Summer 2015

Contributions to modeling of bubble entrainment for ship hydrodynamics applications

Jiajia Li
University of Iowa

CONTRIBUTIONS TO MODELING OF BUBBLE ENTRAINMENT FOR SHIP HYDRODYNAMICS APPLICATIONS

by

Jiajia Li

A thesis submitted in partial fulfillment
of the requirements for the Doctor of
Philosophy degree in Mechanical Engineering
in the Graduate College of
The University of Iowa

August 2015

Thesis Supervisor: Professor Pablo M. Carrica
Dr. Alejandro M. Castro

Graduate College
The University of Iowa
Iowa City, Iowa

CERTIFICATE OF APPROVAL

_____

PH.D. THESIS

_____

This is to certify that the Ph.D. thesis of

Jiajia Li

has been approved by the Examining Committee
for the thesis requirement for the Doctor of Philosophy
degree in Mechanical Engineering at the August 2015 graduation.

Thesis Committee: _____
Pablo M. Carrica, Thesis Supervisor

_____
Alejandro M. Castro, Thesis Supervisor

_____
Christoph Beckermann

_____
Ching-Long Lin

_____
James H.J. Buchholz

ACKNOWLEDGMENTS

I would like to thank my supervisor, Dr. Pablo M. Carrica for his encouragement, support and guidance during my graduate studies. Dr. Carrica has shown me an academic quality that I admire and respect. He always encourages me to explore my potential and offers guidance. Also, I am deeply indebted to Dr. Alejandro M. Castro for his guidance and assistance. Interacting with him affected positively my research work and also my personal life. I would like to thank Profs. Christoph Beckermann, Ching-Long Lin and James H.J. Buchholz for serving as my dissertation committee members.

I had the pleasure to work with my colleagues Juan E. Martin, Yuwei Li, Matias N. Perret, Alireza Mofidi, and Mehdi Esmaeilpour, who deserve many thanks for their suggestions and help during my studies.

I deeply thank my parents, my wife, and my son for their support. I could have never completed this work successfully without their encouragement.

In addition, I would like to express gratitude to the sponsors of our project. This research was supported by the Office of Naval Research under Grant N00014-14-1-0134. Drs. Patrick Purtell, Ki-Han Kim, and Thomas Fu were the program managers. The simulations in this work were performed using the high-performance capabilities offered by the Department of Defense's High Performance Computing Modernization Program.

ABSTRACT

This thesis presents two important contributions to the modeling of entrainment of air bubbles in water, with focus on ship hydrodynamics applications.

The first contribution consists of a general framework for modeling turbulent air entrainment. The framework attempts to describe the evolution of bubbles from their formation at the free surface, size distribution changes due to breakup and coalescence, and rise due to buoyancy. This proposed framework describes the complex entrainment process as a series of simpler mechanisms which can be modeled independently. For each mechanism a simple but mechanistic model is developed to provide closure while leaving the door open for future improvements. These unique characteristics enable the entrainment model to be used in general problems while still producing results at least as good as the few other available models.

The massive entrainment of air that takes place around a ship leads to very high void fractions and accumulation of bubbles against the hull, particularly underneath the flat regions of the hull and in low pressure regions near appendages. These processes also pose challenges for two phase solvers. As a second contribution in this thesis, numerical algorithms for two phase flows are developed to eliminate the numerical instabilities normally occurring at high void fractions or large void fraction gradients. A hybrid method to improve pressure-velocity coupling for collocated grids is introduced, which keeps advantages typical of staggered grids in mass conservation and face flux computations. A new two phase coupling strategy is developed to guarantee stability at high void fraction. The balanced force method is extended to general curvilinear grids to suppress spurious velocities. The overall methodology provides strong coupling among pressure, velocity and void fraction, while avoiding numerical instability, and works for free-surface flows on dynamic overset grids.

The proposed numerical schemes are tested for 1D and 2D cases. It is shown that the two phase solver is stable and efficient, even for extreme cases. Good mass conservation properties for multigroup simulations are also demonstrated. The air entrainment model is tested for a 2D wave breaking case and compared with extensive experimental data. The results show good predictions for entrainment location and other two-phase metrics such as size distributions.

Full scale simulations for Athena R/V are performed using the same modeling constants obtained for the 2D wave breaking case. A grid study is also carried out to evaluate grid convergence properties of the model. While the model can predict well experimental data at full scale for the ship, it also shows dramatic improvements respect to previous entrainment models by converging in grid and not needing to re-evaluate the model constants for each new application. A high-speed Kann boat is also simulated at full scale, showing encouraging results for a preliminary entrainment model for aeration due to impact. The proposed numerical schemes are proved stable and robust in high Reynolds number flows with complex relevant geometries. In addition, these full scale simulations also identify modeling and numerical issues for future improvements.

PUBLIC ABSTRACT

Bubbles entrained around a ship have significant effects to the ship hydrodynamics. This thesis presents two important contributions to the modeling of air entrainment relevant to ship applications.

The first contribution contains a general framework for modeling air entrainment in turbulent flows. This proposed framework describes the complex entrainment process as a series of simpler mechanisms which can be modeled independently. For each mechanism a simple but mechanistic model is developed while leaving the door open for future improvements.

The massive entrainment of air that takes place around a ship leads to accumulation of bubbles, particularly underneath the flat regions of the hull and in low pressure regions near appendages. These processes also pose challenges for numerical solver. As a second contribution in this thesis, numerical algorithms for air-water flows are developed to eliminate the numerical instabilities normally occurring in regions where large amount of bubbles accumulate.

The proposed numerical schemes can improve the stability of simulations as shown in 1D and 2D cases. The air entrainment model is tested for a 2D wave breaking case and compared with experimental data. Simulations for a vessel, Athena R/V, are performed using the same configuration for the model as in the 2D wave breaking case. The model can predict well experimental data and shows dramatic improvements respect to previous entrainment models. A high-speed Kann boat is also simulated, showing encouraging results for a preliminary entrainment model for aeration due to impact.

TABLE OF CONTENTS

LIST OF TABLES

LIST OF FIGURES

LIST OF SYMBOLS

English symbols

$\boldsymbol{a}_i$	Covariant base vector (Chapter 3)
A	Coefficient resulting from discretization of convection and diffusion terms (Equation (3.3), Chapter 3); Transversal area (Chapter 4)
A_s	Surface area (Equation (1.10))
b	Width in the perpendicular direction (Section 4.12)
$\boldsymbol{b}^i$	Normal vector to constant i -plane (Chapter 3)
c_b	Source strength constant (Equation (1.12))
c_L , c_η	Turbulence spectrum constant (Equation (4.7))
c_λ	Mixing length turbulence model constant (Section 4.10)
C	Turbulence spectrum constant (Equation (4.7)); Impact entrainment model constant (Section 4.12 and 5.3)
C_{air}	Entrainment source strength constant (Equation (1.10))
C_{ent}	Entrainment source strength constant (Equation (1.11))
C_D	Drag coefficient
$\hat{C}_{D,g}$	Modified drag coefficient for group g (Chapter 2, Section 3.2.1)
C_L	Lift coefficient
Co	Courant number (Chapter 3)
C_{VM}	Virtual mass coefficient
d	Bubble diameter (Section 1.2)
d_0	Nozzle diameter (Section 1.2)
d_{10}	Bubble mean diameter
d_{32}	Bubble Sauter diameter
d_e	Entrainment depth (Section 4.12)
d_{w}	Distance to the wall (Chapter 3 and 4)

D	Bubble diameter
D_0	Formation bubble diameter (Chapter 4)
D_g^{ent}	Discretized entrainment size distribution (Chapter 5)
D_g	Group diameter; discretized size distribution (Table 3.1)
D_s	Diameter of entrainment ring (Chapter 4)
$\tilde{D}_s$	Non-dimensional function (Equation (4.23))
D_H	Hinze scale
ΔD_g	Bin width at group diameter D_g (Chapter 1)
e_{ij}	Metric of contravariant gradient (Chapter 3)
$\dot{E}^G$	Required power for potential force (Chapter 4)
$\dot{E}^\sigma$	Required power for surface tension force (Chapter 4)
E_d	Disturbance kinetic energy per unit volume (Equation (1.10))
E_t	Turbulent kinetic energy per unit volume (Equation (1.10))
f	Faces of a control volume (Chapter 3); volumetric force (Section 3.4); bubble number density distribution
f_k	Entrainment modeling factor (Equation (1.13))
f_E	Bubble size distribution at entrainment (Chapter 1)
F	Source term from discretized form of time derivative (Equation (3.4))
$\mathbf{F}^{\text{WF}}$	Non-dimensional wall force (Equation (3.35))
F_1	Blending function in $k-\varepsilon$ / $k-\omega$ SST model (Equation (4.51))
F_q	Volumetric flux on free surface (Section 1.3)
g	Gravity acceleration (Chapter 1, Chapter 4); group number (Chapter 2); test function of void fraction (Equation (3.38))
$\boldsymbol{g}$	Gravity vector (Section 1.2)
g_k^j	Inverse metric of b_j^k (Equation (3.34))
G	Number of discrete bubble groups (Chapter 2)
J	Jacobian of a matrix (Chapter 3; volumetric flux per unit area (Chapter 4)

J_p	Jacobian for the control volume at node p (Chapter 3)
k, k_t	Turbulent kinetic energy (Section 4.9)
$\hat{k}$	Unit vertical direction
K	Entrainment modeling constant (Chapter 1)
K_1, K_2	Entrainment modeling constant (Chapter 1)
ℓ	Vortex length scale (Chapter 4)
ℓ_t	Turbulent integral length scale for $k-\omega / k-\varepsilon$ SST model (Figure 4.3)
ℓ_E	Entrainment depth (Equation (1.13))
l_1	l_1 norm (Chapter 3)
L	Characteristic length scale (Section 1.2, Chapter 2, Chapter 5); length scale in turbulence field (Section 4.2)
L_{11}	Integral length scale (Chapter 4-5)
L_D	Length scale for bubbles rising in turbulent flow (Table 4.3)
L_j	Jet length (Chapter 1.2)
L_{EI}	Transition length from the energy containing range to inertial range (Chapter 4)
L_{ID}	Transition length from the inertial range to the dissipation range (Chapter 4)
m	Total mass in domain (Section 3.6.3)
m_0	Initial total mass in domain (Section 3.6.3)
$\hat{\boldsymbol{n}}$	Unit normal vector to surface (or wall) pointing into water
n_ℓ	Vortex number density (Chapter 4)
N	Number of grid points (Chapter 3)
N_g	Group g number density
N_{tot}	Total number of bubbles (Chapter 3)
p	Pressure; node number (Chapter 3)
p_0	Bubble size distribution at formation (Chapter 4); constant in turbulence spectrum function (Equation (4.7))
p_a	Atmospheric pressure (Equation (4.15))

p_h	Bubble size distribution due to breakup and coalescence (Chapter 4)
p_z	Probability of finding a bubble (Chapter 4)
$\boldsymbol{P}$	Acceleration due to packing force (Chapter 2-3)
P_B	Probability of breakage (Chapter 4)
$\breve{q}_{f,i}$	Contravariant Slip flux on faces (Equation (3.25))
q_A	Entrainment rate per unit width (Equation (1.8))
$\overline{q}_A$	Non-dimensional volumetric rate per unit width (Equation (1.7))
Q	Bubble entrainment rate (Chapter 4)
Q_ℓ	Rate of air entrainment for a vortex with size ℓ (Chapter 4)
Q_A	Volumetric entrainment rate (Section 1.2)
r	Radial coordinate in polar coordinates (Section 3.6.1)
R	Bubble radius
R_δ	Surface roughness of a jet (Equation (1.8))
s	Slope (Chapter 1 and 4)
$\tilde{s}$	Modified slope (Equation (4.17))
S	Entrainment source (Chapter 4)
$\mathbf{S}$	Strain rate tensor
S_0	Source strength constant (Equation (1.3))
S_g	Entrainment source for group g
$S_{\ell 0}$	Turbulent air entrainment constant (Chapter 4-5)
$S_{p,i}$	Source term in discretized liquid momentum equation at node p for i component (Chapter 3)
t	Time
$\boldsymbol{t}$	A vector (Chapter 3)
δt , Δt	Time step interval
u	Instantaneous velocity (Chapter 3-4)
$\boldsymbol{u}$	Velocity vector (Chapter 1-2, Section 4.9)

u'	Fluctuation of jet velocity (Section 1.2)
u_0	r.m.s of velocity fluctuation for isotropic turbulence (Chapter 4)
u_ℓ	r.m.s velocity of eddies with size ℓ (Chapter 4)
$u_{\mathbf{n}}$	Velocity vector in normal direction (Equation (1.11))
$u_{p,i}$	i component of velocity on node p (Chapter 3)
U_0	Boat speed (Equation (4.53))
U_j	Jet velocity (Section 1.2)
$\overline{U}_j$	Non-dimensional jet velocity (Equation (1.7))
$\overline{U}_t$	Non-dimensional transition velocity (Equation (1.7))
$\overline{v}_0$	Mean bubble volume at formation (Chapter 4)
v_g	Bubble volume for group g (Equation (2.4))
$\tilde{V}$	Discretized form of neighbor nodes and source term (Equation 3.4)
V_T	Bubble terminal velocity
dV'	Differential volume (Chapter 4)
dV	Differential volume (Equation (4.5) and (4.6))
$\mathcal{V}$	Configuration of a given vortex (Chapter 4)
$w_{p,i}$	Pseudo-momentum at node p for i component (Equation (3.5))
x	Coordinate in x direction (Chapter 3, Section 4.4); non-dimensional variable (Section 4.5-4.6)
$\boldsymbol{x}$	Position vector (Chapter 3)
$\boldsymbol{x}_E$	Position vector for entrainment places (Chapter 1)
$\tilde{x}$	Non-dimensional variable Equation (4.17); function of $\tilde{s}$ (Equation (4.17))
Δx	Grid size in x direction (Chapter 3)
Δx_0	Grid size for the coarsest grid size in x direction (Chapter 3)
z	Vertical coordinate (Chapter 3); depth under free surface to find a bubble (Chapter 4)
z'	Depth under free surface for a given vortex (Chapter 4)

dz' Differential depth for z' (Chapter 4)

dz Differential depth for z (Chapter 4)

Dimensionless groups

Fr Froude number

We Weber number

Ca Capillary umber

Fr_ℓ Vortex Froude number (Chapter 4)

Sc_b Bubble Schmidt number (Chapter 2)

Greek letters

α Angle of jet inclination (Section 1.2.1); Volume fraction

α_0 Void fraction at free surface

α_{d0} Initial void fraction (Chapter 3)

α_g Void fraction for group g

β Breakup source (Equation 2.3); packing force function (Equation (2.7)); turbulence modeling constant (Equation (4.51))

β^* Modeling constant (Equation (4.50) and (4.51))

χ Coalescence source (Equation (2.3))

δ Surface roughness; Dirac delta function (Equation (1.3))

$\delta_{i,j}$ $=1$ if $i = j$ or 0.

δ_{FS} Peak to peak value for surface waves (Chapter 4-5)

$\varepsilon, \varepsilon_t$ Turbulence dissipation

ε_m Defect of mass (Section 3.6.3)

ϕ Distance to free surface; an arbitrary scalar (Equation (3.1) and (3.2))

γ Turbulence modeling constant (Equation (4.51))

η Fraction of turbulent energy that can entrain bubbles (Equation (1.13)); Kolmogorov scale (Chapter 4)

κ Wave number (Section 4.2); weighting factor (Equation (3.28))

λ	Wavelength (Section 4.12); length scale of surface roughness (Equation (4.52))
μ	Dynamic viscosity
μ_{eff}	Effective dynamic viscosity (Equation (4.47))
ν	Kinematic viscosity
ν_p	Modeling kinematic viscosity due to packing effects
ρ	Mass density
σ	Surface tension
σ_k, σ_ω	Turbulence modeling constant (Equation (4.50) and (4.51))
$\sigma_{\omega 2}$	Turbulence modeling constant (Equation (4.51))
ω	Weights from time marching discretization (Chapter 3); Specific dissipation rate (Chapter 4)
$\vec{\omega}$	Vorticity vector (Figure 1.2)
Ω_g	Normalized group void fraction (Equation (3.26))
ξ	Computational coordinate of a point (Chapter 3)

Subscripts

e	Entrainment
l	Liquid
c	Continuous phase
cr	Critical value
d	Disperse phase
g	Gas; group number
M	Maximum
t	Turbulence
s	Surface (Chapter 4)
m, min	Minimum
r	Relative value
p	Node p (Chapter 3)

nb	Neighbor nodes (Chapter 3)
f	Face of a control volume (Chapter 3)
D	Diameter
i, j, k	Index from 1 to 3
ent	Entrainment
n	n time steps (Chapter 3)
ref	Reference
ℓ	Vortex with size ℓ (Chapter 4)

Superscripts

n	n time steps (Chapter 3)
$*$	Predicted term (Chapter 3)
$+$	Turbulent sublayer scaled value
$\smile$	Contravariant vector (Chapter 3)
i, j	Index from 1 to 3 (Chapter 3)
$-$	Linear interpolated value from neighbor nodal values (Chapter 3)

Abbreviations

CFD	Computational fluid dynamics
CS	Collocated scheme (Chapter 3)
DES	Detached eddy simulation
ENO	Essentially non-oscillatory
HS	Hybrid scheme (Chapter 3)
LES	Large eddy simulation
ML	Mixing length mode (Chapter 5)
MNL	Menter's model with no limit in production (Chpater 5)
PISO	Pressure implicit with splitting of operator (Chapter 3)
RANS	Reynolds averaged Navier-Stokes
RHS	Right hand side (Figure 3.1)

SIMPLE	Semi-implicit method for pressure-lined equations
SST	Shear stress transport
TPM	Two phase Menter's blended turbulence model (Chapter 5)
TVD	Total variation diminishing

Operators

∂_i	Partial derivative in i component
$\breve{\nabla}_i$	Contravariant gradient in i component

CHAPTER 1 INTRODUCTION

1.1 Motivation

Air entrainment occurs naturally when a surface ship is advancing in a seaway. Bubbles can be entrained at bow and shoulder waves, the contact line of the hull with free surface and turbulent flow of stern. The sizes of bubbles can range from micrometers to millimeters. These bubbles have significant importance to the ship signature. Firstly, the entrainment of wave breaking near the ship is a source of acoustic noise. This noise can be detected by acoustic means (Borowski et al. 2008), resulting in increased probability of detection. Secondly, the presence of bubbles also has an impact on the hydrodynamic motion of the ship. Experiments in ships and flat plates of bubble-induced drag reduction show drag reduction can vary more than 4% (Latorre et al. 2003, Elbing et al. 2008). This can have dramatic impact on economy considering that 80% of volume of world trade is through maritime transportation (UNCTAD 2009). Thirdly, the bubbly wake behind the ship can last for a long distance. Experiments demonstrate that the length of the bubbly wake can reach 5000 m and the depth could be up to 10 m (Trevorrow et al. 1994, Trevorrow et al. 2006, Sutin et al. 2009). This signature can be observed on the sea surface as white water wake and detected acoustically from underwater. It enables the ship to be monitored by airplanes and satellites, increasing the risk for a navy ship to be an attack target.

Air entrainment is important for other natural and engineering applications. It can enhance mass and energy transfer between air and water in natural world, resulting a key role in global climate change. Air entrainment also contributes to the efficiency of the mixture flow in gas-liquid reactors, and the quality of products in casting industry.

Figure 1.1: Example of bubbly flow around a ship.

As shown in Figure 1.1, the white water around the ship is the indicator of presence of bubbles. These bubbles are mainly generated from interactions between the flow and the free surface, with potential bubble production by propeller cavitation. The main types of air entrainment around a ship can be summarized as follows: (see Figure 1.2)

a. **Plunging jet entrainment**: A falling liquid jet pierces a free surface and causes entrainment around the contact line. Wave breaking produced by ships can result in such form of air entrainment.
b. **Cavity fragmentation entrainment**: The jet or splash of breaking waves can entrap large air cavities into the water. These cavities are then subject to the flow turbulence and breakup into smaller bubbles.
c. **Droplet impact entrainment:** Sprays and splash formed by wave impact and wind form droplets that hit the free surface and trap air into the water. The resulting bubble sizes can be very small (for example, typically around $50\,\mu m$ in diameter for Mesler entrainment).
d. **Vortex induced entrainment:** Vortices interacting with a free surface can entrain bubbles when they are energetic enough. The high turbulent flow at the stern and in the

boundary layer near the free surface of a ship can entrain significant amounts of air bubbles.

The described main mechanisms of entrainment may be caused by a variety of processes present around a ship. Bow and shoulder waves often exhibit plunging jets and high levels of turbulence. The contact line between the hull and the free surface is subject to the highly turbulent ship boundary layer. The stern flow, mostly in transom sterns, exhibits highly energetic large-scale vortices and massive entrainment. It should be noticed that other air entrainment processes may also exist around ships, but the complexity of the problem is evident even if the study is limited to the mechanisms discussed above.

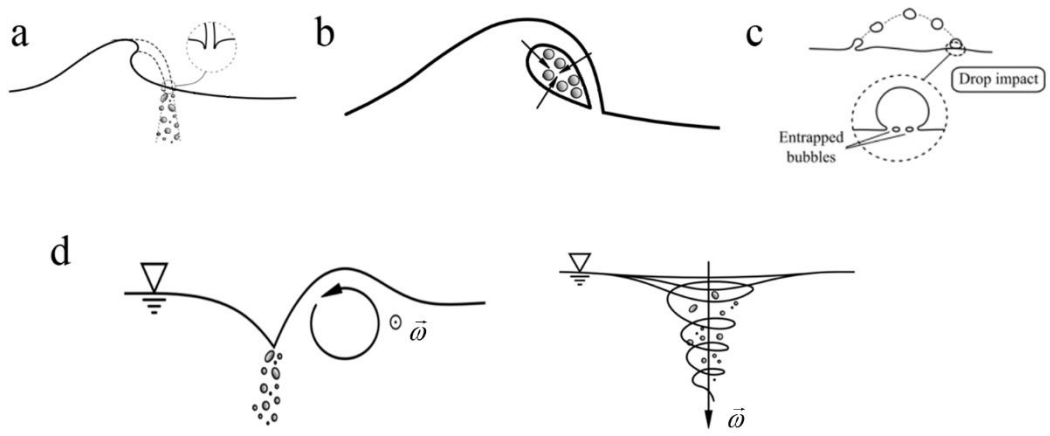

Figure 1.2: Schematic diagram for different entrainment processes.

Though bubble transport is a complex problem and far from a mature state of development, it has been tackled extensively by the nuclear industry (Wallis 1969, Ishii 1975, Ishii and Hibiki 2006, Drew and Passman 1999, Behzadi et al. 2004, among others) and applied to surface ships (Carrica et al. 1998, 1999, Moraga et al. 2008, Castro 2011, Ma et al. 2010b). The transport of bubbles around the ship and in its wake has unique challenges, mostly due to the very high Reynolds number boundary layer and the presence of the air/water interface not found in other applications. It is in this context that air

entrainment modeling is extremely important, since the development has not kept pace with bubble transport modeling. Although much progress has been achieved over last few decades, the current entrainment models still cannot predict bubbly flow correctly around a ship. It is recognized at this point that the entrainment of bubbles is the most underdeveloped component in modeling the bubbly flow around ships, and is crucial to properly predict the bubbly wakes (Castro et al. 2014). This topic is specially challenging due to the multiple physical phenomena involved in the entrainment process.

1.2 Air entrainment background

As discussed before, air entrainment involves several physical processes. Experimental and modeling work in literature has been limited to a few canonical flows. Simple plunging jets were studied first, measuring mostly air entrainment rate. Breaking waves have more recently become another important flow to study air entrainment, though much more complicated than the plunging jet. Vortex interaction with a free surface and consequent air entrainment can now be studied numerically and experimentally. Advanced cameras enable capturing bubble entrainment from droplet impact. Air entrainment caused by these flows is still at an early stage of research. This section mainly reviews for the state of the art on modeling these four air entrainment mechanisms.

1.2.1 Plunging jet

A plunging jet consists of an incoming fluid steam of velocity U_j impacting a receiving pool of the same fluid (Kiger and Duncan 2011). Key parameters characterizing the flow are defined as:

$$\begin{aligned} \mathrm{Fr} &= U_j \big/ \sqrt{gL} \\ \mathrm{We} &= \rho_l U_j^2 L \big/ \sigma \\ \mathrm{Ca} &= \mu_l U_j \big/ \sigma \end{aligned} \tag{1.1}$$

where Fr is the Froude number, We is the Weber number, Ca is the capillary number, L is the length of the jet, ρ_l is the liquid density, μ_l is the liquid dynamic viscosity and σ is the surface tension.

When the jet impacts the pool surface, it may or may not entrain bubbles. No bubbles are observed in the pool when the jet velocity is low. As the velocity increases, and the process gains enough energy to entrap air by overcoming surface tension and potential energy due to gravity, bubbles begin to appear around the impact region. A key parameter for plunging jets is then the condition for onset of air entrainment. Lara (1979) established two regions of onset jet velocity for a vertical plunging liquid jet: continuous jet and jet droplets. The author showed that the droplet region has lower onset velocity. Bin (1993) proposed a correlation $U_e = 5L^{0.534}$ (here subscript means entrainment, the same for later use in equation) for the droplet region based on the data of Bin (1988) and Kumagai and Endoh (1983). Lin and Donnelly (1966) measured the onset velocity for different fluids with high viscosity, and proposed a correlation as $\mathrm{We}_e = 10\,\mathrm{Re}_e^{0.74}$, where the length scale is the diameter of the jet at the impact point. Lorenceau (2003) combined her data with that from Lin and Donnelly (1966) to obtain a new correlation for the onset of entrainment $\mathrm{Ca}_e = -1.6\ln\left(\mu_g/\mu_l\right) - 13.7$. For low-viscosity jets the onset condition is not well defined. Ciborowski and Bin (1972) proposed $\mathrm{We}_e = 400$ for turbulent short-length jets. El Hammoumi et al. (2002) observed a condition given by $\mathrm{Ca}_e = 0.04$ for $\mathrm{Re} \sim 200$ using an oil/air system. A dimensionless correlation for the onset velocity including turbulent fluctuation (denoted as u') but without physical motivation was developed by Chanson (2009) : $U_e\mu_l/\sigma = 0.0109\left[1 + 3.375\exp\left(-70u'/U_e\right)\right]$.

A second key parameter is the entrainment rate Q_A, typically separated into two regions according to the jet velocities. van de Sande and Smith (1974, 1976) proposed $Q_A = 0.015\left(d_0^2 U_j^3 L_j^{0.5} \sin^{-1.5}\alpha\right)^{0.75}$ for low jet velocities ($2\,\mathrm{m/s} < U_j < 5\,\mathrm{m/s}$) (valid for certain experimental parameters), where d_0 is the nozzle diameter and α is the jet deviation angle from horizontal free surface. For high jet velocities, two different

mechanisms are proposed: air entrained by the jet roughness and air dragged by the boundary layer along the jet. Ervine et al. (1980) and McKeogh and Ervine (1981) formulated an entrainment rate equation based on these two mechanisms and experimental data. Bin (1993) reported that the boundary layer air entrainment contributed 20 to 70% to the total and thus cannot be ignored. Sene (1988) deduced an analytical equation for the air layer trapped in water using a Couette flow assumption, resulting in $Q_A \sim U_j^{1.5}$. Kiger and Duncan (2011) reported more recent developments for the relationship between Q_A and U_j. The entrainment rate follows $Q_A \sim U_j^{1.8}$ for a low velocity jets and $Q_A \sim U_j^{0.5}$ for higher velocity jets in the work by Brattberg and Chanson (1998), while Ma et al. (2010a) proposed $Q_A \sim U_j^2$ and $Q_A \sim U_j^1$ for low and high velocities, respectively. Results of El Hammoumi et al. (2002) imply $Q_A \sim U_j^{1.23}$ for high speed jets. Though these results indicate certain similar characteristics, it is difficult to make universal conclusions due to different experimental conditions.

Several attempts at numerically simulating air entrainment caused by plunging jets are reported in the literature. Iafrati et al. (2004) and Brouilliot and Lubin (2013) simulated 2D plunging jets, though conclusions are of little consequence since bubbles are inherently 3D. Deshpande et al. (2012) simulated a 3D inclined plunging jet using the volume of fluid (VOF) method. Even though large cavities can be captured, the grid is not fine enough to resolve small bubbles.

1.2.2 Breaking waves

Breaking waves can be classified as four types: spilling, plunging, collapsing and surging (Galvin 1968). Though all these can entrain bubbles, research on entrainment has mainly focused on spilling and plunging breakers. For plunging breakers, Kiger and Duncan (2011) summarized four major mechanisms for entrainment: entrapment of a closed air cavity when the jet hits the front wave face, entrainment around the impact region, entrainment by forward splash and backward splash, and entrainment over the

splash and turbulent breaking regions. Spilling breakers not always entrain bubbles, but occur more frequently than plunging breakers. The progress in experimental measurements and modeling has been slow due to the complexity of the breaking process (Duncan 2001).

Experimental data is scarce for entrainment due to the complexity of the two phase flow during the early process of wave breaking. Two important aspects are usually reported in the literature: bubble size distribution and energy dissipation during the process. Deane and Stokes (2002) measured the size distribution of bubbles for plunging breaking waves. Two distinct phases are observed in the experiments: acoustically active phase and quiescent plume phase. Entrainment occurs mainly in the first phase, where acoustic noise from the splash and bubble formation takes place. Cavity fragmentation generating large bubbles (large than 2 mm in radius) is observed from noise spectrograms. The bubble size distribution for the acoustic phase has the form of $f(r) \propto r^s$, where s is the slope in a log-log plot. Two different slopes are found: $-3/2$ for bubbles smaller than 1 mm in radius and $-10/3$ for the rest, with 1 mm reported as the Hinze scale for the breaking waves. Leifer and de Leeuw (2007) studied bubble plumes generated by paddle-amplified, wind-stress breaking waves subsequent to formation. Two main categories of plumes are reported: diffuse plumes with low concentration of bubbles and dense plumes containing large numbers of bubbles which can obscure the background. The bubble size distribution responds to a power law and two distinct regions of different slopes are separated by a critical radius. Both slope and critical radius vary for different plumes. The size distribution is found to steepen with time as large bubbles breakup and/or rise and leave the domain. Mori et al. (2007) studied void fraction and bubble size distribution for wave breakers in laboratory experiments at two different scales. It was found that the slope of the time and space-averaged bubble size distributions is independent of the experimental scale within a range -1.2~-1.9 while the scale effect becomes evident in void fraction. Blenkinsopp and Chaplin (2010) used highly sensitive optical fiber phase-detection probes to measure high void fraction on breaking waves. They observed bubbles up to 60 mm in diameter close to

the surface but away from the active entrainment region. The slope reported for plunging waves varies from −1.4 to −3.15 while it changes from −2.1 to −2.9 in the spilling/plunging case. The variation in the slope occurs at diameters between 1.7 mm and 2.4 mm.

Johansen et al. (2010) performed measurements around the Full-scale Athena research vessel. The bubble size distribution at the plunging bow wave was reported, showing a slope around -2.35. Tavakolinejad (2010) also measured the bubble size distribution for a 2D+T simulated breaking bow waves using a high speed camera technique. The bubble size distributions at different times (equivalent to positions along the ship) follow a power law. It has to be mentioned that the measurements were not performed near the active entrainment region, thus bubbles experienced coalescence, breakup and dissolution processes before being measured.

Energy dissipation is significant in wave breaking process. Horikawa and Kuo (1966) proposed that bubbles entrained by breakers is significant in energy dissipation, at least at initial stages. Rapp and Melville (1990) concluded that the energy dissipated by wave breaking could be up to 40% of the initial energy. The amount of entrapped air can be related with the energy dissipation in breaking waves (Loewen and Melville 1994). According to Lamarre and Melville (1991), entraining bubbles can cost a high fraction (30 to 50%) of the wave energy. Hoque (2002) demonstrated that wave steepness is important for the volume of entrained air and energy dissipation rate. Iafrati (2011), from a 2D numerical study, concluded that entraining air could account for a fraction between 10 to 35% of the energy dissipated by a wave breaking event.

Numerical simulation of breaking waves is more challenging than plunging jets. 2D plunging breakers were simulated by Dalrymple and Rogers (2006) and Landrini et al. (2007) using smooth particle hydrodynamics techniques. An interesting conclusion is that the jet does not penetrate the front surface of the wave deeply, unlike the situation in a typical steady plunging jet, but bounces up to form a forward splash. A vortex dipole can

be formed for the backsplash which drags bubbles deeper. Adams et al. (2010) used VOF with 134 million nodes to simulate a plunging breaking wave without surface tension and viscous effects. Though quite a few bubbles can be found after wave breaking, the small bubbles cannot be predicted correctly due to the absence of surface tension. On the other hand, the small bubbles require even higher spatial resolution.

1.2.3 Vortex interaction with a free surface

A vortex can entrain bubbles by interacting with a free surface. A bathtub vortex, also known as drain-type vortex, can form an air tube dependent on the vortex strength. Takahashi et al. (1988) performed an experiment to investigate the onset conditions for air entrainment by a drain-type vortex, providing empirical criteria based on their data. Transient behavior of air entrainment was studied by Ezure et al. (2008) with visualization techniques. It was observed that the extension of the air core length delays to the increase of circulation around the vortex. Ezure et al. (2011) studied the bubble size distribution for the entrainment by a drain-type vortex. The mean equivalent bubble diameter varies from 1.3 to 2.1 mm and is influenced by the thickness of air core.

When the direction of a vortex is parallel to the free surface, it can also entrain bubbles by fragmenting the surface with strong shear stress. Greaves and Kobbacy (1981) observed that small vortices formed due to turbulence generated at interface when investigating surface aeration. Oguz et al. (2002) proposed that large scale vortex rings were responsible for destabilizing the meniscus formed in a plunging jet. Jeong and Moffatt (1992) carried out experiments using a pair of counter-rotating cylinder with a free surface, observing that a sharp cusp occurs on the free surface when the vortex strength increases to a certain level. Jeong (2012) analytically studied free surface deformation before entrainment due to a vortex in Stokes flow. A much more complicated situation occurs with free surface turbulence, which has been studied widely (Shen and Yue 2001, Lang and Manglano 2004, Savelsberg and van de Water 2009). The up-swelling and spiral eddies

can destabilize the free surface and cause entrainment (Townsend 1966, Davies 1972, Hirt 2003).

1.2.4 Droplet impact

Entrainment processes are well described by Pumphrey and Elmore (1990) when a drop of water impacts on a water surface. The process that can result in a large number of small bubbles is called Mesler entrainment. When a droplet impacts a flat liquid interface with a relatively low velocity, a large number of very small bubbles (typically below $50\,\mu m$ in diameter) are produced. This phenomena is referred to as Mesler entrainment (Mesler and Mailen 1977, Bergman and Mesler 1981, Esmailizadeh and Mesler 1986). Sigler and Mesler (1990) conducted a photographic study that showed a chandelier style pattern of bubbles formed after the droplet impacted the interface. Thoroddsen et al. (2003) used a one million fps camera to temporally resolve the air film between the drop and bulk fluid. They found that about 5000 bubbles with size $15\ \mu m$ could be formed during a single drop impact for low impact velocities. Bick et al. (2010) studied bubble formation via multi-drop impacts, quantifying the critical crater depth formed upon impact and the time interval between drop impacts for entrainment to happen. It was established that bubbles could be produced at much lower velocities if two or more drops impacted the liquid-air interface within an appropriate short interval in time. Saylor and Bounds (2012) performed an experiment that studied the role of the Weber and capillary numbers on Mesler entrainment, it was found the region of onset of Mesler entrainment in plots of percent occurrence can be scaled by these parameters.

1.3 State of the art on air entrainment modeling

Direct simulation of air entrainment for engineering applications will be beyond the computational capabilities over the foreseeable future. Modeling of air entrainment processes compatible with feasible numerical approximations to engineering problems (RANS/DES approaches) is still on its infancy (Castro et al. 2014). A good entrainment

model has to answer three key questions: where to entrain (place to activate entrainment), when to entrain (conditions for entrainment), and how to entrain (entrainment rate and bubble size distribution). It is unlikely that these questions will be answered satisfactorily soon, due to the incomplete understanding of the physical process involved in entrainment. However, models developed recently show hope that reasonable predictions of entrainment for many applications are feasible. Since the aim of this thesis is air entrainment around ships, our focus will be on entrainment for air-water systems.

Baldy (1993) assumed bubble generation at small scales was self-similar, borrowing the idea from turbulence theory. According to this assumption, the entrainment rate depends only on the state of eddies in the inertial range and formation energy of a bubble without considering other effects. A simple entrainment equation is derived through energy balance with dimensional considerations:

$$S(d) = K \frac{\varepsilon_t}{\sigma d^2 / \rho_l} \tag{1.2}$$

where K is a constant, ε_t is turbulence dissipation, d is the bubble diameter. This equation shows that the entrainment source is strong when the turbulence dissipation is large.

For computational fluid dynamics (CFD) applications, air entrainment models can be implemented in two ways, as boundary conditions at the free surface or as volumetric sources near the entrainment region. Air entrainment is an interfacial process as bubbles are entrained by destabilizing the free surface. However this process is short, transient, and greatly localized, resulting in difficult implementation in a CFD code. Thus, there is a trend to model air entrainment as a volumetric source.

The work by Carrica et al. (1999) probably is the first attempt in applying air entrainment in computational ship hydrodynamics, where air was entrained in a certain region manually determined by the authors, with the bubble size distribution imposed as in the experimental data from Cartmill and Su (1993). Bubbles are transported into the water by assigning void fraction and bubble velocity as boundary conditions at the free surface.

This model essentially uses Dirichlet boundary conditions for both group void fraction and velocity.

Moraga et al. (2008) proposed the first predictive model for CFD applications in ship hydrodynamics. The entrainment, modeled as a volumetric source, can be written for each bubble size as

$$S_g(\boldsymbol{x}) = S_0 f_E(D_g) \Delta D_g \sum_E \delta(\boldsymbol{x} - \boldsymbol{x_E}) \tag{1.3}$$

where S_0 is a constant which determines the source intensity, f_E is the bubble size distribution function and ΔD_g is the bin width for the group diameter D_g. The summation of δ functions is designed to selectively choose active grid nodes. This model does not provide bubble size distribution; instead f_E is obtained from experimental data in the acoustic phase measured by Deane and Stokes (2002). Entrainment conditions can be summarized as,

$$\boldsymbol{u}_c(\boldsymbol{x_E}) \cdot \frac{\boldsymbol{g}}{\|\boldsymbol{g}\|} > u_e \approx 0.22\,\text{m/s} \tag{1.4}$$

$$\boldsymbol{u}_c(\boldsymbol{x_E}) \cdot \hat{\boldsymbol{n}} > u_e \approx 0.22\,\text{m/s} \tag{1.5}$$

$$0 < \phi(\boldsymbol{x_E}) < \phi_{\text{ent}} \tag{1.6}$$

where $\boldsymbol{g}$ is the gravity vector, $\hat{\boldsymbol{n}}$ is the normal direction to the interface pointing into the water, ϕ is the signed distance to the free surface and ϕ_{ent} is a constant estimated from the penetration depth of a plunging jet. There are two adjustable constants, S_0 and ϕ_{ent}, which may vary for different flows.

Ma et al. (2010a) developed a quantitative sub-grid model of air entrainment based on plunging jets. Entrainment rate equations are derived for different jet speeds under strong assumptions for the jet. The non-dimensional volumetric rate per unit width of the jet can be written as,

$$\bar{q}_A = \begin{cases} 0 & \bar{U}_j < 1 \\ K_1 \bar{U}_j^3 & 1 \le \bar{U}_j < \bar{U}_t \\ K_2 \bar{U}_j^{1.5} & \bar{U}_t \le \bar{U}_j \end{cases} \tag{1.7}$$

where K_1 and K_2 are two modeling constants, $\bar{U}_t$ is the non-dimensional transition velocity that separates different mechanisms for entrainment, and $\bar{U}_j$ is the non-dimensional jet velocity. The velocity scale is the critical velocity which is set to 1 m/s. Experimental data from several researchers can be generalized into Equation (1.7) by using different constants. The location of entrainment is determined according to the criterion in Moraga et al. (2008). The model is active near a free surface within a given region and only one bubble size is included. Carrica et al. (2012) also proposed an entrainment model based on experimental data of plunging jets. The entrainment rate per unit width is written as,

$$q_A = 2.43\left(U_j - u_e\right) R_\delta \tag{1.8}$$

$$u_e = 22.5 R_\delta^{1/2} + 1.31 \tag{1.9}$$

where R_δ is the surface roughness of the jet which can be estimated from turbulent kinetic energy at the plunging point. This model is applied along a contact line for wave breaking manually, which is inconvenient for implementation in general flows.

Using dimensional analysis, Garrett et al. (2000) showed that the bubble size spectrum depends on the turbulence dissipation. Cox and Shin (2003) studied the void fraction dependence on turbulence intensity for waves in the surf zone. Mori et al. (2007) found a linear relationship between void fraction and turbulence intensity in an experimental study. These studies highlight the importance of turbulence in air entrainment, prompting recent efforts to focus on turbulence as a significant parameter for air entrainment modeling.

Hirt (2003) proposed a model based on a simple energy balance law assuming that turbulent eddies raise small liquid elements out of the water, which could trap air into the liquid. The volume rate of entrainment is

$$Q_A = \begin{cases} C_{\text{air}} A_S \left(2\left(E_t - E_d\right)/\rho_c\right)^{1/2} & E_t > E_d \\ 0 & \text{otherwise} \end{cases} \tag{1.10}$$

where A_s is the surface area, E_t is the turbulent kinetic energy per unit volume, E_d is the disturbance kinetic energy per unit volume including surface tension and potential energy due to gravity, and C_{air} is a constant.

Shi et al. (2010) proposed a model by assuming that the entrainment source was proportional to the shear production term in the $k-\varepsilon$ turbulence model with bubble size distribution following the experimental data of Deane and Stokes (2002). The results of wave breaking simulations show a reasonable prediction of the entrainment position. Ma et al. (2010b) presented a model assuming that cavities with size equal to the surface roughness could be entrained in the normal direction to the free surface. The volumetric source is written as,

$$Q_A = \begin{cases} C_{\text{ent}} \dfrac{\partial u_n}{\partial \hat{n}} \dfrac{k_t}{\phi_{\text{ent}} g} & \dfrac{\partial u_n}{\partial \hat{n}} > 0, \phi < \phi_{ent} \\ 0 & \text{otherwise} \end{cases} \tag{1.11}$$

where $\partial u_n / \partial \hat{n} = \nabla u_n \cdot \hat{\boldsymbol{n}}$ with $\hat{\boldsymbol{n}}$ the normal vector to surface pointing into water, u_n is the liquid velocity in the normal direction, k_t is the turbulent kinetic energy, g is the acceleration of gravity, and ϕ_{ent} is the depth of active region near the free surface for entrainment. The source strength is controlled by C_{ent}. Castro (2011) applied this model to the bubbly flow around the US Navy research vessel Athena R/V. It was found the void fraction at the bow was two orders of magnitude smaller than that in experiments when the source strength constant was calibrated using the void fraction at stern.

Ma et al. (2011a) followed the ideas from Baldy (1993) and proposed an entrainment model for multiple bubble sizes. The entrainment source for each bubble size is written as,

$$S_g\left(D_g\right) = \frac{c_b}{4\pi}\left(\frac{\sigma}{\rho_c}\right)^{-1} \alpha_c \frac{f_E\left(D_g\right)\Delta D_g}{\sum_{i=1}^{G} D_i^2 f_E\left(D_i\right)\Delta D_i} \varepsilon_t \tag{1.12}$$

where c_b is the source strength constant. f_E is obtained from experimental data (Deane and Stokes 2002). The entrainment region is selected by setting a critical turbulence dissipation ε_c in simulation.

Carrica et al. (2012) presented a model for unresolved turbulent entrainment. The flux of entrainment per unit area is written as

$$F_q = V_T \alpha_0 \approx 2\eta \frac{k_t}{g \ell_E} V_T \; f_k \tag{1.13}$$

where α_0 is the void fraction at free surface, η is the fraction of turbulent energy that can entrain bubbles, f_k is a factor considering not all turbulent scales are energetic enough to entrain air, V_T is bubble terminal velocity, and ℓ_E is the entrainment depth, equal to the integral length scale of turbulence in the model.

As can be seen from the previous discussion, current entrainment models are loosely based on physical mechanisms. They are usually limited to a single type of entrainment with adjustable constants for the strength. The important information of bubble size distribution is determined from experiment data for all available models. The loss of energy in water by entraining bubbles is also neglected. Much more work is needed to properly predict air entrainment, and this thesis attempts to contribute to the topic.

1.4 Contribution of this dissertation

In this thesis, a general framework to develop mechanistic air entrainment models focused on entrainment caused by turbulence near a free surface is developed and implemented in the CFD code REX. The air entrainment framework consists of several mechanisms that attempt to follow the history of the bubbles from their formation at the free surface, size distribution changes due to breakup and coalescence, and rise due to buoyancy. In this manner, the proposed framework describes the very complex entrainment process as a series of simpler mechanisms which could hopefully be modeled independently with various levels of complexity. The model for each mechanisms is based

on physical processes which are different from existing models. The final model can in principle provide

1. Total air entrainment rate. A mechanistic model based on interaction between vortices and the free surface is developed. The onset condition is naturally obtained.
2. Bubble size distribution. Force balances are applied to the formation of bubbles for different sizes. Also, size distribution is changed due to bubble breakup, coalescence, and filtering by buoyancy.
3. Locations where to activate the model. Bubbles are formed at free surface and then transported down to certain depth decided mainly by turbulent mixing and buoyancy effects. The source location is obtained from probabilistic considerations.

This thesis also contributes to the development of algorithms needed to stabilize the bubble transport when the volume fraction is high. To this aim, a two phase solver for pressure-velocity-void fraction coupling suitable for high void fraction problems in collocated overset curvilinear grids are developed. Traditional collocated grid methods are unstable and may result in divergence when the void fraction or its gradient is high. Also, a new mass conservation form is developed to avoid instabilities at high void fraction level. For complex bubbly flows around ships, high void fraction may occur in certain regions due to air entrainment or bubble accumulation. Improvements for the two phase solver can avoid numerical instability under such conditions. In addition, a balanced force method is extended to general curvilinear grid to suppress spurious velocity. Overall, it has the following advantages compared with previous implementation in CFDShip-Iowa 4.5:

1. Stronger coupling between the continuous and dispersed phase. Robust and stable.
2. Stronger pressure velocity coupling in the projection method.
3. Better conservation of all quantities in the fluid field.
4. Stable Solution as the time step decreases.
5. Much more stable for bubbly flow in the boundary layer.

CHAPTER 2 MATHEMATICAL MODEL OF POLYDISPERSED FLOWS

A two-fluid model is used to describe the two phase bubbly flow. The governing equations for each phase can be derived by ensemble averaging the Navier-Stokes equations (Ishii and Hibiki 2006, Drew and Passman 1999). The original two-fluid model equations can be simplified for the case of dispersed bubbly flows (Carrica et al. 1999, Castro and Carrica 2013a, 2013b and references therein), such that the governing equations for the continuous phase (liquid) can be written as (Castro 2011)

$$\frac{\partial \alpha_c \boldsymbol{u}_c}{\partial t} + \nabla \cdot \left(\alpha_c \boldsymbol{u}_c \otimes \boldsymbol{u}_c \right) = -\nabla p_c + \nabla \cdot \left(2\alpha_c \left(\frac{1}{\mathrm{Re}} + \nu_t \right) \nabla^s \boldsymbol{u}_c \right) + \frac{\alpha_d}{\mathrm{Fr}^2} \left(1 - \frac{\rho_d}{\rho_c} \right) \hat{k} + \alpha_d \boldsymbol{P} \tag{2.1}$$

$$\frac{\partial \alpha_c}{\partial t} + \nabla \cdot \left(\alpha_c \boldsymbol{u}_c \right) = 0 \tag{2.2}$$

where a reference length L and velocity U are used to non-dimensionalize the equations, resulting in the Reynolds and Froude numbers defined as $\mathrm{Re} = UL/\nu$ and $\mathrm{Fr} = U/\sqrt{gL}$, respectively, with ν the continuous fluid kinematic viscosity, ρ fluid density, and g the acceleration of gravity. Subscripts *c* and *d* are used to denote the continuous phase (water) and the disperse phase (bubbles) variables. The turbulent exchange of momentum is modeled with a turbulent viscosity ν_t obtained from an appropriate turbulence model. Though the continuous phase is incompressible, its velocity field in general is not divergence-free due to the presence of bubbles as stated by Equation (2.2).

A multigroup approach, based on the Boltzmann theory of gases, is used to model the disperse phase (Carrica et al. 1999), where bubbles of similar sizes are grouped together in discrete groups. The resulting multigroup equation is:

$$\frac{\partial N_g}{\partial t} + \nabla \cdot \left(\boldsymbol{u}_g N_g \right) = \nabla \cdot \left(\left(\frac{\nu_t}{Sc_b} + \nu_p \left(\alpha_d \right) \right) \nabla N_g \right) + \beta_g + \chi_g + S_g \tag{2.3}$$

where g is the group number, $g = 1,...,G$, and G is the number of discrete bubble size groups. The bubble number density N_g is the number of bubbles per unit volume in group g. β_g, χ_g, S_g are the source terms due to bubble breakup, bubble coalescence, and bubble entrainment, respectively. Gas void fraction is a derived quantity computed as

$$\alpha_d = \sum_{g=1}^{G} v_g N_g \tag{2.4}$$

with v_g the group-g bubble volume and relates to the continuous phase void fraction by $\alpha_c = 1 - \alpha_d$. Turbulent dispersion and bubble packing are modeled as dispersive terms with effective viscosities ν_t / Sc_b and ν_p with Sc_b a bubble Schmidt number. The purpose of the packing diffusivity ν_p is to model the dispersion of bubbles due to the action of random collisions with other bubbles as the void fraction increases. These collisions have been modeled in the past for particle flows as collision forces (Gidaspow 1994). Similarly, turbulence dispersion can be modeled using a volumetric force (Lopez de Bertodano 1994, Carrica et al. 1999) that for small bubbles it can be shown to be equivalent to a diffusive term in Equation (2.3) (Moraga et al. 2003). In this work the dispersion of bubbles due to random collisions is modeled using a diffusive term following the ideas for turbulent dispersion. The model proposed in this work has the form

$$\nu_p = V_T(d_{32}) d_{32} \beta(\alpha_d) \tag{2.5}$$

with d_{32} the Sauter diameter, $V_T(d_{32})$ the terminal velocity at this bubble size and $\beta(\alpha_d)$, with the nondimensionalization in Equation (2.5), an assumed universal function of void fraction that goes to infinity as void fraction approaches a hundred percent.

In analogy to the dispersive forces due to turbulence, the packing force term in Equation (2.1) can be obtained for the simple case in which bubbles rise against a wall only due to buoyancy:

$$\alpha_d \boldsymbol{P} = \sum_g \alpha_g \boldsymbol{P}_g = -\sum_g \hat{C}_{D,g} V_{T,g} \nu_p \nabla \alpha_g \tag{2.6}$$

where $\hat{C}_{D,g}$ is a group-g drag coefficient defined in the work by Castro (2011), $V_{T,g}$ is the bubble terminal velocity for group g and $\alpha_g = v_g N_g$ is the void fraction for group g. Lacking experimental data to choose a functional form for $\beta(\alpha_d)$ and in analogy to work in fluidized beds (Gidaspow 1994), here an ad-hoc model is proposed which increases with void fraction but does not go to infinity for numerical stability reasons

$$\beta(\alpha_d) = 50\begin{cases} 0 & \alpha_d \le 0.15 \\ 5(\alpha_d - 0.15)^2 & 0.15 < \alpha_d \le 0.70 \\ 20(\alpha_d - 0.7) + 1.51 & 0.70 < \alpha_d \le 0.85 \\ 100(\alpha_d - 0.85) + 4.51 & \alpha_d > 0.85 \end{cases} \tag{2.7}$$

where the multiplication factor is calibrated for problems of rising bubbles towards a wall to avoid void fraction to reach 100%. The momentum equation for group-g can be written as (Carrica et al. 1999):

$$C_{VM}\left[\frac{\partial \boldsymbol{u}_g}{\partial t} + (\boldsymbol{u}_g \cdot \nabla)\boldsymbol{u}_g - \left(\frac{\partial \boldsymbol{u}_c}{\partial t} + (\boldsymbol{u}_c \cdot \nabla)\boldsymbol{u}_c\right)\right] + \frac{3}{8}\frac{C_{D,g}}{R_g}\|\boldsymbol{u}_{r,g}\|\boldsymbol{u}_{r,g} = -\nabla p_c + \left(\left(1 - \frac{\rho_d}{\rho_c}\right)\frac{\hat{k}}{Fr^2}\right) - C_L \boldsymbol{u}_{r,g} \times \nabla \times \boldsymbol{u}_c \tag{2.8}$$

where the inertial and viscous terms are neglected. $\boldsymbol{u}_{r,g} = \boldsymbol{u}_g - \boldsymbol{u}_c$ is the group-g slip velocity and $C_{VM}, C_{D,g}, C_L$ are the modeling coefficients for virtual mass, drag and lift, respectively.

In addition to the conservation of momentum and mass for each phase, the complete model includes a blended k-ε/k-ω model with detached eddy simulation (DES) capabilities for turbulence modeling (Xing et al. 2007) and a single-phase level set method to model free surface flows (Carrica et al. 2007b). The multigroup methodology for bubbly two-phase flows is thoroughly described in Castro et al. (2013a, 2013b) and references therein.

CHAPTER 3 NUMERICAL METHODS

It is well known that the staggered arrangement of pressure and velocity leads to a very stable pressure-velocity coupling that allows to preserve mass to machine precision. This scheme is attractive since no special care on how fluxes are computed needs to be taken to obtain a strong pressure-velocity coupling. This is particularly important for applications with density changes and in particular for high density ratios as in the case of free surface flows (Dommermuth et al. 2006). On the other hand, the collocated arrangement of velocity and pressure provides a configuration of simpler implementation since only one grid for all variables can be used in contrast to having a different grid for each velocity component and pressure separately. While this does not represent a particular advantage for codes using Cartesian grids, it does make a significant difference for implementations using curvilinear grids for which significantly more complex geometric metrics are needed (Thompson et al. 1985). The evaluation of several metrics is not only cumbersome but requires a significantly larger amount of computations and memory. In addition, curvilinear grids can be body fitted allowing the representation of complex geometries and proper refinement normal to solid walls to resolve boundary layers. This technique has proven very effective in combination with overset methods (Carrica et al. 2007a, Buning and Pulliam 2011) allowing to represent even more complex geometries, multibody simulations with motions and control surfaces and even localized refinement while still exploiting highly efficient strategies for structured grids (Carrica et al. 2010). The implementation of overset with staggered arrangements would require the computation of separate Domain Connectivity Information (DCI) for four grids corresponding to the three velocity components and pressure. In this regard collocated methods are more convenient since only one DCI needs to be computed for all variables. However, the collocated arrangement of variables does not provide the natural coupling of pressure and

velocity offered by staggered grids. Decoupling between pressure and velocity may occur if no special care is taken in the computation of face fluxes.

In their pioneer work, Rhie and Chow (1983) presented a method that estimates face velocities by interpolation from nodal velocities. Regardless of the interpolation used to compute face fluxes, with collocated methods mass is not preserved exactly. As a result, these small errors in the conservation of mass lead to mass sinks or sources that ultimately may result in the divergence of the system of equations or unphysical pressure oscillations. This issue can usually be overcome in single phase codes leading to very robust implementations that provide accurate results for practical applications (Mofidi and Carrica 2014)). However, these mass conservation errors may be very unforgiving for applications involving large density changes or free surface flows.

In addition to errors in mass conservation that may or may not be acceptable depending on the application, the original Rhie and Chow interpolation suffers of spurious pressure oscillations that worsen as the time step is decreased (Shen et al. 2001, Pascau, 2011) due to an inappropriate interpolation for face fluxes. In the past different alternatives were proposed by several authors to compute face fluxes to remove pressure oscillations. Kothe (1999) estimated face fluxes using high order Taylor expansions. Aksoy and Chen (1992) proposed a momentum-weighted interpolation method to estimate face velocities. Thorough reviews of different alternatives are presented by Miettinen (1997) and by Pascau (2011).

This work focuses on the development of a robust numerical strategy for the solution of high void fraction two-phase bubbly flows with free surface on overset curvilinear grids. The main application targeted in this paper is the simulation of bubbly flows around full scale surface ships though the techniques presented herein have a much broader range of applications. These are very challenging flows from the computational point of view given that they involve high Reynolds number free surface flows spanning a wide range of spatial and temporal scales, complex geometries that move in reaction to the

flow and high void fraction levels caused by massive air entrainment and accumulation of bubbles as they rise towards the hull. Bubble diameters range from a few micrometers to several millimeters and therefore a polydisperse model to describe several bubble sizes is adopted (Castro and Carrica 2013a). This model adds a considerable number of unknowns tightly coupled by a highly non-linear system of equations further increasing the computational cost.

In the simulation of bubbly two-phase flows pressure, velocity and void fraction are tightly coupled by mass conservation. Small errors in mass conservation admissible for practical single phase flow simulations become intolerable for two-phase flows especially with high void fraction. Yoeh and Tu (2010) reviewed several variations of the SIMPLE pressure-velocity coupling method extended to multi-phase flows. Castro and Carrica (2013a) and Castro (2011) extended the projection method from Huang et al. (2008) for the simulation of polydispersed bubbly flows.

This work extends the work by Castro (2011), resulting in a two-way coupled methodology for the simulation of bubbly two-phase flows with free surface and high void fraction. The pressure-velocity coupling is based essentially on the projection method by Rhie and Chow (1983) with face fluxes computed as in Lien and Leschziner (1994). The strategy presented herein uses a hybrid approach in which staggered face velocities are used for transport and pressure-velocity coupling while the momentum equation is solved on a collocated grid. The methodology is presented in Section 3.1. Section 3.2 presents an alternative form of mass conservation for a strong and robust coupling of void fraction with pressure and velocity. As described in Section 3.2, void fraction coupling with pressure and velocity is achieved by solving a predictor step within a fixed-point iteration. Implementation details near boundaries and overset interfaces are given in Section 3.3. In Section 3.4 the balanced forced method developed by Montazeri and Ward (2014) to avoid the generation of spurious currents is extended for curvilinear grids. A two-way coupled solution with high void fraction is achieved even when very stiff non-linear packing forces

accounting for collision between bubbles are accounted for. The methodology allows integrating the full bubbly phase model all the way into solid boundaries where grid aspect ratios often result in stability issues. Such a capability can then be used in the development of near wall bubbly flows models, an area for which much more research is needed.

The code REX is used in this work. REX uses multiblock structured curvilinear body-fitted grids with a dynamic overset capability that allows the placement of local refinements where needed and to perform computations with large amplitude motions (Carrica et al. 2007a, 2010). A single-phase level set approach is used for free surface modeling (Carrica et al. 2007b). Turbulence is modeled using a blended k-ε/k-ω model with DES capabilities (Xing et al. 2007). The governing equations are discretized using a control volume/finite differences approach on a collocated grid in space. The convection terms are discretized with linear upwind biased or TVD schemes (Ismail et al. 2010). SUGGAR (Noack 2005) is used to dynamically obtain overset the domain connectivity information. Either projection (Bell et al. 1991) or PISO (Issa 1986) are used for pressure-velocity coupling. A coordinate transformation from the physical domain to the computational domain is used to discretize the equations, where control volumes in the computational domain are cubes with unit volume and unit area on each face (Thompson et al. 1985).

The methodology is tested for stability and accuracy in Section 3.6 including convergence studies on a series of 1D and 2D cases reaching over 96% void fraction. Finally, the method is applied to the simulation of a full scale polydisperse bubbly flow around ships for which experimental data in the near field region is available.

3.1 Pressure-velocity coupling in collocated grids

The pressure-velocity coupling scheme used in this work is based on the second order projection method by Bell et al. (1996) using linear interpolation to compute face fluxes as in Rhie and Chow (1983). This scheme as implemented for general curvilinear

grids in REX will be referred to as the collocated scheme (CS). Improvements to this scheme are presented and the resulting strategy is referred to as hybrid scheme (HS).

3.1.1 Discretization in general curvilinear coordinates

The governing equations are transformed from physical coordinates x_i into non-orthogonal coordinates ξ_i with unit cells in each direction. A partial transformation is used in which only the spatial coordinates are transformed leaving the velocity components in the original physical space. Here only the needed notation is introduced referring the interested reader to Thompson et al. (1985). In this transformation the covariant base vector $\boldsymbol{a}_i = \partial \boldsymbol{x} / \partial \xi_i$ length equals the cell size in the *i*-th direction. The normal vector to constant *i*-planes is then given by $\boldsymbol{b}^i = (b_1^i, b_2^i, b_3^i) = \boldsymbol{a}_j \times \boldsymbol{a}_k$ with indices i, j, k in cyclic order and its modulus being the cell face area. The Jacobian of the transformation $J = \boldsymbol{a}_1 \cdot (\boldsymbol{a}_2 \times \boldsymbol{a}_3)$ provides the cell volume. The geometric quantities b_j^i and J fully specify the transformation. Given a vector $\boldsymbol{t}$ the contravariant vector $\breve{t}_i = \boldsymbol{b}^i \cdot \boldsymbol{t}$ represents the flux of that vector across a face in the *i*-th direction, in indicial notation $\breve{t}_i = b_j^i t_j$. The gradient of a scalar ϕ is computed as

$$\partial_i \phi = \frac{b_i^j}{J} \frac{\partial \phi}{\partial \xi_j} \tag{3.1}$$

and the contravariant gradient is computed as

$$\breve{\nabla}_i \phi = e_{ij} \frac{\partial \phi}{\partial \xi_j} \qquad e_{ij} = \frac{b_l^i b_l^j}{J} \tag{3.2}$$

3.1.2 Projection method

Regardless of the spatial and temporal schemes used, the discretization of the momentum conservation Equation (2.1) at node p for the i-th component leads to a discrete system of the form

$$\frac{\omega_n \alpha_{c,p}^n}{\delta t} u_{p,i}^n + \partial_i p_p^n = A_{p,i} u_{p,i}^n + \sum_{nb} A_{nb,i} u_{nb,i}^n + S_{p,i} - \frac{1}{\delta t}\left(\omega_{n-1}\alpha_{c,p}^n u_{p,i}^{n-1} + \omega_{n-2}\alpha_{c,p}^n u_{p,i}^{n-2}\right) \quad (3.3)$$

where the summation over nb includes all neighbor nodes within the discretization stencil. The coefficients ($A_{p,i}$, $A_{nb,i}$) result from the spatial discretization of convection and diffusion terms while ω_l are weights arising from the time marching discretization. The source term $S_{p,i}$ includes body forces as well as cross diffusion terms originated from the discretization of the diffusion terms in a non-orthogonal system. These are usually small and are treated as known quantities within a fixed-point iteration. For convenience, the following shorthand variables are defined

$$\begin{aligned} \tilde{V}_{p,i}^n &= \sum_{nb} A_{nb,i} u_{nb,i}^n + S_{p,i} \\ V_{p,i}^n &= A_{p,i} u_{p,i}^n + \tilde{V}_{p,i}^n \\ F_{p,i} &= \frac{1}{\delta t}\left(\omega_{n-1}\alpha_{c,p}^{n-1} u_{p,i}^{n-1} + \omega_{n-2}\alpha_{c,p}^{n-2} u_{p,i}^{n-2}\right) \end{aligned} \quad (3.4)$$

thus Equation (3.3) can be written as

$$\begin{aligned} \frac{\omega_n \alpha_{c,p}^n}{\delta t} u_{p,i}^n + \partial_i p_p^n &= \tilde{V}_{p,i}^n + A_p u_{p,i}^n - F_{p,i} \\ &= V_{p,i}^n - F_{p,i} = w_{p,i}^n \end{aligned} \quad (3.5)$$

where the diagonal term A_p is the same for all components if a linear convection scheme is used, i.e. $A_{p,i} = A_p$ and the pseudo-momentum w_i is defined. An approximate discrete form of the momentum equation can be obtained using the latest available pressure p^* in Equation (3.5) to obtain a *predicted* velocity $\boldsymbol{u}^*$ that in general does not satisfy mass conservation

$$\frac{\omega_n \alpha_{c,p}^n}{\delta t} u_{p,i}^* + \partial_i p_p^* = \tilde{V}_{p,i}^* + A_p u_{p,i}^* - F_{p,i} = w_{p,i}^* \quad (3.6)$$

It is key to notice that Equation (3.6) is discretized at the cell centers. A momentum equation at the faces is not available. Assume at this point that such an equation can be written for face f as

$$\frac{\omega_n \alpha_{c,f}^n}{\delta t} u_{f,i}^n + \partial_i p_f^n = \tilde{V}_{f,i}^n + A_f u_{f,i}^n - F_{f,i} = w_{f,i}^n \tag{3.7}$$

Using contravariant fluxes the conservation of mass Equation (2.2) can be discretized as

$$\sum_f \alpha_{c,f}^n \breve{u}_{f,i}^n = -J_p \frac{\partial \alpha_{c,p}^n}{\partial t} \tag{3.8}$$

where the summation includes all cell faces $f = u, d, w, e, s, n$ and the flux components are $i = 1$ for $f = u, d$, $i = 2$ for $f = w, e$ and, $i = 3$ for $f = s, n$. The contravariant fluxes in Equation (3.8) can be obtained by taking the dot product of Equation (3.7) with $\boldsymbol{b}^i$

$$\frac{\omega_n \alpha_{c,f}^n}{\delta t} \breve{u}_{f,i}^n + \breve{\nabla}_i p_f^n = \breve{w}_{f,i}^n \tag{3.9}$$

where the contravariant pressure gradient is computed using Equation (3.2). Combining Equations. (3.8) and (3.9) results in a Poisson equation for the pressure

$$\sum_f e_{ij,f} \left. \frac{\partial p^n}{\partial \xi_j} \right|_f = J_p \frac{\omega_n}{\delta t} \frac{\partial \alpha_{c,p}^n}{\partial t} + \sum_f \breve{w}_{f,i}^n \tag{3.10}$$

Different alternatives exist to obtain the approximate momentum equation at the face in Equation (3.7) using the predicted velocity from Equation (3.6) and leading to various definitions of $\breve{w}_{f,i}^n$ in Equation (3.10). These alternatives have a strong impact in the stability and convergence of the method and are the subject of the next two subsections. Coupling with void fraction through its time derivative in Equation (3.10) is also a crucial since a weak coupling may lead to the divergence of the system especially at high void fractions. This is treated in Section 3.2.

3.1.3 Collocated scheme

In the collocated scheme the pseudo-momentum $\breve{w}_{f,i}^n$ needed in the right hand side of Equation (3.10) is first computed at the nodes using the approximation $w_{p,i}^n = w_{p,i}^*$ with $w_{p,i}^*$ computed from Equation (3.6) after the predictor step as

$$w_{p,i}^{*} = \frac{\omega_n \alpha_{c,p}^{n}}{\delta t} u_{p,i}^{*} + \partial_i p_p^{*} \tag{3.11}$$

The value at the face is then obtained as $w_{f,i} = \bar{w}_i$ with the overbar denoting interpolation from nodal values. Once pressure is computed from Equation (3.10), velocity is updated from Equation (3.5) as

$$u_{p,i}^{n} = \frac{\delta t}{\omega_n \alpha_{c,p}^{n}} (w_{p,i}^{*} - \partial_i p_p^{n}) \tag{3.12}$$

This strategy was used by Huang et al. (2007) for free surface flows and by Castro (2011) for two-phase bubby flows. This approach, however, results in pressure oscillations that can become acute as time step decreases (Shen et al. 2001). In presence of high void fraction the problem dramatically increases.

The divergence of the solution at small time steps can be explained by noticing that the discrete divergence of w_i in Equation (3.10) contains two contributions, one of which depends on the time step. Applying linear interpolation to find $w_{f,i}$ on Equation (3.6)

$$w_{f,i}^{n} = \overline{w_i^{*}} = \overline{V_i^{*}} - \overline{F_i} = V_{f,i}^{*} - F_{f,i} \tag{3.13}$$

the discrete divergence of $w_{f,i}^{n}$ in Equation (3.10) is

$$\sum_f \breve{w}_{f,i}^{n} = \sum_f \sum_j b_i^j w_{f,j}^{n} = \sum_f \breve{V}_{f,i}^{*} - \sum_f \breve{F}_{f,i} \tag{3.14}$$

According to mass conservation, Equation (3.8), and the definition of F_i given by Equation (3.4), the last term in Equation (3.14) reduces to

$$\sum_f \breve{F}_{f,i} = -\frac{J_p}{\delta t} \left(\omega_{n-1} \frac{\partial \alpha_{c,p}^{n-1}}{\partial t} + \omega_{n-2} \frac{\partial \alpha_{c,p}^{n-2}}{\partial t} \right) \tag{3.15}$$

and therefore should be zero for a steady void fraction. However, even for single phase systems, the term in Equation (3.15) is in general not zero given that $F_{f,i}$ is computed by interpolation of nodal values. This error is amplified when divided by δt in Equation (3.15) and feeds into the pressure Poisson equation in Equation (3.10). This problem can many times go unnoticed specially for the time steps used in practical computations. It does

however become a source of instabilities for high void fraction two-phase flows and it thus must be addressed.

3.1.4 Hybrid scheme

The scheme presented in this section solves a nodal (collocated) momentum equation while computing mass-preserving face velocities used for convection and pressure coupling as in a staggered approach. The computational cost increases slightly, since while only three velocity components need to be stored in CS at the nodes, the hybrid scheme (HS) presented herein stores three additional face velocities.

According to Pascau's (2011) analysis for single phase flow, improper interpolation for cell face velocities from node values can result in a scheme with time step dependence. Here we choose the approach originally implemented by Lien and Leschziner (1994) for single phase flow and later used for interfacial flows by Udaykumar et al. (1997) on 2D Cartesian grids. It's convergence at small time steps was demonstrated by Yu et al. (2002). This method computes a predicted face velocity $u^*_{f,i}$ from an algebraic momentum equation at the cell faces obtained as

$$\frac{\omega_n \alpha^n_{c,f}}{\delta t} u^*_{f,i} + \partial_i p^*_f = \tilde{V}^*_{f,i} + A_f u^*_{f,i} - F_{f,i} = w^*_{f,i} \tag{3.16}$$

with $\tilde{V}^*_{f,i} = \overline{\tilde{V}^*_i}$ and $A_f = \bar{A}$, and the face void fraction computed by linear interpolation. Another option to estimate $\tilde{V}^*_{f,i}$ is from $\tilde{V}^*_{f,i} / A_f = \overline{\tilde{V}^*_i / A}$, which is claimed to be unconditionally consistent by Pascau in 1D test (2011). The two methods show identical results for applications in this thesis. From Equation (3.16), $u^*_{f,i}$ is explicitly computed as

$$u^*_{f,i} = \left(\tilde{V}^*_{f,i} - F_{f,i} - \partial_i p^*_f \right) / \left(\frac{\omega_n \alpha^n_{c,f}}{\delta t} - A_f \right) \tag{3.17}$$

Then the momentum term in Equation (3.7) is estimated as $w^n_{f,i} = w^*_{f,i}$, with $w^*_{f,i}$ computed from Equation (3.16). This momentum term as needed in the Poisson Equation (3.10), as well as the face velocities, can be evaluated directly in contravariant form as

$$\breve{\tilde{V}}^*_{f,i} = \sum_j b^i_j \tilde{V}^*_{f,j}$$

$$\breve{F}_{f,i} = \frac{1}{\delta t}\left(\omega_{n-1}\alpha^{n-1}_{c,f}\breve{u}^{n-1}_{f,i} + \omega_{n-2}\alpha^{n-2}_{c,f}\breve{u}^{n-2}_{f,i}\right) \tag{3.18}$$

$$\breve{u}^*_{f,i} = \sum_j b^i_j u^*_{f,j} = \left(\breve{\tilde{V}}^*_{f,i} - \breve{F}_{f,i} - \breve{\nabla}_i p^*_f\right) / \left(\frac{\omega_n \alpha^n_{c,f}}{\delta t} - A_f\right)$$

$$\breve{w}^*_{f,i} = \sum_j b^i_j w^*_{f,j} = \breve{\tilde{V}}^*_{f,i} + A_f \breve{u}^*_{f,i} - \breve{F}_{f,i} \tag{3.19}$$

With the pseudo-momentum computed from Equation (3.19), the pressure is computed from Equation (3.10). Nodal velocities are updated using Equation (3.12) and in general do not satisfy mass conservation. However, contravariant face velocities do satisfy mass conservation exactly, after being updated from the contravariant version of Equation (3.16)

$$\breve{u}^n_{f,i} = \frac{\delta t}{\omega_n \alpha^n_{c,f}}(\breve{w}^*_{f,i} - \breve{\nabla}_i p^n_f) \tag{3.20}$$

The convective face velocities that must be stored in a general curvilinear approach are the contravariant face velocities. These are used in the set of equations in Equation (3.19) as well on the discretization of the convection term of any transport equation. If the contravariant velocities $\breve{u}^{n-1}_{f,i}$ and $\breve{u}^{n-2}_{f,i}$ are also stored, the computation of $\breve{F}_{f,i}$ in Equation (3.19) satisfies Equation (3.15) exactly, eliminating time step dependence.

3.2 Two phase coupling strategy

In the pressure-velocity coupling schemes presented above the void fraction was assumed to be known. However, in a two-way coupled bubbly flow simulation the void fraction is computed from the group number densities, Equation (2.4). These in turn are solved from the multigroup transport Equation (2.3). The void fraction affects the flux of liquid momentum, which interacts with pressure through mass conservation. At the same time, changes in void fraction affect the pressure through the mass conservation Equation (3.10). This coupling becomes very tight especially at high void fraction levels.

In Castro and Carrica (2013a) the full system is solved using a partitioned approach in which each model is solved in sequence within a fixed-point iteration: turbulence, number densities and void fraction, level-set, and finally liquid velocity and pressure. The iteration is repeated until a converging criteria is reached. The void fraction time derivative in Equation (3.10) is obtained before computing the pressure. The pressure, however, modifies the liquid velocity field which in turn is responsible for bubble transport. This approach may not converge for high void fraction levels. Castro and Carrica (2013a) show how to treat bubble compressibility, but the approach fails for void fraction levels higher than 40%. The divergence of this explicit approach is demonstrated in Section 3.6.2.2.

A new strategy is developed here for a strong pressure-velocity-void fraction coupling. The key idea is to write an evolution equation for the total void fraction that can be used in a predictor step to estimate the void fraction at the next time step. In addition, when combined with mass conservation in Equation (2.2), a new form of mass conservation results where the void fraction time derivative is eliminated. Multiplying Equation (2.3) by the group volume and summing over all groups, a transport equation for total void fraction α_d is obtained

$$\begin{aligned} &\frac{\partial \alpha_d}{\partial t} + \nabla \cdot \left(\boldsymbol{u}_d \alpha_d \right) = \nabla \cdot \left[\left(\frac{\nu_t}{Sc_b} + \nu_p \right) \nabla \alpha_d \right] + S_d \\ &\boldsymbol{u}_d = \frac{1}{\alpha_d} \sum \boldsymbol{u}_g \alpha_g \end{aligned} \tag{3.21}$$

where $\boldsymbol{u}_d$ is the void fraction effective velocity. Breakup and coalescence sources are eliminated since they preserve bubble mass. Adding Equations. (2.2) and (3.21) yields

$$\begin{aligned} &\nabla \cdot \boldsymbol{u}_c = \nabla \cdot \left[\left(\frac{\nu_t}{Sc_b} + \nu_p \right) \nabla \alpha_d - \boldsymbol{u}_{d,r} \alpha_d \right] + S_d \\ &\boldsymbol{u}_{d,r} = \boldsymbol{u}_d - \boldsymbol{u}_c \end{aligned} \tag{3.22}$$

where the time derivatives cancel out since $\alpha_c + \alpha_d = 1$. $\boldsymbol{u}_{d,r}$ is the relative velocity between the average bubble velocity and the liquid. This equation strongly couples velocity

with void fraction since bubble transport is already used in its formulation. In addition, the right hand side of Equation (3.22) is weakly dependent on the liquid phase velocity, allowing to treat velocity variations in a strongly implicit way. Lastly, large volume changes that would otherwise be detected by the time derivative in Equation (3.10) are implicitly included. Equation (3.22) represents an alternative form of the mass conservation equation and is used to replace Equation (2.2).

The contravariant velocity needed to compute the discrete divergence in Equation (3.22) is obtained dividing Equation (3.9) by the void fraction

$$\frac{\omega_n}{\delta t}\breve{u}^n_{f,i} + \frac{1}{\alpha^n_{c,f}}\breve{\nabla}_i p^n_f = \frac{\breve{w}^n_{f,i}}{\alpha^n_{c,f}} \tag{3.23}$$

Summing over all faces, and using the discrete version of Equation (3.22) for the divergence of the velocity, produces a new pressure Poisson equation as

$$\begin{aligned}\sum_f \frac{e_{ij,f}}{\alpha^n_{c,f}}\frac{\partial p^n}{\partial \xi_j}\bigg|_f &= -\frac{\omega_n}{\delta t}\sum_f \breve{u}^n_{f,i} + \sum_f \frac{\breve{w}^n_{f,i}}{\alpha^n_{c,f}} \\ &= -\frac{\omega_n}{\delta t}\left(\sum_f \breve{q}_{f,i} + J_p S_d\right) + \sum_f \frac{\breve{w}^n_{f,i}}{\alpha^n_{c,f}}\end{aligned} \tag{3.24}$$

with the contravariant slip flux defined as

$$\breve{q}_{f,i} = \left(\frac{\nu_{t,f}}{Sc_b} + \nu_{p,f}\right)\breve{\nabla}_i \alpha_{d,f} - \alpha_{d,f}\,\breve{u}_{d,r}\big|_{f,i} \tag{3.25}$$

It is important to use the same convection/diffusion schemes in Equation (3.25) as in Equation (3.21), to avoid the introduction of a spurious divergence in the liquid velocity field. To understand the reason, consider a steady state problem for which $\boldsymbol{u}_c = 0$ and $S_d = 0$. In steady state the discrete version of Equation (3.21) implies that the divergence of the discrete slip flux, computed using the convection schemes in Equation (3.21), is zero, i.e. $\sum_f \breve{q}_{f,i} = 0$. Exactly zero divergence of the velocity can only be achieved if the same approximations are used for $\breve{q}_{f,i}$ in Equations (3.22) and (3.24).

The scheme then proceeds with the projection of face velocities, Equation (3.20), and node velocities, Equation (3.12). The procedure for the proposed two-phase projection solver implemented in REX is summarized in Figure 3.1.

Initialize previous time steps

- $\breve{u}_{f,i}^{n-2} \leftarrow \breve{u}_{f,i}^{n-1}$, $\breve{u}_{f,i}^{n-1} \leftarrow \breve{u}_{f,i}^{n}$
- $u_{p,i}^{n-2} \leftarrow u_{p,i}^{n-1}$, $u_{p,i}^{n-1} \leftarrow u_{p,i}^{n}$
- $\alpha_d^{n-2} \leftarrow \alpha_d^{n-1}$, $\alpha_d^{n-1} \leftarrow \alpha_d^{n}$

Main non-linear iteration

- Solve turbulence model equations.
- Solve level-set transport +re-initialization equations.
- Solve for group-g velocity from $\boldsymbol{u}_g^n$ Equation (2.8).

Pressure-velocity-void fraction solver

- Void fraction predictor Equation (3.21). Iterations are needed to converge packing model.
- Predict node velocity $\boldsymbol{u}_p^*$ from Equation (3.6).

Compute terms for RHS in pressure equation

- Slip flux $\bar{q}_{f,i}$ from Equation (3.25).
- Predicted contravariant face velocity $\breve{u}_{f,i}$ from Equation (3.18).
- Contravariant pseudo-momentum at the face $\breve{w}_{f,i}$ from Equation (3.19).

Pressure solver

- Build Poisson equation matrix and RHS from Equation (3.24).
- Solve for pressure p^n.

Compute pressure gradient

- Pressure gradient $\partial_i p_p$ at the nodes.
- Contravariant pressure gradient $\breve{\nabla}_i p_f^n$ at faces.

Update velocities

- Node velocities $u_{p,i}^n$ from Equation (3.12).
- Contravariant face velocities $\breve{u}_{f,i}^n$ from Equation (3.20).

End pressure-velocity-void fraction solver

End main non-linear iteration

- Multigroup solver for number densities N_g for Equation (2.3).
- Update void fraction α_d^n from Equation (2.4).

Figure 3.1: Coupling strategy for the main time step solver. To save computational cost, a void fraction predictor is used within a fixed-point iteration loop, coupling pressure, velocity, and void fraction. At the end of the main non-linear loop, the void fraction is updated with the full multigroup model.

3.2.1 Semi-Implicit treatment of the packing force

The packing force term is determined by the void fraction of each group. In the proposed two phase coupling strategy, it cannot be discretized implicitly as the buoyancy term during fixed-point iteration given that the multigroup Equation (2.6) is solved at the end of the fixed-point inner iteration. The highly nonlinear dependence on α_d may cause instabilities when treated explicitly. Here the following semi-implicit method is proposed to discretize this term. The packing force can be written as,

$$\begin{aligned}\alpha_d \boldsymbol{P}^{n+1} &= -\sum_g \hat{C}_{D,g} V_{T,g} \nu_p^{n+1} \nabla \alpha_g^{n+1} \\ &= -\sum_g \hat{C}_{D,g} V_{T,g} \nu_p^{n+1} \nabla \left(\alpha_d^{n+1} \Omega_g^{n+1} \right) \\ &\approx -\sum_g \hat{C}_{D,g} V_{T,g} \nu_p^{n+1} \left(\Omega_g^n \nabla \alpha_d^{n+1} + \alpha_d^{n+1} \nabla \Omega_g^n \right)\end{aligned} \tag{3.26}$$

where $\Omega_g = \alpha_g / \alpha_d$ is the void fraction size distribution. In the fixed-point non-linear iteration, ν_p and α_d in Equation (3.26) can use latest available values while Ω_g uses the group information from last time step.

3.3 Boundary conditions

The formulation derived above is valid only for inner nodes for which a momentum equation such as Equation (3.3) is valid. For these inner nodes the pseudo-momentum fluxes $\breve{w}_{f,i}$ and the contravariant pressure gradients are well defined for all faces, and the pressure Poisson equation in Equation (3.24) is fully specified.

In an overset free surface code such as REX, a computational node is either an interior node, a boundary condition node, a node on the air side or a fringe point interpolated from another grid, see (Carrica et al., 2007a; Carrica et al., 2007b) for details. This is illustrated in Figure 3.2 where a sample *interior cell* is labeled as p. Cells for which a momentum equation is not available are generally referred as *boundary condition cells* and samples are labeled with b in Figure 3.2. Cells sharing at least one of their faces with

a neighbor boundary condition cell are referred as *transition cells* (squares) and samples are labeled with q in Figure 3.2.

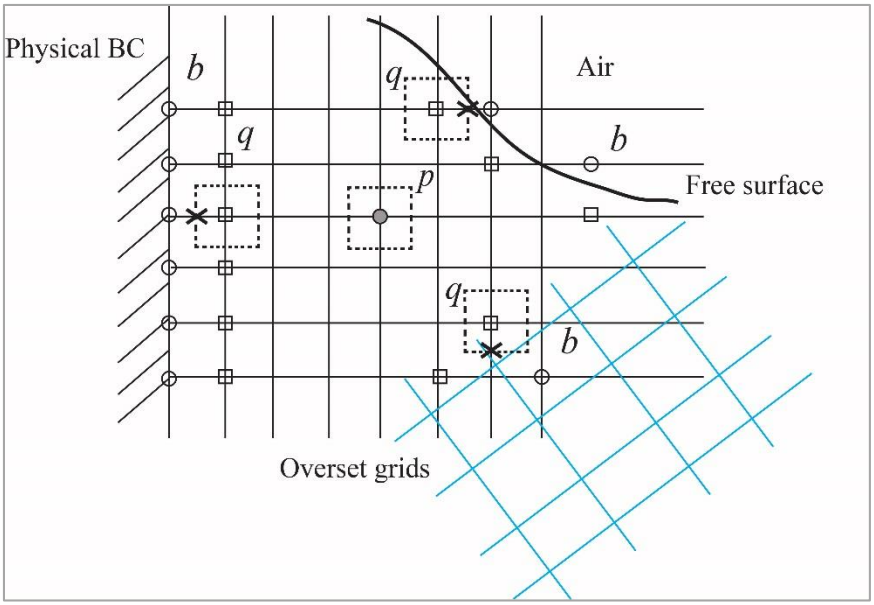

Figure 3.2: Cells definition at grid points next to a boundary condition.

For these nodes the momentum equation, Equation (3.5), is well defined and the predictor step is valid. The Poisson equation, Equation (3.24), can be written as

$$\sum_f \frac{\breve{\nabla}_i p_f^n}{\alpha_{c,f}^n} = -\frac{\omega_n}{\delta t}\left(\sum_f \breve{q}_{f,i} + J_p S_d\right) + \sum_f \frac{\breve{w}_{f,i}^n}{\alpha_{c,f}^n} \tag{3.27}$$

and is valid even for transition nodes, though the computation of the contravariant fluxes at faces between inner and transition nodes (crosses in Figure 3.2) needs to be revised.

Boundary condition nodes (circles) in Figure 3.2 do not have a momentum equation but the velocity is either imposed, interpolated from another grid, or computed from a particular boundary condition. As a consequence, the diagonal coefficient A_f in Equation (3.16) and a face momentum equation are not defined, and neither the face velocity $\breve{u}_{f,i}^n$ nor the pseudo-momentum $\breve{w}_{f,i}^n$, needed in Equation (3.27), can be computed. In this work

a face momentum equation at these faces is obtained by interpolation between the transition cell momentum equation and the boundary condition

$$\frac{\omega_n \alpha^n_{c,\kappa}}{\delta t} u^n_{\kappa,i} + \kappa \partial_i p^n_\kappa = \kappa \left(\tilde{V}^n_{q,i} + A_q u^n_{q,i} - F_{q,i} \right) + (1-\kappa) \frac{\omega_n \alpha^n_{c,b}}{\delta t} u^n_{bc,i} \tag{3.28}$$

where $\kappa \in [0,1]$ is a weighting factor function of the distance between a transition node q and a boundary node b in Figure 3.2. Equation (3.28) reduces to the boundary condition $u^n_{b,i} = u^n_{bc,i}$ for $\kappa = 0$ and to the nodal momentum equation, Equation (3.5), for $\kappa = 1$. In the curvilinear coordinate system the face between these two cells is located at $\kappa = 1/2$ and Equation (3.28) reduces to

$$\frac{\omega_n \alpha^n_{c,f}}{\delta t} u^n_{f,i} + \frac{1}{2} \partial_i p^n_f = \frac{1}{2} \left(\tilde{V}^n_{q,i} + A_q u^n_{q,i} - F_{q,i} \right) + \frac{1}{2} \frac{\omega_n \alpha^n_{c,b}}{\delta t} u^n_{bc,i} = w_{f,i} \tag{3.29}$$

Equation (3.29) is used to replace the face momentum equation in Equation (3.7) allowing computation of the pseudo-momentum $\breve{w}^n_{f,i}$ at these transitional faces for Equation (3.27). Notice that, for Dirichlet boundary conditions, Equation (3.29) implies that the pressure gradient used in Equation (3.27) is half of what is needed in a normal inner node. This approach allows to treat transitional cells with a unified procedure. Particulars for each boundary condition are discussed below.

3.3.1 No-slip walls and velocity boundary conditions

For node centered codes as REX, boundary cells are actually half cells as depicted in Figure 3.2 and therefore metrics b^i_j and J reflect this. Next to a solid boundary, flow is parallel to the boundary and normal slip fluxes $\breve{q}_{f,i}$ are neglected. In the general case these fluxes are not zero in the tangential directions but are neglected for stability reasons. This approximation is exact at zero void fraction or if the void fraction is solved for boundary control volumes, especially considering how small these cells are in the normal direction for boundary layers where $y^+ \sim 1$. Therefore $\sum_f \breve{q}_{f,i} = 0$ is assumed for these cells. This

condition is equivalent to $\nabla \cdot \boldsymbol{u}_c = 0$ when $S_d = 0$ in Equation (3.27), which enforces conservation of volume.

3.3.2 Free surface nodes

REX uses a single-phase level set method to solve unsteady viscous free surface flows (Carrica et al. 2007b). The velocity in the air is extended from water along the direction normal to the free surface to enforce a zero shear stress condition. Pressure on the air side is imposed such that interpolation on the free surface results on constant atmospheric pressure. As a result, a momentum equation is not solved on these nodes and the approach described in Section 3.3 is applied on nodes one cell within the fluid.

3.3.3 Fringe points

Figure 3.2 depicts a typical transition node q next to a fringe point b for which both velocity and pressure are found by interpolation from another donor grid (Carrica et al. 2007a). The situation is similar to what was described above in that a momentum equation is not available at node b and therefore a face momentum equation is not available on the shared face.

On these cells the pressure Poisson equation is discretized as for any other inner cell as in Equation. (3.27). However, the pseudo-momentum term $\breve{w}^n_{f,i}$ is found by interpolation, i.e. $\breve{w}^n_{f,i} = \breve{\breve{w}}^n_i$, as done in the original collocated scheme (CS) described in Section 3.1.3.

3.4 Balanced force method for volumetric forces

Montazeri and Ward (2014) show that body forces balance the pressure gradient at the faces, not at the nodes. Therefore, if the body force at the nodes for the momentum equation in Equation (3.3) is not consistent with the discrete version of the body forces at the faces, spurious velocities may be induced by an unbalanced pressure gradient. A balanced-forced method is developed in (Montazeri and Ward 2014) to circumvent this

issue. In the two-phase model for bubbly flows, these volumetric forces are the packing force and the net buoyant term in Equation (2.1). In this work the method in (Montazeri and Ward 2014) is extended to curvilinear grids.

To understand the issue, consider a 1D problem where a volumetric force f balances the pressure gradient at steady state. Since the Poisson Equation (3.10) is built from the momentum balance at the faces Equation (3.9) in steady state implies

$$\nabla p_{i+1/2} = \frac{p_{i+1} - p_i}{\Delta x} = \frac{f_i + f_{i+1}}{2} \tag{3.30}$$

$$\nabla p_{i-1/2} = \frac{p_i - p_{i-1}}{\Delta x} = \frac{f_{i-1} + f_i}{2} \tag{3.31}$$

When solving Equation (3.3) , the pressure gradient at node i is

$$\nabla p_i = \frac{1}{2\Delta x}\left(p_{i+1} - p_{i-1}\right) = \frac{1}{2}\left(\nabla p_{i-1/2} + \nabla p_{i+1/2}\right) = \frac{f_{i-1} + 2f_i + f_{i+1}}{4} \tag{3.32}$$

and consequently $\nabla p_i \neq f_i$. If the volumetric force is simply evaluated as f_i, the pressure gradient in the momentum equation is not balanced and spurious velocities occur.

To avoid this inconsistency, Montazeri and Ward (2014) propose to reconstruct volumetric forces at the nodes using face values. In this work the method is extended to curvilinear grids in an approximate way such that it reduces to Montazeri and Ward (2014) method for Cartesian grids. The scheme proposed computes the contravariant body forces at the faces, interpolates them into the cell center and transforms them back to physical space for the momentum equation. Since the total discrete force equals the body force times the cell volume, this quantity is interpolated instead

$$\breve{f}_{i,p} = \left\langle J \frac{\boldsymbol{b}^i}{\left\|\boldsymbol{b}^i\right\|} \cdot \boldsymbol{f} \right\rangle_{i,p} \tag{3.33}$$

where $\langle \cdots \rangle_{i,p}$ takes the mean value between faces upstream/downstream for $i = 1$, west/east for $i = 2$ and north/south for $i = 3$. The contravariant force in Equation. (3.33) is converted to physical space using the inverse of metric b^i_j

$$f_{i,p} = \frac{g_j^i}{J_p \left\| \boldsymbol{g}^i \right\|} \breve{f}_{j,p} \tag{3.34}$$

with the metric inverse defined such that $g_k^i b_j^k = \delta_{i,j}$ and $\boldsymbol{g}^i = (g_1^i, g_2^i, g_3^i)$.

3.5 Near wall treatments

As bubbles are transported under a ship, they can accumulate at the wall due to buoyancy, resulting in high void fraction. Though wall force models in a bubble column, where bubbles move parallel to the wall, were tackled by researchers (Antal et al. 1991, Hosokawa et al. 2002), these models are not applicable to the situation in which bubbles are pushed against a solid surface, since the only forces they account for are related to the presence of a solid boundary to the force of a sphere moving parallel to it. At high Reynolds number flows the grid aspect ratio near the wall is extremely large resulting in very stiff nonlinear equations, which complicates the problem further. Lacking acceptable theoretical or experimental data, a preliminary model is developed to prevent bubbles from penetrating the wall. An extra force is added to the bubble momentum Equation (2.8) for each group

$$\begin{aligned} \mathbf{F}_g^{\mathrm{WF}} &= \left(1 - \frac{\rho_d}{\rho_c}\right) \frac{\hat{\boldsymbol{n}}}{\mathrm{Fr}^2} f\left(R_g\right) \\ f\left(R_g\right) &= \min\left(\frac{d_{\mathrm{w}} - 2R_g}{R_g}, 0\right) \end{aligned} \tag{3.35}$$

where $\hat{\boldsymbol{n}}$ is the normal direction of the wall pointing to the liquid, d_{w} is the distance between the bubble center and the wall. Considering an example in which bubbles rise towards the wall only due to buoyancy, the model predicts zero bubble velocity at $d_{\mathrm{w}} = R_g$ while net velocity pointing away from the wall at $d_{\mathrm{w}} < R_g$. The other forces on bubbles except buoyancy are assumed to linearly decrease to zero from $d_{\mathrm{w}} = 2R_g$ to $d_{\mathrm{w}} = R_g$. This model has expected trends, though the absolute values and functional forms of the equations can be far from how actual forces should look. More work is needed in wall forces, highly relevant for ship hydrodynamics.

3.6 Evaluation Tests and Discussion

The proposed method is tested for 1D and 2D cases with high void fraction and bubble packing. The 1D cases focus on comparing the hybrid and the collocated approaches, and stability and convergence rates are assessed. A 2D polydisperse case illustrates decoupling between groups when the packing force is explicitly treated in the liquid momentum equation and how the semi-implicit method proposed in Section 3.2.1 solves the issue. Finally, the proposed methodology is applied in Chapter 5 to the simulations of full scale ships for which experimental data is available.

3.6.1 Forced radial flow

One-dimensional configurations have been used in the past as benchmarks to examine different pressure-velocity coupling strategies (Pascau 2011) because, though simple, still contain the essential features of the pressure-velocity coupling problem and therefore can be used to highlight potential pitfalls and advantages of different numerical strategies. An interesting solution with a non-constant velocity solution is obtained in cylindrical coordinates. Solutions to the following problem are investigated

$$\frac{\partial \alpha_c}{\partial t} + \frac{1}{r}\frac{\partial}{\partial r}(r\alpha_c u) = 0 \tag{3.36}$$

$$\frac{\partial \alpha_c u}{\partial t} + \frac{1}{r}\frac{\partial}{\partial r}(r\alpha_c u^2) = -\frac{\partial p}{\partial r} \tag{3.37}$$

where r is the radial coordinate and u the velocity in the radial direction. Equations (3.36) and (3.37) are obtained by writing Equations (2.2) and (2.1) in cylindrical coordinates and dropping the functional dependences along the axial and azimuthal directions. The problem is solved within the domain $r \in (1,6)$ with an inlet boundary condition $u(r=1)=1$ and a zero gradient boundary condition at the outer radius. For these tests the void fraction is a known function of space and time of the form

$$\alpha_d(r,t) = tg(r) \tag{3.38}$$

and thus $\partial\alpha_c / \partial t = -g(r)$ in Equation (3.36). Void fraction and velocity are zero at $t = 0$. Notice that for this case the velocity field is completely determined from the mass conservation Equation (3.36). The numerical tests are performed with two different functional forms for $g(r)$: a step function with $g(r) = 1$ for $r \in (1.5, 2)$ and zero otherwise, and a continuous Gaussian function of the form

$$g(r) = e^{-\frac{(r-3.5)^2}{2}} \tag{3.39}$$

The discontinuous functional form of $g(r)$ results in discontinuities in the velocity and pressure fields constituting a difficult test for the overall approach. The smoother functional form provided by Equation (3.39) tests the solver on a situation more commonly found on actual computations where the void fraction usually is a continuous function in space.

Notice that in this test the void fraction is not transported with the velocity field as it would be in the simulation of a bubbly flow. In this regard this test case reproduces a situation similar to the flow across a porous media rather than an actual bubbly flow, resulting in a harder problem to solve given the discrete jumps of pressure and velocity across void fraction discontinuities. Notice also that the mass flux is continuous all across the domain. Equation (3.36) can be integrated analytically to obtain the velocity, and Equation (3.37) is then integrated numerically to obtain the pressure using a fine resolution with appropriate jump conditions at the locations with discontinuous in $g(r)$. The solution thus obtained is used as reference solution to gauge the performance of the numerical methods.

To avoid the generation of wiggles due to high order discretization schemes that might mask numerical issues with the pressure-velocity coupling under study, first order upwind in space and implicit Euler in time are used unless otherwise stated.

3.6.1.1 Instability at small time steps

Equations (3.36) and (3.37) are solved for the step function in $g(r)$ using $\Delta r = 0.05$ and $\Delta t = 9\times10^{-6}$ to discretize space and time, respectively. Successively larger time steps are used to illustrate convergence in time. The solution is advanced in time until a 99.9% void fraction is reached. Solutions for HS and CS are shown in Figure 3.3.

The fluid injected at $r = 1$ with velocity $u = 1$ slows down as r^{-1} due to mass conservation as the radius expands. The decrease in velocity continues up to $r = 1.5$ where the higher void fraction causes a discontinuous jump in velocity to conserve mass flux. A similar jump but decreasing velocity occurs at $r = 2$ as the void fraction goes back to zero. From this point forward the velocity keeps decreasing with r^{-1}. Pressure then adjusts to these changes in momentum according to Equation (3.37).

Solutions obtained with CS manifest spurious oscillations that originate at the discontinuities and propagate through the domain. The amplitude of these oscillations grows as smaller time steps are used.

The solutions obtained with HS represent a significant improvement upon the previously obtained solutions. Though not completely eliminated at the discontinuous void fraction interfaces, oscillations in velocity are greatly reduced and are confined to a small region of about two grid points in width. This can be observed in the insets for the velocity in Figure 3.3. More importantly, the solutions obtained with HS do converge for small time steps.

The solutions obtained with HS practically overlap on top of each other indicating a solution that is converged in time even for the larger time steps. Notice that HS underpredicts the total pressure jump when compared to the reference solution. This is an acceptable error considering the coarse grid used and the large jump in void fraction that forces a jump in velocity of three orders of magnitude. HS proved to be more stable and to provide more accurate solutions than CS and converges with time step with minimum spurious oscillations.

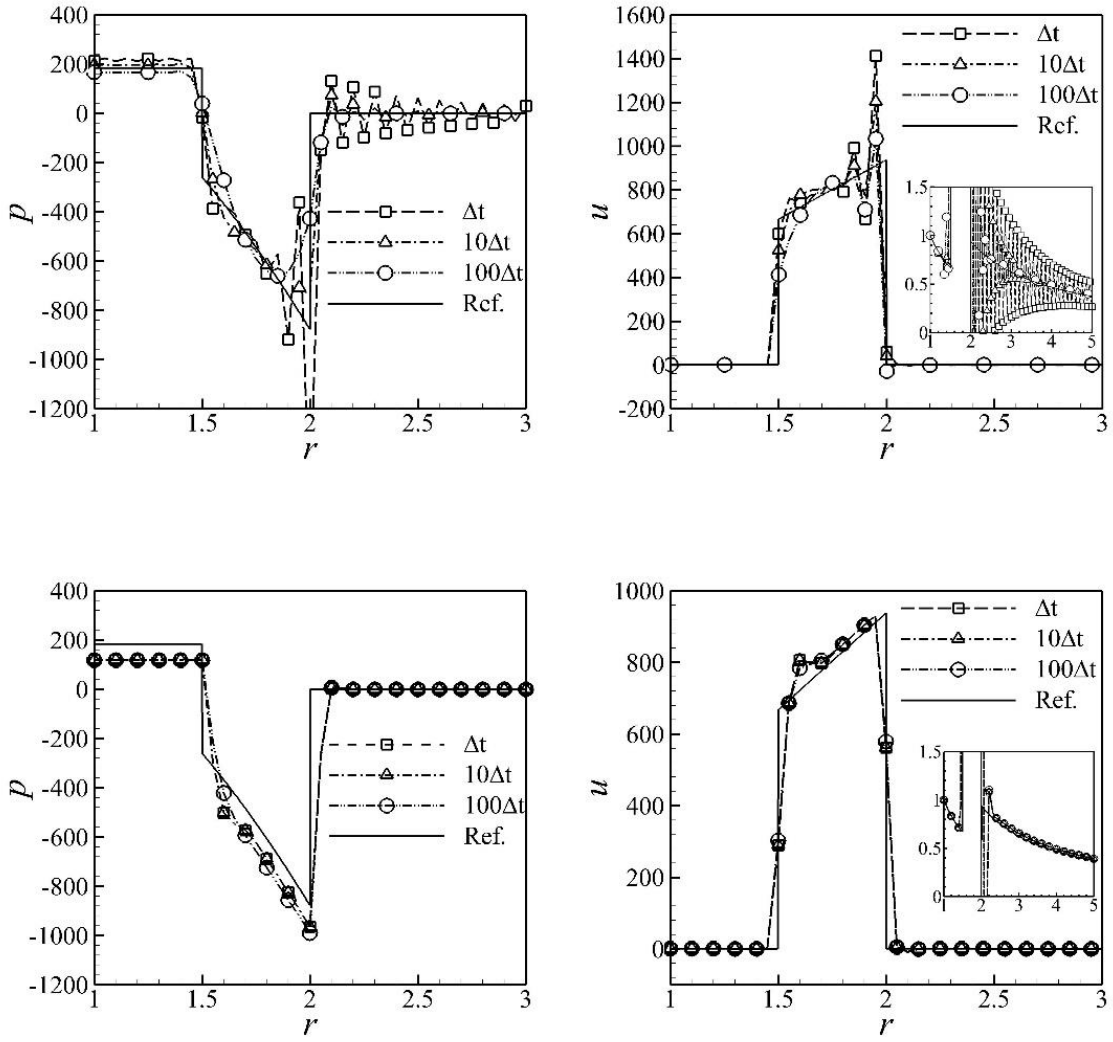

Figure 3.3: Pressure and velocity obtained with CS (top) and HS (bottom).

3.6.1.2 Grid study

A grid study is performed keeping the time step at $\Delta t = 9\times10^{-6}$ while successively refining the grid by a factor of two with the coarsest grid consisting of $N = 101$ points. The test is performed with both the step and Gaussian functions for $g(r)$ using HS. The solution is advanced in time until a 99.9% void fraction is reached.

Solutions obtained for the case with discontinuous void fraction are practically indistinguishable from each other except near the discontinuities. Particularly at $r = 1.5$ the overshoot in velocity decreases as the grid is refined and gets confined within a smaller

region. Notice that the same problem solved with N grid points using CS in Figure 3.4 exhibits large oscillations in pressure and velocity that pollute the entire domain.

The inlet pressure is underpredicted irrespectively of the grid refinement. This finite error in the pressure occurs because the numerical formulation presented assumes continuous pressure and velocity fields. For the bubbly flows of interest for this work, the void fraction, velocity and pressure are expected to be continuous and therefore a test with a continuous $g(r)$ is more representative. Results obtained for the Gaussian function in Equation (3.39) are presented in Figure 3.5. In this case a clear convergence to the reference solution is obtained as the grid is refined. The inset in Figure 3.5 shows that the inlet pressure converges towards the reference solution as the grid is refined, in contrast to the discontinuous case in Figure 3.4.

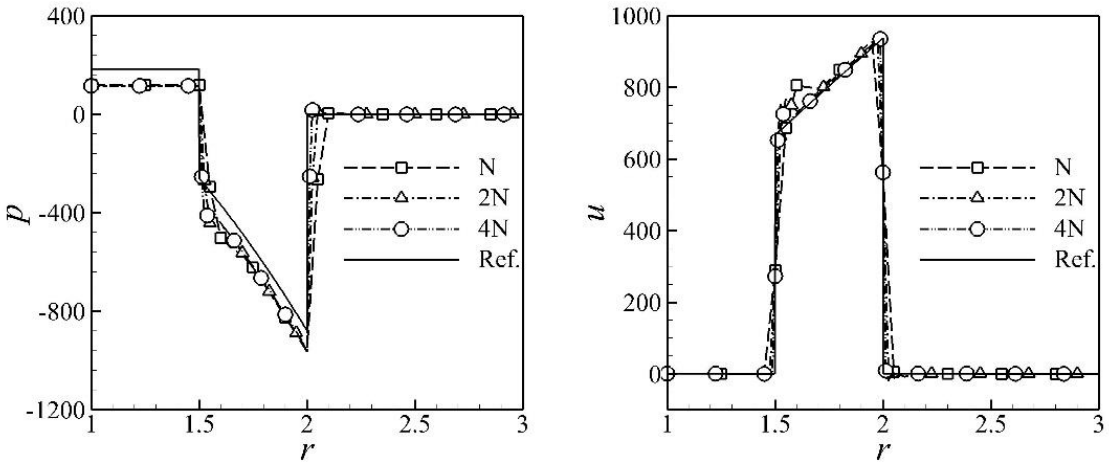

Figure 3.4: Grid study for pressure and velocity using HS. Discontinuous $g(r)$.

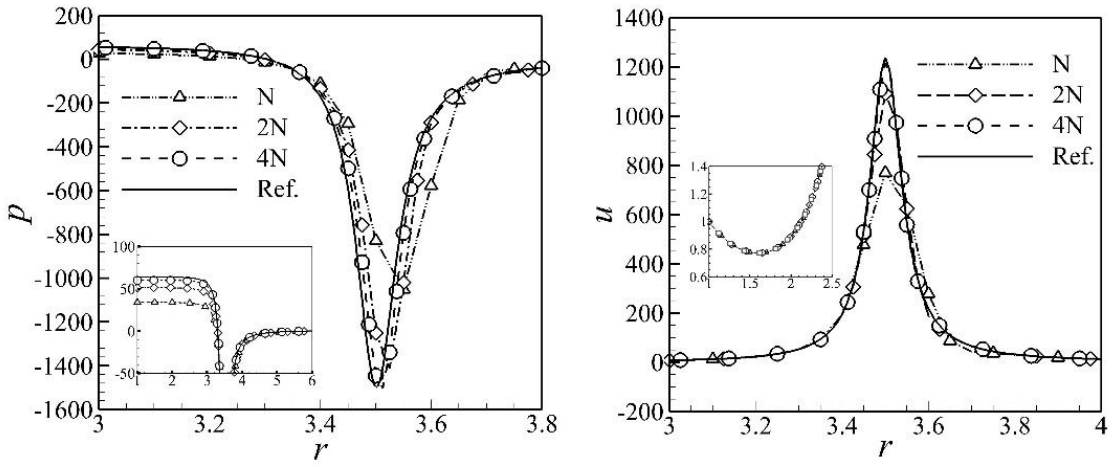

Figure 3.5: Grid study for pressure and velocity using HS. Gaussian $g(r)$.

3.6.2 Accumulation of bubbles against a wall

A serious problem in the simulation of bubbly flows around ships is the buildup of void fraction as bubbles rise towards the bottom of the ship's hull. The only mechanism preventing the accumulation of bubbles beyond a hundred percent void fraction is packing in Equation (2.3). The packing model is highly non-linear with void fraction, causing a tight interaction between pressure, velocity and void fraction, especially at high bubble concentration levels.

To test the overall coupling strategy under this particularly hard condition a 1D problem is solved in which gravity acts in the positive *x*-coordinate. Unless otherwise stated variables are non-dimensionalized using $U = 1$ m/s and $L = 1$ m. At $t = 0$ bubbles with a Sauter diameter $d_{32} = 2$ mm are located in $x \in (1.3, 1.8)$, with an initial void fraction α_{d0}, and rise with a fixed terminal velocity $V_T(d_{32}) = 10$ cm/s towards a wall located at $x = 2$. Bubbles rise due to buoyancy and accumulate as they encounter the wall. As the void fraction increases packing takes place until a steady state is reached. This test is also used to fix the functional form and strength of the packing function in Equation (2.5), under the constraint of not exceeding a hundred percent void fraction. The same packing model is then used throughout the rest of the paper.

Besides the grid study in Section 3.6.2.5, the domain $(1.0, 2.0)$ is discretized using 101 grid points and the time step is $\Delta t = 10^{-2}$. Second order upwind biased (Shu 1998) is used for convection. A second order TVD scheme with superbee limiter (Ismail et al. 2010) is used for bubble transport.

3.6.2.1 Comparison of CS against HS. Spurious oscillations.

To illustrate the generation of wiggles when using CS at moderate void fractions the problem is first solved with $\alpha_{d0} = 0.1$ and using a small time step of $\Delta t = 10^{-3}$. First order upwind is used to highlight that the generation of spurious oscillations is not introduced by the convection scheme. Figure 3.6 compares CS and HS at two time instances. After only ten time steps the void fraction and velocity still retain steep profiles. This causes spurious oscillations in the velocity that remain at later stages when the void fraction has been smoothed out due to numerical diffusion as shown for $t = 1$. These oscillations occur not only near void fraction gradients but also pollute the entire section of the domain where the velocity should essentially be zero. The HS in contrast, exhibits no oscillations even where void fraction undergoes sharp transitions.

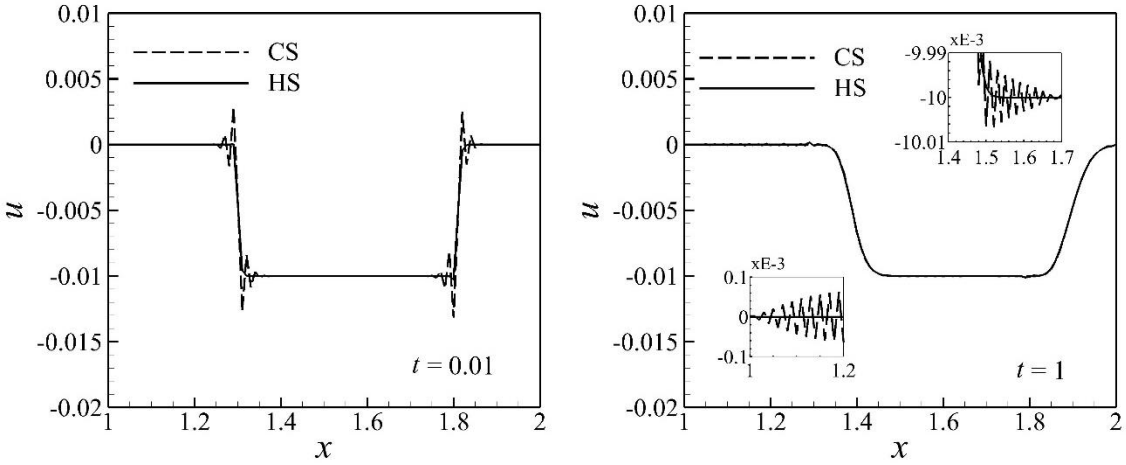

Figure 3.6: Comparison of CS and HS at low void fraction. Spurious oscillations generated using CS are completely removed when switching to HS.

3.6.2.2 Explicit coupling of void fraction

As discussed in Section 3.2, the coupling between pressure, velocity and void fraction may become unstable if the time derivative of the void fraction on the right hand side of the pressure Poisson Equation (3.10) is updated explicitly only after a new updated void fraction is available within the fixed-point iterative procedure. To demonstrate this issue the 1D accumulation of bubbles against a wall test case is solved using this explicit procedure with $\alpha_{d0} = 0.4$ and the results are shown in Figure 3.7. As bubbles approach the wall on the right and start accumulating the scheme eventually becomes unstable as the void fraction reaches high levels.

A new version of the mass conservation equation that solves this issue is presented in Section 3.2 and its robustness is demonstrated in the next sections.

3.6.2.3 Volumetric forces treatment

As discussed in Section 3.4, inconsistent treatment of volumetric forces in the momentum equation can result in the generation of spurious oscillations in the nodal velocities. For the modeling of bubbly flows these volumetric forces consist of the net buoyant term and packing. To illustrate the severity of this issue, the test case of 1D accumulation of bubbles is solved, this time using the coupling strategy presented in Section 3.2 using the Poisson Equation (3.24). The initial void fraction packet has maximum void fraction $\alpha_{d0} = 0.4$. Figure 3.8 shows the resulting velocities at time $t = 20$ for which a stable scheme would yield a solution close to steady state with zero velocity and bubbles packed against the wall. Face velocities are entirely determined by the discrete mass conservation Equation (2.2) and practically overlap for both methods in Figure 3.8(b). Notice that these velocities are very close to zero, as they should be in steady state. Nodal velocities shown in Figure 3.8(a), however, undergo large oscillations when simply the nodal evaluation of volumetric forces is used. The balanced force method introduced in Section 3.4 solves this issue.

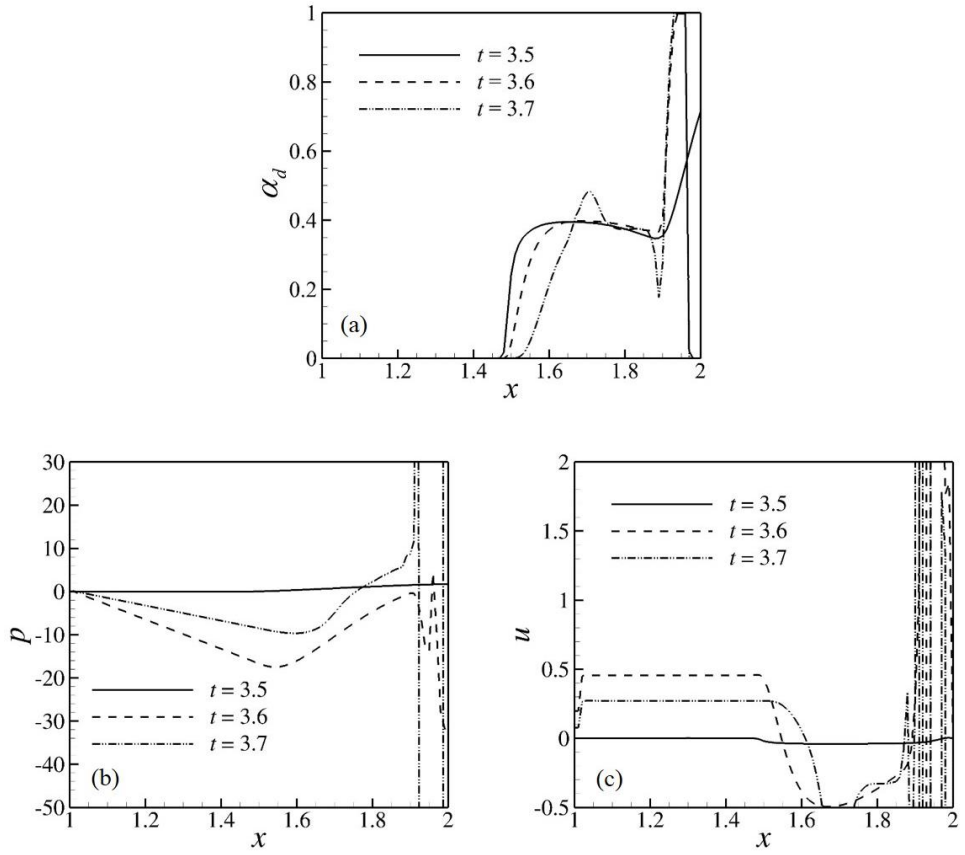

Figure 3.7: Explicit treatment of the void fraction time derivative. (a): void fraction distribution; (b) pressure distribution; (c) nodal velocity distribution.

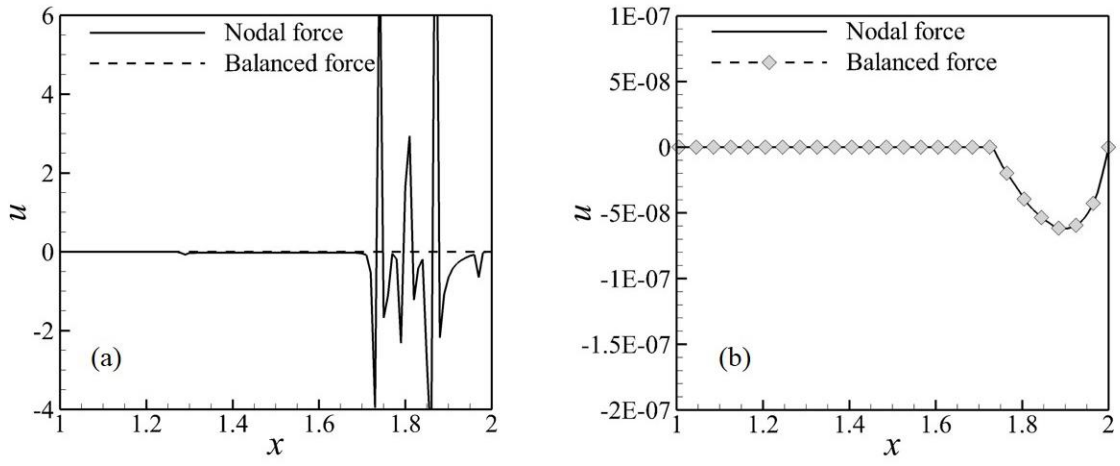

Figure 3.8: (a) nodal and (b) face velocities. Nodal evaluation of volumetric forces vs. balanced force method at $t = 20$.

3.6.2.4 Stable solution at high void fraction

This test case exemplifies the robustness of the numerical strategy for very large void fractions. For this test the initial void fraction is $\alpha_{d0} = 0.4$ and HS with balanced treatment of volumetric forces is used. A time sequence of the solution in Figure 3.9 shows how as bubbles rise towards the wall the liquid is displaced and forced to back out. As bubbles reach the wall they accumulate within a narrow region ($t = 4$) and as they continue to rise the void fraction increases reaching around 96% at the wall in steady state. Face and node velocities practically overlap on top of each other though face velocities satisfy mass conservation exactly while node velocities do not. At $t = 20$ the solution is practically steady. Notice that the pressure goes to zero in steady state, due to the fact that with the packing model presented in Section the fluid is free to flow and in equilibrium at zero velocity the pressure gradient vanishes.

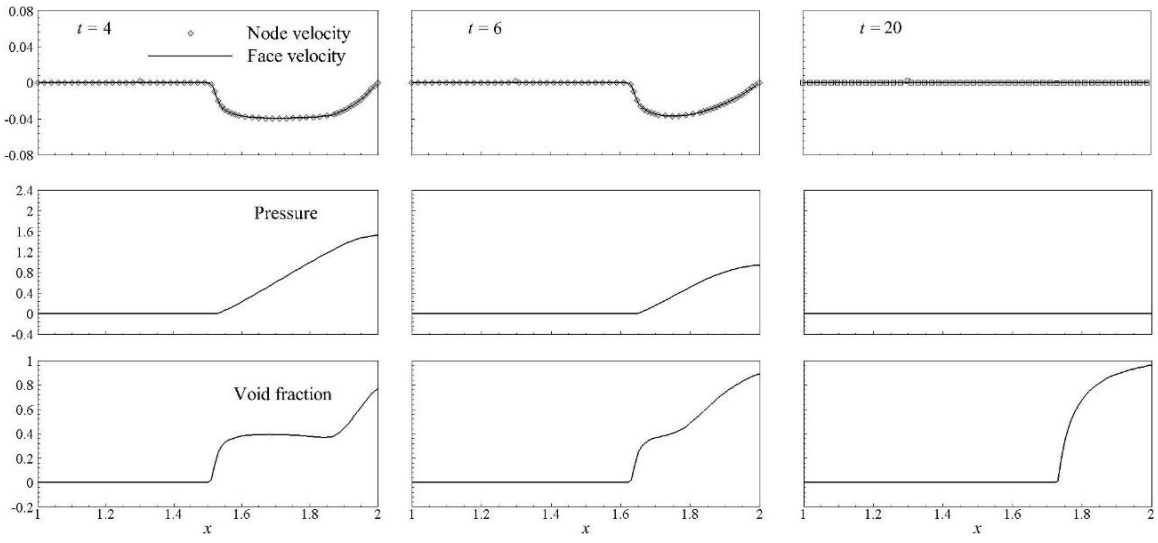

Figure 3.9: Time sequence of velocity, pressure and void fraction as bubbles travel from the left towards a wall on the right.

3.6.2.5 Convergence study

A grid study is performed on the full 1D test case of bubbles approaching a wall for which pressure, velocity and void fraction convergence rates are analyzed. The

configuration conditions are the same as the case above, except that the initial conditions here is a Gaussian distribution of the from

$$\alpha_{d0}(x) = 0.1\, e^{-\frac{(x-1.3)^2}{2\times 0.05^2}} \tag{3.40}$$

The grid spacing is progressively refined according to $\Delta x_i = \Delta x_0 / 1.5^{i-1},\ i = 1,2,3,4$ with the coarsest grid spacing set to $\Delta x_0 = 0.01$. The time step is kept fixed at $\Delta t = 2\times 10^{-3}$ for a Courant number $Co = 0.4$ for the finest grid, ensuring that the results are converged in time. In this case upwind biased ENO schemes (Shu 1998) are used for convection of liquid momentum and bubbles. A reference solution is computed with a 4th order ENO using a grid size $\Delta x = \Delta x_0 / 20$. The results are compared with the reference solution at $t = 3$ before accumulation at the wall takes place and large gradients could pollute the convergence analysis.

Figure 3.10 shows the error computed in l_1 norm for different convection schemes. The pressure solution reaches at most second order given that the Laplacian operator in Equation (3.24) is discretized using second order central differences. Since all variables are coupled by the model the upper bound in the pressure convergence rate can affect the convergence rate of the other variables. While the nodal velocity converges with second order at best, the face velocity can reach a faster rate. If a 4th order ENO is used for bubble transport, the void fraction reaches approximately 3rd order convergence rate due to the 3rd order interpolation of the face velocity used for the transport.

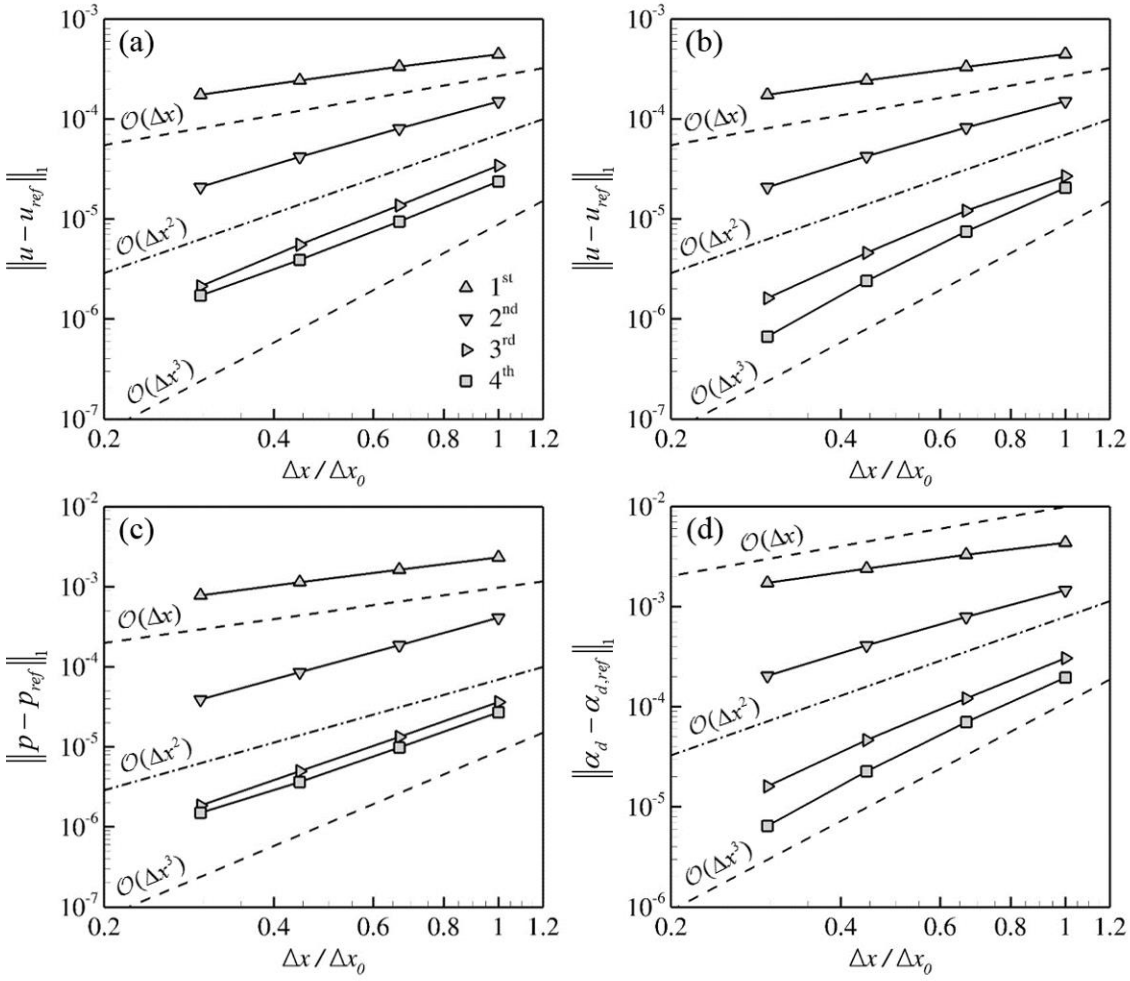

Figure 3.10: Convergence in l_1 norm using different convection schemes at $t=3.0$: (a) nodal velocity; (b) face velocity; (c) pressure; (d) void fraction.

3.6.3 2D tank case

A 2D case with high void fraction is designed to test the proposed scheme. Figure 3.11 shows a schematic of the configuration. The reference length and velocity are 1 m and 1 m/s, respectively, resulting in a Reynolds number of 1×10^6. The computational domain is $1(x)\times2(z)$ and the initial void fraction distribution is given by

$$\alpha_{d0}=\begin{cases}0.4 & 0.09\le x\le 0.91, 1.04\le z\le 1.85\\ 0 & \text{otherwise}\end{cases} \tag{3.41}$$

The computational domain is discretized using a uniform Cartesian grid with 101×201 nodes. Three bubbles sizes spanning a wide range of diameters are chosen to highlight the fundamentally distinct dynamic behavior due to their different terminal velocities, as summarized in Table 3.1, which shows terminal velocity V_T and discrete size distribution $D_g = N_g / N_{tot}$.

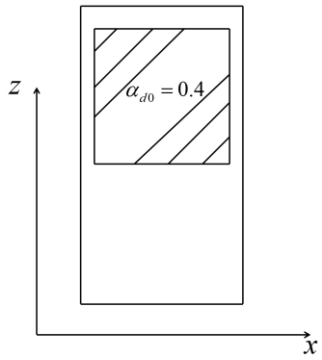

Figure 3.11: 2D tank initial flow configuration.

Table 3.1: Bubble size distribution for 2D tank simulation.

Radius (mm)	D_g	V_T (cm/s)
0.1	0.25	1.55
0.5	0.5	9.11
1	0.25	15.9

The two phase blended k-ε / k-ω SST turbulence model is used to model turbulence (Moraga et al. 2008). All the boundaries have no-slip wall boundary conditions. The simulation is run for 50 non-dimensional time units with a time step $\Delta t = 5\times10^{-3}$. Second order in space and time are used for discretization. The total void fraction transport and multigroup number density transport are solved using a TVD scheme with superbee limiter (Ismail et al. 2010) to avoid undershoots that can result in unphysical negative void fraction. A second-order upwind linear scheme is used for the liquid momentum.

Given that number densities are updated at the end of the time step iteration, see Figure 3.1, these are not available to update the packing force in the momentum equation. As discussed in Section 3.2.1, using the previous time step information to compute this term may lead to unstable coupling. A semi-implicit approach was proposed which uses the latest void fraction information while only leaving the size distribution, not its magnitude nor its gradient, explicitly computed. To test these ideas, the 2D tank problem is solved using both approaches.

Figure 3.12 shows void fraction contours comparing solutions obtained using both approaches at $t = 50$ when the solution is close to a steady state. Notice that the contours are colored in a logarithmic scale to visualize the small void fraction contributions of the smallest bubbles. While large bubbles quickly rise up towards the top where they accumulate due to packing, small bubbles behave essentially as fluid tracers leaving characteristic traces caused by the fluid motions, see Figure 3.12. Besides small secondary motions at the bottom of the tank, at $t = 50$ the fluid is practically steady. Nonetheless, oscillations develop at the sharp interface of packed bubbles at the top of the tank when the packing forces are updated explicitly as observed by the wavy pattern in Figure 3.12. The proposed semi-implicit scheme however yields a stable solution.

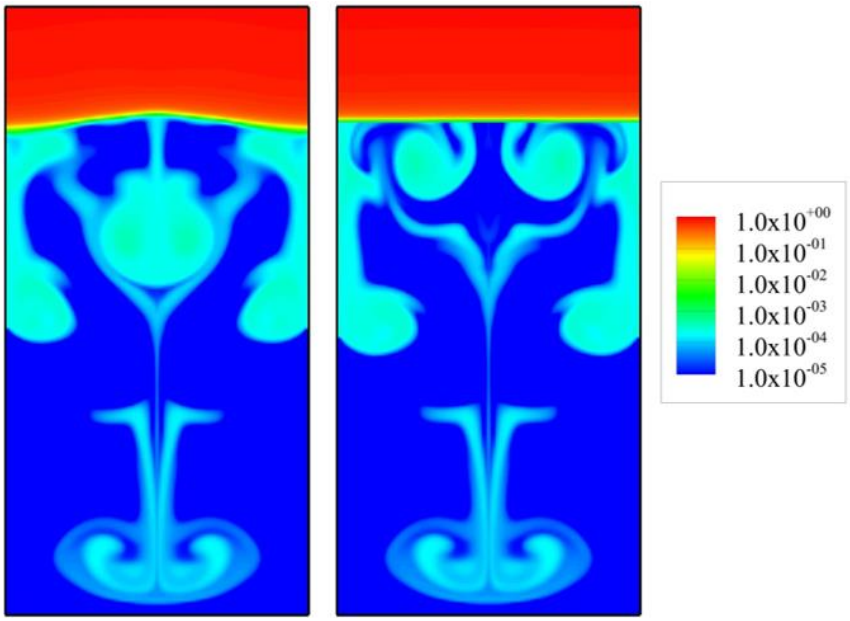

Figure 3.12: Void fraction distribution at $t = 50$. Explicit (Left) and semi-implicit (Right) approaches for the computation of the packing term.

Figure 3.13 shows the time history of the total liquid kinetic energy in the tank. The oscillations for the explicit method grow in time increasing the energy of the system eventually causing divergence, while the proposed semi-implicit method shows a continuous decrease in energy as expected.

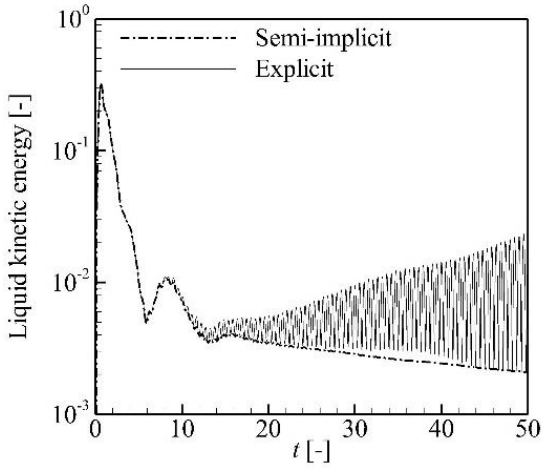

Figure 3.13: Total liquid energy varies with time.

Figure 3.14 (a) shows a time evolution of the total void fraction. At $t = 0.3$ bubbles rise and expand in width mainly due to contact forces modeled by packing. Two lobes appear at $t = 0.6$ due to the presence of counter rotating vortices formed as the rising bubbles displace liquid. Bubbles accumulate against the wall as they reach the top of the tank where packing balances with buoyancy in steady state. Large bubbles initially dragged down by the primary pair of vortices eventually rise back up and join the foamy region near the wall. Given their small terminal velocity, small bubbles are dragged by the liquid and highlight weaker secondary vortices that reach the bottom of the tank. This behavior is better appreciated in Figure 3.15 which shows contours of group void fraction α_g for each bubble size. While 0.5 mm and 1.0 mm bubbles quickly concentrate at the top, 0.1 mm bubbles follow liquid currents at the bottom of the tank.

A time sequence of pressure contours is shown in Figure 3.14(b). The proposed scheme yields a very smooth and stable pressure field that, as expected, approaches zero at $t = 50$.

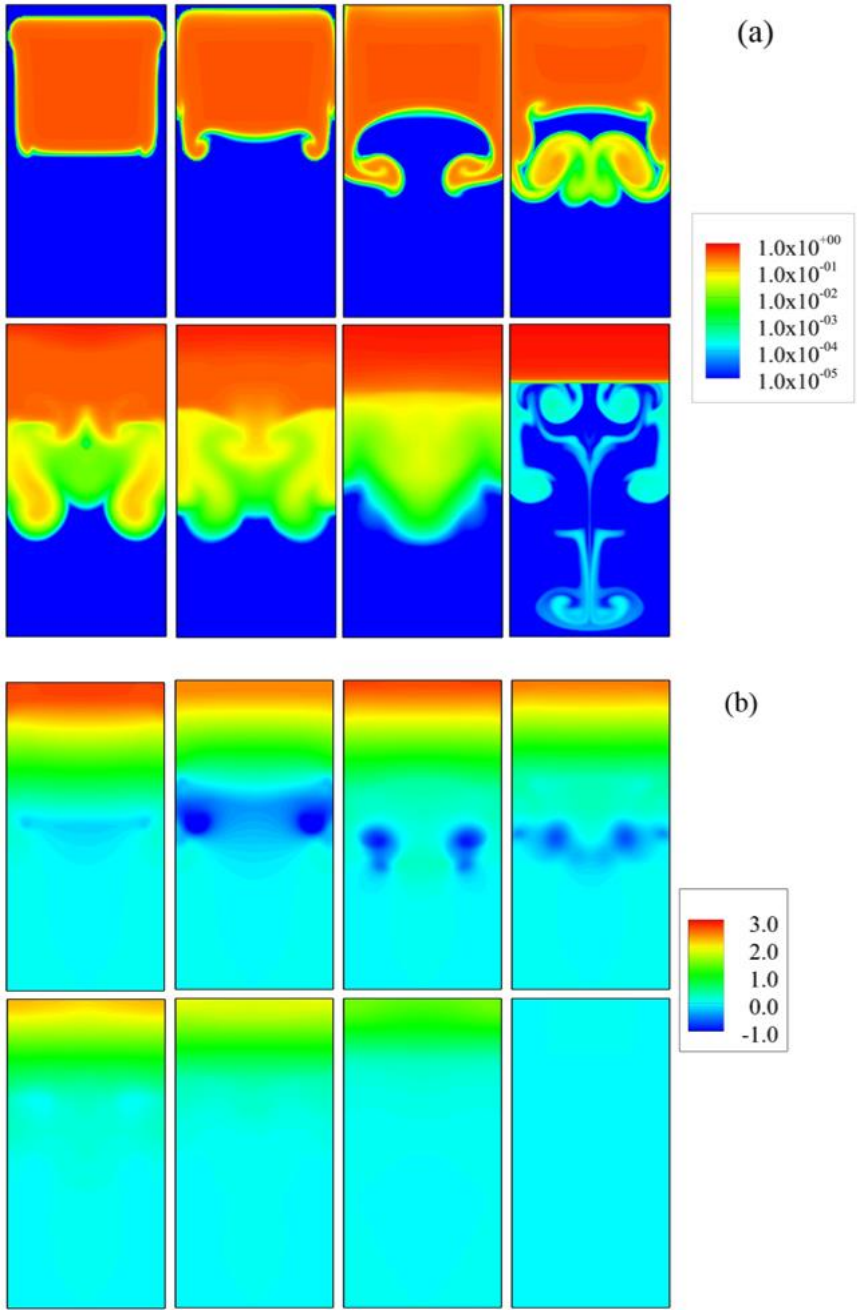

Figure 3.14: Void fraction (a) and pressure distribution (b) for different time steps. Top: $t = 0.3, 0.6, 1, 1.5$; Bottom: $t = 2.5, 3.5, 5.5, 40$

The conservation of bubble mass is assessed by monitoring the defect of mass $\varepsilon_m = (m(t) - m_0)/m_0 \times 100\%$ with $m(t)$ the integral of void fraction over the entire domain and m_0 the initial mass. This is shown in Figure 3.16 where good mass conservation is observed with a maximum defect of 0.25% over the large time span of the simulation.

While the proposed scheme should preserve mass exactly, small convergence errors lead to mass defects, most of which occur during the process of settlement of the foam on top of the tank.

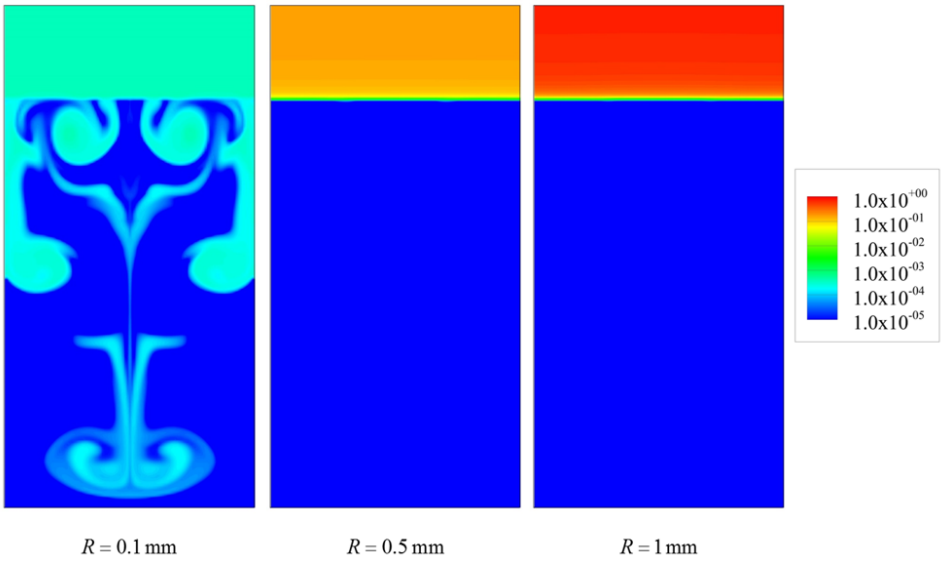

Figure 3.15: Void fraction distribution for each group at $t = 50$.

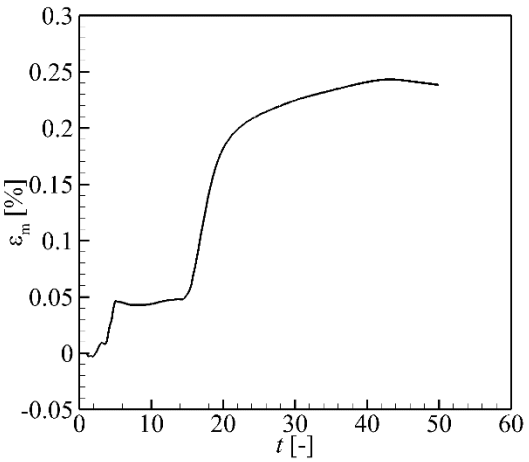

Figure 3.16: Bubble total mass variation varies with time.

CHAPTER 4 TURBULENT ENTRAINMENT MODEL

Air entrainment in turbulent flows is a very intricate phenomenon given the difficult treatment of polydisperse bubbly flows, the inherent complexity of turbulence and the very convoluted interfacial transport taking place at the free surface. Even when extensive research has been performed separately in each of these areas, their interaction is still a little explored area.

The model developed in this work attempts to model the physical phenomena that cause and influence the formation and transport to depth of bubbles. This approach is greatly differentiates from previous work in that the model is built from mechanistic processes. This model starts considering the effect that one single vortex has on the deformation of the free surface. Using models of turbulence successfully used before in theories of bubble breakup, the effect of several turbulent length scales is taken into account. Considering these mechanisms, the model predicts no entrainment for large, deep vortices since they only generate waves with long wave lengths but not steep enough to cause the breakage of the free surface. In addition, very small vortices are not able to entrain air either due to the strong stabilizing effect of surface tension forces on small scales. As a result, the model is able to predict entrainment for a range of turbulent scales that are energetic enough.

Figure 4.1 shows vortex interacting with free surface. These vortices can be described as different length scale eddies of turbulence. They can deform and break the surface. Bubbles can be entrained when the energy of eddies is suitable. Also the bubbles have to fight against buoyancy as dragging down by liquid. In this case large bubbles rise and escape through the free surface faster than smaller bubbles and therefore it is more likely to find small bubbles rather than large bubbles at larger depths. In addition bubbles are still subject to breakup and coalescence as they are pulled deeper into the bulk of the fluid.

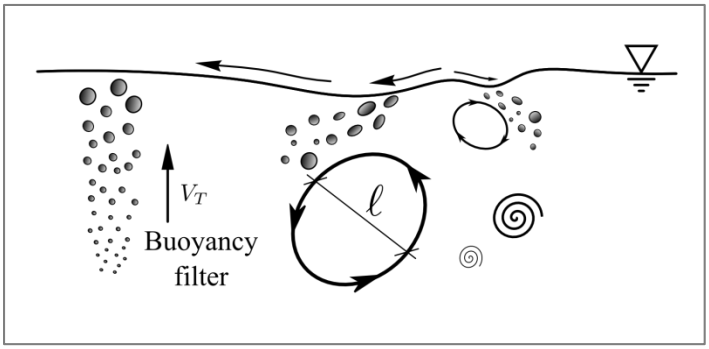

Figure 4.1: Schematic of air entrainment by turbulence.

The assumption at this point is that the shape of the vortex can be neglected, giving priority to the energy content of that vortex scale. In addition, smaller vortices may induce deformations on top of the deformations caused by larger vortices. In this regard, a "superposition" hypothesis is used. This hypothesis has previously been used with good success in the development of breakup models.

This chapter is organized as follows. In Section 4.1 a general framework is presented which would allow, under different levels of approximation, to obtain a series of entrainment models. This framework attempts to describe air entrainment by turbulence as a cascade of separate processes that can be treated individually. It also tries to obtain a general expression for the air entrainment rate which is composed of multiplicative factors independent of each other. Different approximations and modeling strategies for each of these terms would then allow to attaining a simple but mechanistic model. Sections 4.2 to 4.7 describe modeling strategies for each of the terms appearing in the general framework in Section 4.1. Finally in Section 4.8 further simplifications are presented that allow to achieve an air entrainment model which only requires the computation of a one-dimensional integral. To complete the picture, Section 4.9 presents how the momentum and turbulence model equations need to be modified in order to satisfy the basic energy and momentum conservation laws. Section 4.10 introduces a free surface turbulence model which considering turbulence generation due to unresolved roughness on free surface.

Section 4.11 discusses limitations in the model with recommendations for future work. A preliminary entrainment model due to impact between the boat and the rough free surface is presented in Section 4.12.

4.1 A general framework

The air entrainment framework described in this section is composed of several factors that attempt to describe bubble motions for formation at the free surface, breakup and coalescence when descending and filtering due to buoyancy. These sequences are summarized in Table 4.1.

Consider the schematic of Figure 4.2 where a single vortex of size ℓ located at a depth z' entrains air across the free surface at a rate $Q_\ell(\ell, z')$ in m^3/s. From now on the set of variables characterizing a given vortex configuration (size and distance from the free surface) is denoted by $\mathcal{V} = \{\ell, z'\}$. $n_\ell \, d\ell$ is the number of vortices per unit volume with size within $d\ell$ of ℓ. The contribution to the total amount of air entrained by vortices located at a depth z' in a differential volume $dV' = A dz'$ is given by Equation (4.1) in Table 4.1 where A is an arbitrary transversal area. The number of bubbles entrained can be obtained through dividing this number by the mean bubble volume entrained at the free surface, namely $\bar{v}_0$.

Bubbles entrained by the interaction of a vortex and the free surface have a size distribution $p_0(D|\mathcal{V})$, characteristic of the formation process. This size distribution may be changed later due to two basic processes: 1) breakup and coalescence of the entrained bubbles and 2) filtering due to buoyancy. The number of entrained bubbles with size within dD_0 of D_0 is proportional to $p_0(D_0|\mathcal{V})dD_0$. This is reflected by Equation (4.2) in Table 4.1.

After these bubbles travel to a depth z into the fluid the size distribution can be changed as $p_h(D|D_0, z)$ because of breakup and coalesce. $p_h(D|D_0, z)$ represents the size distribution for bubbles entrained with size D_0 and then travel a distance z into the

water. The proportion of the above bubbles having size within dD of D at depth z is $p_h(D \mid D_0, z)dD$, Equation (4.3) in Table 4.1.

The last factor considered contains information about the filtering in size due to buoyancy. $p_z(z \mid D)\,dz$, the probability of a bubble with size D being pushed down to within dz of a depth z, should account for this effect, Equation (4.4) in Table 4.1.

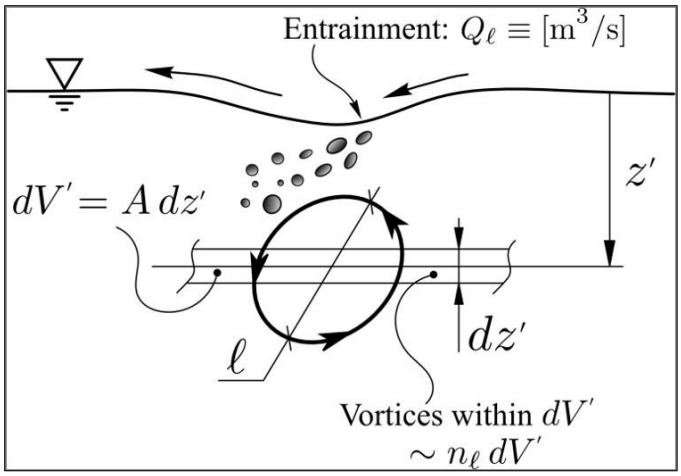

Figure 4.2: Single vortex contribution to air entrainment.

Table 4.1: Sequential events during the lifetime of a bubble entrained at the free surface.

NO.	Description	Equation
(4.1)	Total air entrainment by vortices located in a volume dV' at depth z'	$Q_\ell(\mathcal{V})\, n_\ell(\ell)\, d\ell\, dV'$
(4.2)	Bubbles within dD_0 of size D_0	$Q_\ell(\mathcal{V})\, n_\ell(\ell)\, d\ell\, dV'\, p_0(D_0 \mid \mathcal{V})\, dD_0/\overline{v}_0$
(4.3)	The bubbles travel into a depth z and change their size distribution due to breakup and coalescence into $p_h(D \mid D_0, z)$	$Q_\ell(\mathcal{V})\, n_\ell(\ell)\, d\ell\, dV'\, p_0(D_0 \mid \mathcal{V})\, p_h(D \mid D_0, z)\, dD/\overline{v}_0$
(4.4)	Size distribution also changes due to the probability that a bubble is transported down to a depth z	$Q_\ell(\mathcal{V})\, n_\ell(\ell)\, d\ell\, dV'\, p_0(D_0 \mid \mathcal{V})\, p_h(D \mid D_0, z)\, dD\, p_z(z \mid D)\, dz/\overline{v}_0$

The total source of entrainment is obtained by integrating in D_0, the size of the bubbles originally formed at the free surface. Then all vortex sizes are considered by integrating over ℓ. Finally the contribution to the whole turbulent field (homogenous and isotropic is assumed in the turbulent field) underneath the free surface is taken into account by integrating in z'. The entrainment rate can be written as

$$Q(D,z) = \underset{dV}{dz\, A\, dD}\, \frac{1}{\overline{v}_0}\, p_z(z \mid D) \int_0^\infty dz' \int_0^{2z'} d\ell\, Q_\ell(\mathcal{V})\, n_\ell(\ell) \int_0^\ell dD_0\, p_0(D_0 \mid \mathcal{V})\, p_h(D \mid D_0, z) \quad (4.5)$$

where the area A in dV' is taken outside of the integral together with dz to form $dV = A\,dz$, the differential volume to where bubbles are dragged down. The integral ranges are decided based on following assumptions: Vortices of size ℓ can only entrain bubbles smaller than the vortex size, as a result, the upper limit of the innermost integration cannot exceed ℓ. It is also assumed that only vortices with a diameter ℓ smaller than $2z'$ can

entrain air and thus the integration in ℓ only goes to $2z'$. This assumption essentially is a geometrical limit that a vortex must be fully located below the free surface. In addition, it is assumed that the probability of reaching a given depth is not a function of the vortex size but rather a function of the overall flow condition. Therefore $p_z(z|D)dz$ does not depend on the vortex $\mathcal{V}$ and can be factored out.

It has to be noticed that the two depth coordinates z' and z have a completely different meaning. The contribution to the entrainment at a depth z is considered due to vortices located at a given depth z'. Thus bubbles can be entrained at depths that can be different from the location of the vortex responsible of entraining them.

The entrainment source for a bubble size D at depth z is obtained as

$$S(D,z)=\frac{Q(D,z)}{dV\,dD}=\frac{1}{\bar{v}_0}p_z(z|D)\int_0^{\infty}dz'\int_0^{2z'}d\ell\,Q_\ell(\mathcal{V})\,n_\ell(\ell)\int_0^{\ell}dD_0\,p_0(D_0|\mathcal{V})\,p_h(D|D_0,z) \quad (4.6)$$

As shown in Equation (4.6), the following terms require modeling to close this model:

1. $Q_\ell(\mathcal{V})$ [m^3/s], the rate of air entrainment by a single vortex $\mathcal{V}$.
2. $n_\ell(\ell)$ [1/m^3 m], the vortex number density distribution.
3. $p_0(D_0|\mathcal{V})$ [1/m], bubble size distribution of bubbles entrained by a vortex $\mathcal{V}$.
4. $p_h(D|D_0,z)$ [1/m], bubble size distribution of bubbles entrained with a size D_0 due to breakup and coalescence as they traveled to a depth z.
5. $p_z(z|D)$ [1/m], the probability of finding a bubble of size D at a depth z in monodisperse flow.

4.2 Turbulence scales

Pope (2000) gives an analytical model of a spectrum for homogeneous turbulence,

$$E(\kappa) = C\,\varepsilon_t^{2/3}\kappa^{-5/3} f_L^{5/3+p_0}(\kappa L)\, f_\eta(\kappa\eta)$$
$$f_L(\kappa L) = \kappa L \Big/ \left[(\kappa L)^2 + c_L\right]^{1/2} \tag{4.7}$$
$$f_\eta(\kappa\eta) = e^{-\beta\left\{\left[(\kappa\eta)^4 + c_\eta^4\right]^{1/4} - c_\eta\right\}}$$

where $\kappa = 2\pi/\ell$ is the wavenumber, $L = k_t^{3/2}/\varepsilon_t$ and $\eta = \left(\nu^3/\varepsilon_t\right)^{1/4}$ is the Kolmogorov scale. The model coefficients, obtained from experimental data, are $C = 1.5$, $p_0 = 2$, $c_L = 6.78$, $\beta = 5.2$ and $c_\eta = 0.4$. The corresponding turbulent kinetic energy and dissipation are

$$k_t = \int_0^\infty E(\kappa)d\kappa$$
$$\varepsilon_t = \int_0^\infty 2\nu\kappa^2 E(\kappa)d\kappa \tag{4.8}$$

The transition length from the energy containing range to inertial range L_{EI} is defined as $f_L^{5/3+p_0}(L_{EI}) = 0.95$ and the transition length from the inertial range to the dissipation range is defined as $f_\eta(L_{ID}) = 0.95$. This results in the limits

$$L_{EI} \approx 0.945 L_{11} \approx L_{11}$$
$$L_{ID} \approx 28\eta \tag{4.9}$$

In the inertial subrange the r.m.s. velocity of eddies with size ℓ scales as $u_\ell = \beta^{1/2}(\varepsilon_t \ell)^{1/3}$ with $\beta \approx 2$, which is verified by the experiments performed by Kuboi et al. (1972). To extend this relation into the energy containing range it is assumed that $u_\ell \propto \kappa$ and a smooth transition with a functional form similar to the one for f_L in Equation (4.7) is proposed. Therefore, the r.m.s. velocity of eddies with size ℓ is estimated as

$$u_\ell = \sqrt{2}(2\pi)^{1/3}\left(\frac{\varepsilon_t}{\kappa}\right)^{1/3} f_L^{1/3+1} = \sqrt{3}(2\pi)^{1/3}\frac{u_0}{(\kappa L)^{1/3}} f_L^{4/3} \tag{4.10}$$

According to this model $u_\ell \approx 1.28 u_0$ at $\ell = L_{11}$ and the maximum r.m.s. velocity is $u_\ell = 1.6 u_0$ for $\ell = 3.25 L_{11}$. $u_0 = \left(2k_t/3\right)^{1/2}$ is the r.m.s of the velocity fluctuation for isotropic turbulence.

Typical turbulent scales at the stern of Athena R/V are summarized in Table 4.2. In addition, it shows the Hinze diameter D_H estimated according to (Hinze 1955)

$$D_H = 0.725\left(\frac{\sigma}{\rho}\right)^{3/5}\frac{1}{\varepsilon_t^{2/5}} \tag{4.11}$$

Bubbles with a diameter smaller than D_H are strongly stabilized by surface tension difficult to break up. However, bubbles smaller than D_H can be formed by the breakage of bubbles larger than D_H and by highly energetic impact processes.

Table 4.2: Mean flow characteristics at the stern of the Athena R/V.

Scale	**Symbol [unit]**	**Value**
Turbulent intensity	I_t [-]	0.2
Integral length scale	L_{11} [m]	0.3
r.m.s velocity.	u_0 [m/s]	1.08
Turbulent kinetic energy	k_t [m^2/s^2]	1.75
Turbulent dissipation	ε_t [m^2/s^3]	3.32
Turbulent viscosity	ν_t [m^2/s]	0.0831
Kolmogorov scale	η [m]	23.43 x 10^{-6}
Hinze's diameter	D_H [m]	1.47 x 10^{-3}

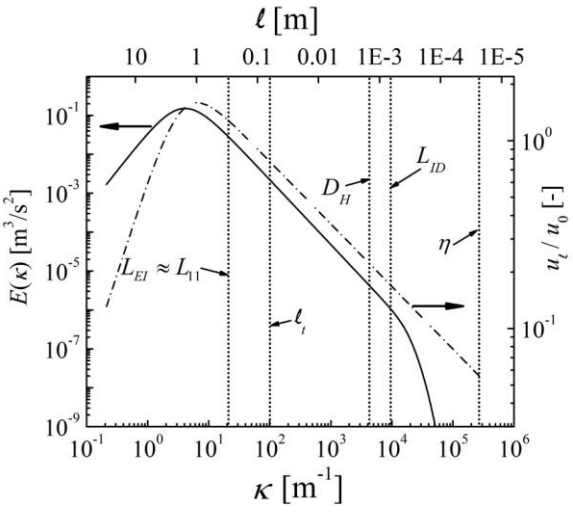

Figure 4.3: The scales of turbulence at the stern of Athena.

These scales are shown in Figure 4.3 together with the turbulent spectrum according to the model in Equation (4.7) and the r.m.s. velocity in Equation (4.10). Integral length scale in blended $k-\varepsilon/k-\omega$ SST model (Menter 1993) ℓ_t is also shown to be smaller than L_{11}. Different axes are used to show $E(\kappa)$ and u_ℓ in the same plot.

4.3 Vortex density in turbulent flow

The density of vortices n_ℓ in Equation (4.6) is modeled by Luo and Svendsen (1996) through describing vortices as spheres of diameter ℓ with mean kinetic energy $e_\ell = \pi\rho_c \ell^3 u_\ell^2/12$. According to this idea the energy spectrum is related to the vortex density by

$$\left(1-\alpha_d\right)\rho_c E\left(\kappa\right) = n_\ell\, e_\ell \tag{4.12}$$

where the factor $(1-\alpha_d)$ is the fraction of liquid. Considering Equation (4.7) and Equation (4.12) the vortex density is found as

$$n_\ell(\ell) = 0.8413\frac{(1-\alpha_d)}{\ell^4} f_L^{\,p_0-1} \tag{4.13}$$

Therefore, the vortex density is proportional to ℓ^{-4} for $\ell << L$ and, with $p_0 = 2$, to ℓ^{-5} for $\ell >> L$.

4.4 Single vortex air entrainment

Air entrainment by a single vortex is modeled considering a simplified problem consisting of a vortex of size ℓ at a distance z' from the free surface. This vortex induces deformations on the free surface that may eventually lead to air entrainment.

The vortex is modeled using the potential flow solution to a line vortex with the condition that $u(\ell/2) = u_\ell$. To obtain the pressure distribution and a first approximation to the induced deformation on the free surface, the mean free surface is assumed to be located at $z = 0$ and thus a vortex image is located at $z = -z'$. The stream function for this simplified problem is

$$\psi = \frac{u_\ell \ell}{2}\left[\ln\left(\sqrt{x^2+(z'+z)^2}\right)-\ln\left(\sqrt{x^2+(z'-z)^2}\right)\right] \tag{4.14}$$

Pressure is computed using the Bernoulli equation as

$$p(x,z) = p_a + \rho g z - \frac{1}{2}\rho u^2(x,z) \tag{4.15}$$

where p_a is the atmospheric pressure. Using the dynamic pressure induced at $z=0$ the free surface elevation $h(x)$ is then approximated through $p(x,h(x)) = p_a$, then

$$h(x) = \frac{u^2(x,0)}{2g} = \frac{(u_\ell \ell)^2}{2g}\frac{z'^2}{\left(z'^2+x^2\right)^2} \tag{4.16}$$

In Duncan (2001) it is mentioned that waves with a slope below approximately 18° are stable, while steeper slopes may result in spilling breaker. Therefore, this model assumes that air entrainment occurs when the slope of the free surface deformation reaches a critical angle of 18° or a slope of $s_{cr} = 0.325$. From Equation (4.16) the free surface slope s is obtained

$$\begin{aligned} \tilde{s} &= \frac{\tilde{x}}{(1+\tilde{x}^2)^3} \\ \tilde{x} &= x / z' \\ \tilde{s} &= \frac{s}{2\,\mathrm{Fr}_\ell^2}\left(\frac{z'}{\ell}\right)^3 \end{aligned} \tag{4.17}$$

where the vortex Froude number is defined as $\mathrm{Fr}_\ell = u_\ell / \sqrt{g\ell}$.

It is assumed the vortices form a ring of vortex tube under the free surface. This vortex tube induces an entrainment ring of diameter D_s. In analogy to the analysis carried out by Carrica et al. (2012) for plunging jets, the air entrainment rate for a single vortex is modeled as the flux of air through this ring of diameter D_s and a thickness due to surface roughness δ. Air is entrained through this ring with the surface velocity u_s. Therefore the flux of air through this ring is $\pi D_s \delta u_s$. However, given that the single vortex configuration is more complex than that of a plunging jet, the air entrainment is modeled to be proportional to this flux. Therefore

$$Q_\ell(\mathcal{V}) = S_{\ell 0}\, D_s\, \delta u_s \tag{4.18}$$

with $S_{\ell 0}$ hopefully a universal enough constant for a wide range of air entrainment problems. Using the potential vortex solution the velocity at the free surface is estimated as

$$u_s(\ell, z) = u_\ell \frac{\ell}{z} \tag{4.19}$$

According to Hunt (1984) the free surface roughness can be modeled from a balance between the potential energy of the surface deformation and the kinetic energy of the vortex leading to $\delta \propto u_s^2 / g$.

The ring vortex diameter D_s is found at the position where the slope according to Equation (4.17) is critical. Thus

$$\frac{D_s(z/\ell, Fr_\ell)}{\ell} = 2\frac{z}{\ell}\tilde{x}\left(\frac{s_{\mathrm{cr}}}{2\,\mathrm{Fr}_\ell^2}\left(\frac{z}{\ell}\right)^3\right) \tag{4.20}$$

where z' is replaced by z considering the variant position when the vortex moves to the free surface from a place far away. As the vortex approaches the free surface the deformation predicted according to Equation (4.16) increases. It can result in very large, unphysical deformations, for strong enough vortices close to the free surface. This is due to the model simplification (such as potential flow, no surface tension). Here a remedy is proposed to avoid unphysical result. It is assumed that when the free surface slope reaches a maximum deflection s_{M} the deformations are so strong that the simple model used to estimate the slope breaks down. The free surface shape freezes at the one with a maximum slope s_{M} for this situation. Lacking experimental or numerical results guiding a better decision this maximum slope is taken to be 45° or $s_{\mathrm{M}} = 1.0$. The minimum depth at which a vortex induces this maximum slope is denoted by z_{m}. As a consequence, the free surface does not vary for $z < z_{\mathrm{m}}$ reaching its maximum size $D_{s\mathrm{M}}$.

When the vortex is not strong enough to induce the minimum slope s_{cr} for air entrainment to occur, Equation (4.20) does not have a solution and therefore $D_s = 0$ is used

for convenience. The onset depth at which the slope at the free surface reaches s_{cr} is denoted as z_e. Vortices farther than z_e from the free surface are not able to induce deformation slopes larger than s_{cr} and therefore do not entrain air.

The onset depth z_e of entrainment is found as the point at which the maximum of $\tilde{s}$ corresponds to a slope s_{cr}. Correspondingly, the minimum depth for maximum deformation is found as the point at which the maximum of $\tilde{s}$ corresponds to a slope s_{M}. This results in

$$\begin{aligned} z_e &= 1.168\,\ell\,\mathrm{Fr}_\ell^{2/3} \\ z_{\mathrm{m}} &= 0.803\,\ell\,\mathrm{Fr}_\ell^{2/3} \end{aligned} \tag{4.21}$$

and for the maximum ring diameter

$$D_{\mathrm{sM}} = 1.914\,\ell\,\mathrm{Fr}_\ell^{2/3} \tag{4.22}$$

These results suggest that the length scale $\ell\,\mathrm{Fr}_\ell^{2/3}$ can be used to make all the vortex ring diameters as a function of depth to collapse into a single curve for all vortex strengths (given by Fr_ℓ). Finally, if the onset depth is used as a reference length the entrainment diameter is

$$\frac{D_s}{z_e} = \tilde{D}_s(z/z_e) = \begin{cases} 0 & z/z_e > 1 \\ 2\dfrac{z}{z_e}\tilde{x}\left(0.824\,s_{\mathrm{cr}}\left(\dfrac{z}{z_e}\right)^3\right) & 0.688 < z/z_e < 1 \\ 1.615 & z/z_e < 0.688 \end{cases} \tag{4.23}$$

This profile is shown in Figure 4.4 together with the onset of entrainment depth. The onset of entrainment depth is shown in Figure 4.5 as a function of Fr_ℓ as well as a function of vortex size ℓ for the parameters in Table 4.2 .

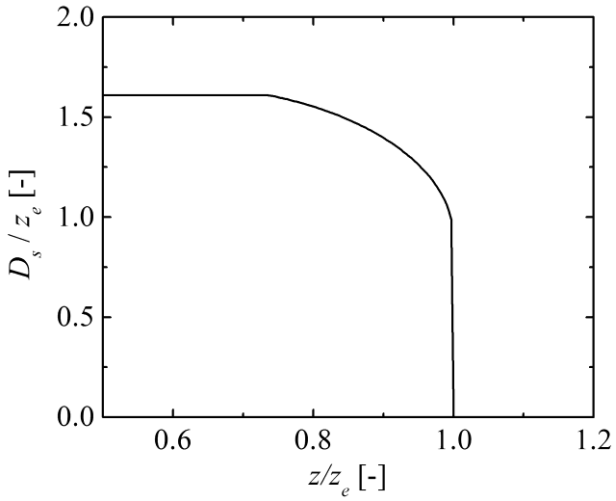

Figure 4.4: Entrainment ring diameter as a function of vortex size

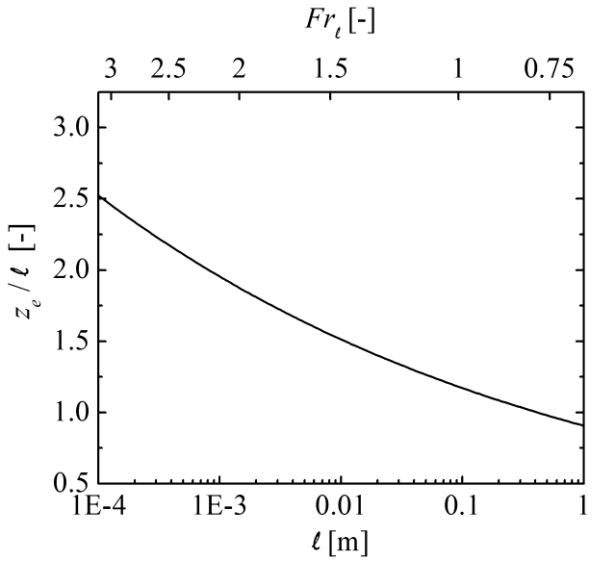

Figure 4.5: Onset of entrainment depth as a function of vortex size.

Using the above results in Equation (4.18) the air entrainment model is obtained as

$$Q_\ell(\mathcal{V}) = S_{\ell 0}\frac{u_\ell^3 \ell^3}{g z_e^2} F(z/z_e), \qquad F(z/z_e) = \left(\frac{z_e}{z}\right)^3 \tilde{D}_s(z/z_e) \tag{4.24}$$

Recall that according to this model $z > \ell/2$ and therefore z never reaches zero.

4.5 Probability of breakage

The probability of breakage $P_B(D|\mathcal{V})$ represents the probability that a vortex $\mathcal{V}$ of size ℓ located at depth z' is energetic enough to break the surface and form a bubble with size D. The probability of breakage was introduced by Luo and Svendsen (1996) and later used by Lehr et al. (2002) in the context of bubble breakup by turbulence.

The mean energy required to form a bubble of size D is $e_s = \pi D^2 \sigma$ if only consider surface tension energy. Luo and Svendsen (1996) consider the probability of a vortex of size ℓ having energy larger than the formation energy, while Lehr et al. (2002) consider instead a force balance between dynamic and surface tension forces. Then they estimate probability of a vortex with size ℓ being able to provide a force larger than the critical value to break a bubble. In this thesis, the force balance approach is followed given that the model by Lehr et al. (2002) predicts breakup rates that are closer to experimental values. The dynamic pressure forces need to counteract the stabilizing effect of the surface tension, thus

$$\frac{1}{2}\rho_c u^2 \geq \frac{2\sigma}{D} \tag{4.25}$$

Fluctuations in velocity for vortices with a characteristic size ℓ approximately follow a Gaussian distribution with zero mean and a standard deviation equal to the characteristic velocity u_ℓ. If each component of the velocity vector follows a Gaussian distribution and is independent to each other, the speed, or velocity vector magnitude, then follows a Maxwellian distribution

$$p(u) = \sqrt{\frac{2}{\pi}} \frac{u^2}{u_\ell^3} e^{-\frac{1}{2}\left(\frac{u}{u_\ell}\right)^2} \tag{4.26}$$

From Equation (4.25) a bubble of size D can be formed by a vortex of size ℓ if $u > u_{\min} = \sqrt{4\sigma/(\rho_c D)}$. The probability for this to happen is

$$P_B(D\,|\,\mathcal{V}) = \int_{u_{\min}}^{\infty} du\; p(u) = \operatorname{erfc}(x) + \frac{2}{\sqrt{\pi}}\, x\, e^{-x^2} \tag{4.27}$$

with

$$\begin{aligned} x &= \frac{u_{\min}}{u_\ell\sqrt{2}} = \sqrt{\frac{2}{\mathrm{We}(D,u_\ell)}} \\ \mathrm{We}(D,u_s) &= \frac{\rho_c\, D\, u_\ell^2}{\sigma} \end{aligned} \tag{4.28}$$

Figure 4.6 shows the probability of breakage when the r.m.s. velocity u_ℓ follows the model in Equation (4.10) and the turbulent field is from Table 4.2.

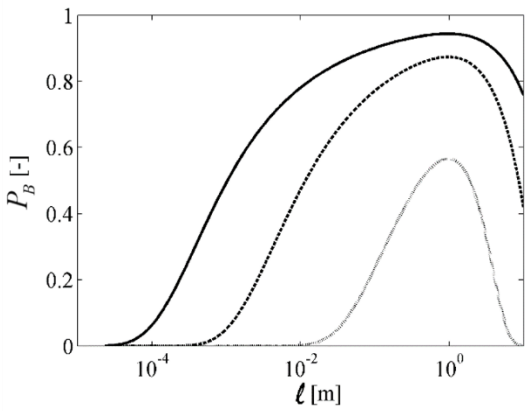

Figure 4.6: Probability of breakage as a function of vortex size for different bubble sizes. Solid: $D = 5$ mm, dashed: $D = 1$ mm, dotted: $D = 100\ \mu$m.

With this model $P_B = 0.57$ for $\mathrm{We} = 2.0$, $P_B = 0.80$ for $\mathrm{We} = 4.0$ and $P_B = 0.94$ for $\mathrm{We} = 10.0$. Critical Weber numbers in the range 3-4.7 have been measured by Lewis and Davidson (1982) and by Martínez-Bazán et al. (1999).

4.6 Size distribution of bubbles at formation

The probability of breakage $P_B(D\,|\,\mathcal{V})$ gives the probability that a vortex of size ℓ has the energy to form by breakage of the surface a bubble of size D. However, if a vortex has the energy to form a bubble with size D, it also has the energy to form bubbles of any

size larger than D. Therefore, the probability to form a bubble with any size within $(D, D+dD)$ is

$$p_0(D|\mathcal{V})\,dD = P_B(D+dD|\mathcal{V}) - P_B(D|\mathcal{V}) \approx \frac{dP_B(D|\mathcal{V})}{dD}\,dD \tag{4.29}$$

Thus the formation size distribution $p_0(D|\mathcal{V})$ is normalized by the probability of breakage,

$$\int_0^{\ell} dD_0\; p_0(D_0|\mathcal{V}) = P_B(\ell|\mathcal{V}) \tag{4.30}$$

Using the probability of breakage from Equation (4.27), the probability of formation of a bubble with size D by a vortex $\mathcal{V}$ is

$$p_0(D|\mathcal{V}) = \frac{\rho u_\ell^2}{\sigma}\frac{x^5 e^{-x^2}}{\sqrt{\pi}} \tag{4.31}$$

where x is the dimensionless variable defined in Equation (4.28). This expression is only valid for $D/\ell < 1$ since it is assumed that a vortex cannot entrain a bubble larger than itself. For the turbulent flows at the stern of the Athena summarized in Table 4.2, Figure 4.7 shows the size distribution of the bubbles for three vortex sizes.

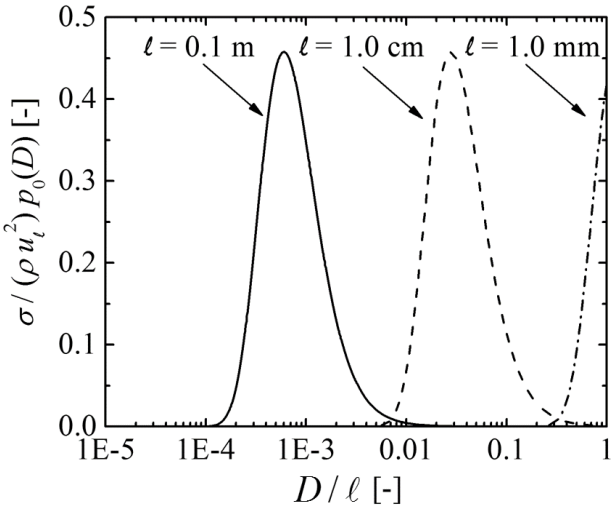

Figure 4.7**:** Bubble size distribution $p_0(D|\mathcal{V})$ of bubbles at formation using the parameters in Table 4.2.

4.7 Probability of finding a bubble at a given depth

Consider an idealized isotropic turbulent flow with zero mean velocity and mean free surface located at $z=0$. If air is entrained through the free surface at a constant rate eventually an equilibrium status is reached when the bubble entrainment rate is balanced by bubbles' loss as they rise and escape through the free surface. To obtain the equilibrium profile the steady state transport equation for $f(D)$ is solved neglecting breakup and coalescence

$$-\frac{\partial}{\partial z}\left(V_T(D)\ f(D,t)\right)=\frac{\partial}{\partial z}\left(\nu_t(z)\frac{\partial f(D,t)}{\partial z}\right) \tag{4.32}$$

where the turbulent viscosity ν_t is a function of the depth z only since the turbulent field is assumed homogeneous in the horizontal direction and the terminal velocity V_T is a function of the bubble size. Equation (4.32) can be solved as

$$\frac{\mathrm{d}\,f}{f}=-V_T\frac{dz}{\nu_t(z)} \tag{4.33}$$

Therefore, different solutions can be obtained depending on the functional form of ν_t for a given bubble size D. The solutions for different ν_ts is given in Table 4.3.

Table 4.3: Summary of analytical solutions for different functional forms of ν_t.

Turbulent profile type	Equations for ν_t	Bubble number density profile
Homogeneous	$\nu_t(z)=\nu_{t0}$	$f(z,D)=f_0(D)\,e^{-z/L_D}\quad L_D(D)=\nu_{t0}/V_T(D)$
Linearly decreasing	$\nu_t(z)=\nu_{t0}\left(1-z/L_{11}\right)$	$f(z,D)=f_0(D)\left(1-z/L_{11}\right)^{L_{11}/L_D}$
Exponentially decreasing	$\nu_t(z)=\nu_{t0}\,e^{-z/L_{11}}$	$f(z,D)=f_0(D)\exp\left(-L_{11}\left(e^{z/L_{11}}-1\right)V_T/\nu_{t0}\right)$

The homogeneous turbulence predicts a solution that exponentially decreases with depth. However it is as unrealistic as having uniform turbulence all the way to infinite depths. A more reasonable assumption is that if L_{11} is the integral length scale of

turbulence, turbulent fluctuations are damped away for depth larger than L_{11}. The linearly and exponentially decreasing profiles can be used to approximate this situation. Figure 4.8 shows the resulting profiles for the three cases with three different values of terminal velocity (and thus different bubble sizes). Turbulence scales are chosen to approximate those at Athena's stern as in Table 4.2.

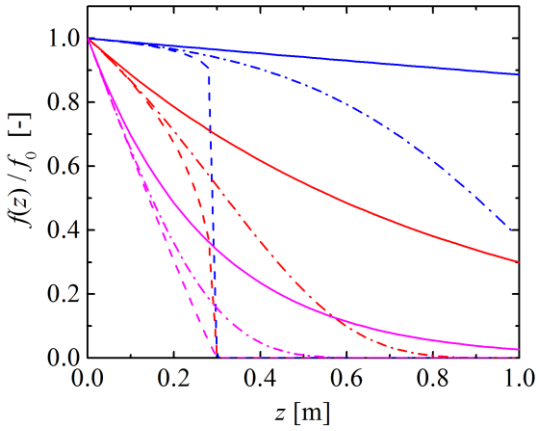

Figure 4.8: Bubble density profile for different turbulent profiles and terminal velocities. Turbulent values approximate Athena's stern. Solid: Homogeneous. Dashed dot: exponentially decreasing. Dashed: Linearly decreasing. Blue: $V_T = 0.01$ m/s. Red: $V_T = 0.1$ m/s. Magenta: $V_T = 0.3$ m/s.

The probability that a bubble of diameter D reaches a depth z can then be modeled using one of the previous solutions normalized to one

$$P_z(z \mid D) = \frac{f(z,D)}{\int_0^\infty dz\ f(z,D)} \tag{4.34}$$

In this thesis, the linearly decreasing turbulent viscosity is used then

$$P_z(z \mid D) = \frac{1}{L_z}(1 - z / L_{11})^{L_{11}/L_D} \tag{4.35}$$

with $L_z = \left(L_{11}^{-1} + L_D^{-1}\right)^{-1}$. L_z is always smaller than either L_D or L_{11}.

4.8 Simplifications of the general model framework

One of the advantages of the general framework stated in Equation (4.6) is that each term can be analyzed, ideally, separately from the others. However, a closed analytical expression may be difficult to obtain from performing these multiple integrals on complex functional forms of the integrands. This section presents a series of approximations used on the different terms in order to arrive to a closed analytical form.

4.8.1 Bubble size distribution history

The history function $p_h(D \mid D_0, z)$ is the size distribution of bubbles originally formed at the free surface with a diameter D_0 and that traveled a depth z into the water. A model for this history would require to deal with bubble transport equations including breakup and coalescence effects.

To be able to analytically integrate Equation (4.6), it is assumed that breakup and coalescence reach equilibrium instantly. Under such condition, $p_h(D \mid D_0, z)$ reduces to the equilibrium size distribution $p_{\text{eq}}(D)$ and therefore no longer depends on the initial bubble size and depth. This hypothesis of fast equilibrium is most likely not correct. However the approximation of a p_h independent on the bubble diameter of the originally formed bubbles allows to quickly obtain a usable approximation of the air entrainment framework. Further improvements to this model would include a more suitable model for p_h.

If history size distribution depends only on bubble size, namely, $p_h(D \mid D_0, z) \approx p_h(D)$. Equation (4.6) can be written as

$$S(D,z) = \frac{1}{\bar{v}_0}\, p_z(z \mid D)\; p_h(D) \int_0^{\infty} dz' \int_0^{2z'} d\ell\; Q_\ell(\mathcal{V})\; n_\ell(\ell) \int_0^{\ell} dD_0\; p_0(D_0 \mid \mathcal{V}) \qquad (4.36)$$

The innermost integral can now be computed using the definition of p_0 in Equation (4.30), reducing Equation (4.36) to

$$S(D,z)=\frac{1}{\bar{v}_0}\,p_z(z\,|\,D)\;p_h(D)\int_0^{\infty}dz'\int_0^{2z'}d\ell\;Q_\ell(\mathcal{V})\;n_\ell(\ell)\,P_B(\ell\,|\,\ell) \tag{4.37}$$

To simplify the integration of Equation (4.37) the order of integration between ℓ and z' is changed as

$$S(D,z)=\frac{1}{\bar{v}_0}\,p_z(z\,|\,D)\;p_h(D)\int_0^{\infty}d\ell\,n_\ell(\ell)\,P_B(\ell\,|\,\ell)\int_{\ell/2}^{\infty}dz'\,Q_\ell(\mathcal{V}) \tag{4.38}$$

In this work, the equilibrium size distribution is obtained from experiments. Johansen et al. (2010) measured size distribution at the bow of Athena R/V at several depths, and the closest measurement to the free surface at a depth of 10 cm is assumed to be turbulent equilibrium size distribution. Then the bubble history size distribution is replaced by

$$p_h(D)=\frac{p_t(D)\,/\,p_z(z=0\,|\,D)}{\int_0^{\infty}dD\,p_t(D)\,/\,p_z(z=0\,|\,D)} \tag{4.39}$$

such that at $z=0$ the entrainment size distribution given by Equation (4.38) reduces to the turbulent model size distribution $p_t(D)$, which is assumed to be that measured at the bow of Athena R/V where the entrainment occurs.

4.8.2 Single vortex entrainment

Using the change of variables $u=z/z_e$ the integral of Q_ℓ in z in Equation (4.38) can be written as

$$\begin{aligned}&\int_{\ell/2}^{\infty}dz'\,Q_\ell(\ell,z)=S_{\ell 0}\,\frac{u_\ell^3\ell^3}{g\,z_e}\,I_Q(\mathrm{Fr}_\ell)\\ &I_Q(\mathrm{Fr}_\ell)=\int_{u_{\min}}^{1}du\,F(u)\quad,\quad u_{\min}=\frac{0.428}{\mathrm{Fr}_\ell^{2/3}}\end{aligned} \tag{4.40}$$

where $F(u)$ is the function defined in Equation (4.24). The integral I_Q can be performed numerically and it is found that it can be approximated to within 5% by the function

$$I_Q(\mathrm{Fr}_\ell)\approx 0.808\,(5.46\,\mathrm{Fr}_\ell^{4/3}-1) \tag{4.41}$$

which is the analytical result obtained when using for the vortex ring diameter in Equation (4.23) the approximation

$$\frac{D_s}{z_e} \approx 1.615\, H(1 - z / z_e) \tag{4.42}$$

with $H(x)$ the Heaviside function. Figure 4.9 shows I_Q as a function of the vortex Froude number. This integral is zero for Froude numbers $\mathrm{Fr}_\ell < 0.28$. The Froude number decreases for large vortices due to $\mathrm{Fr}_\ell \propto \ell^{-1/6}$. Therefore, the fact that $I_Q = 0$ for small Froude numbers indicates that large vortices do not entrain air. This is consistent with the idea that very large vortices generate long wave length waves with slopes that are not steep enough to entrain air. I_Q increases for small vortices. The whole integral in Equation (4.40) goes to zero due to the factor $u_\ell^3 \ell^3 / z_e$ when the vortex size reduces to zero.

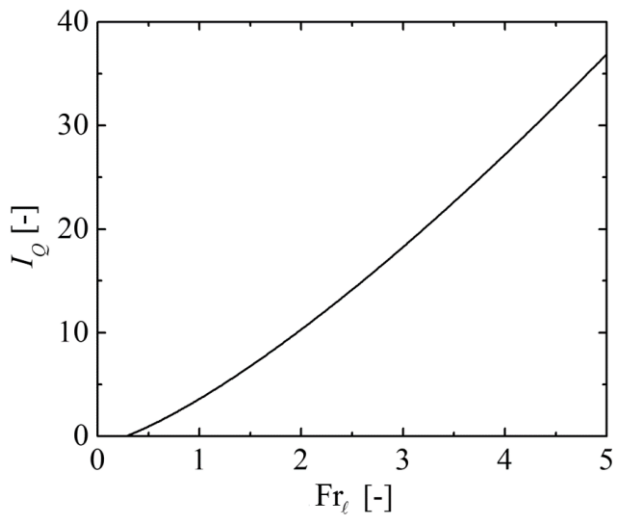

Figure 4.9: Single vortex entrainment source integrated in the depth coordinate.

4.8.3 Integral in vortex sizes

After above simplifications the entrainment model reduces to an expression requiring only a one dimensional integral

$$S(D,z) = S_{\ell 0}\frac{J}{\overline{v}_0}\, p_z(z \mid D)\; p_h(D)\Lambda(\alpha_d)$$

$$J = \int_0^\infty d\ell\, J_\ell(\ell) \tag{4.43}$$

$$J_\ell(\ell) = 0.8413\frac{f_L}{\ell^4} P_B(\ell \mid \ell)\frac{u_\ell^3 \ell^3}{g\, z_e} I_Q(\mathrm{Fr}_\ell)$$

where J is the total volumetric flux per unit area per unit time and J_ℓ represents the contribution to this flux from a vortex of size ℓ, $\Lambda(\alpha_d) = (1-\alpha_d)$. In order to terminate entrainment when void fraction is high, which is more realistic, another form of $\Lambda(\alpha_d) = \max(1-\alpha_d/\alpha_{dc}, 0)$ is proposed with α_{dc} is a critical constant (0.3 for this thesis) for entrainment. Given the wide spectrum of scales in a turbulent flow, the computation of the integral in Equation (4.43) is performed more accurately in a logarithmic scale. The change of variables $u = \ln(\ell)$ in Equation (4.43) results in

$$\hat{J} = \int_{-\infty}^{\infty} du\, \ell\, J_\ell(\ell) \tag{4.44}$$

The integrand is shown in Figure 4.10 for parameters from Table 4.2.

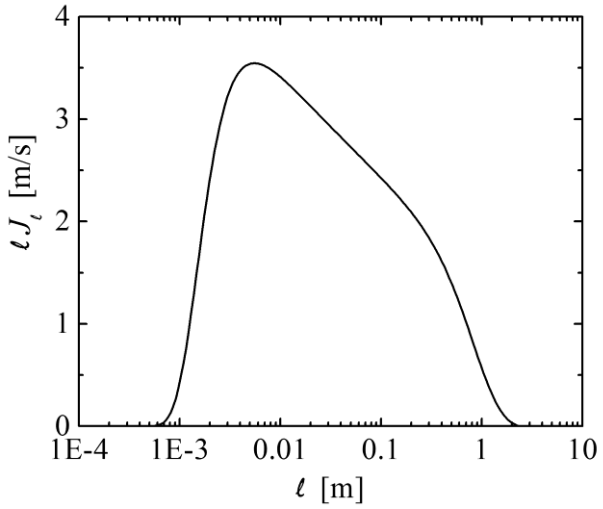

Figure 4.10: Contribution to the total air entrainment flux from vortices of size ℓ.

The flux J is found for several values of turbulent kinetic energy k_t and turbulent dissipation ε_t and is shown in Figure 4.11. While J always increases with ε_t, it eventually reaches a maximum asymptotic value in k_t. This is due to the fact that for a fixed ε_t increasing the value of k_t implies adding larger scales. As mentioned before when solving for I_Q in Equation (4.41), large vortices may only create long waves without breaking the surface to entrain air. Increasing ε_t however, keeping the value of k_t constant, has the effect of expanding the range of small length scales that are strong enough to break the surface.

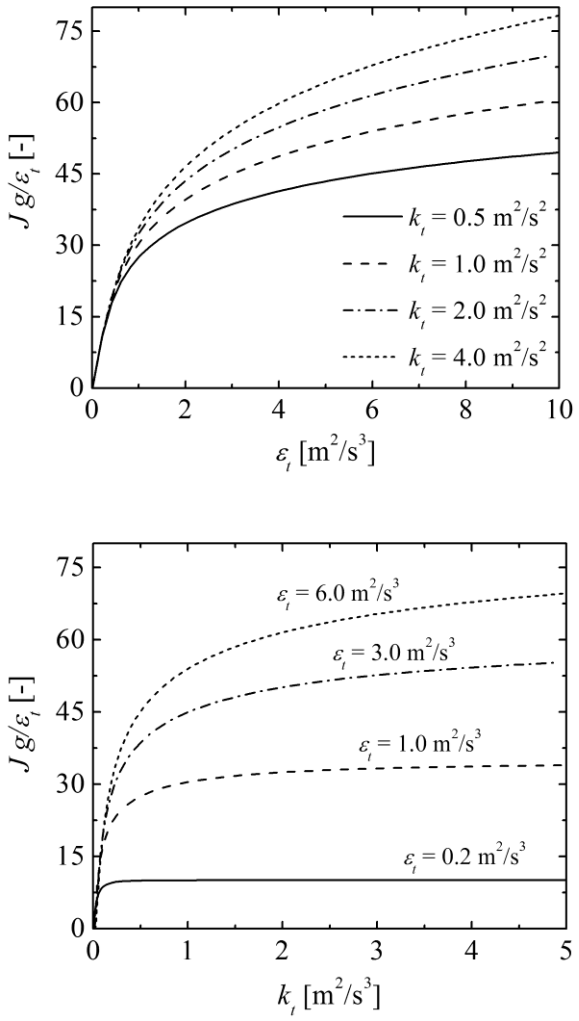

Figure 4.11: Air entrainment flux as a function of turbulent dissipation (top) and turbulent kinetic energy (bottom) for an air-water system.

4.9 Energetic considerations for the liquid phase

The entrainment model presented is a volumetric source active under the free surface. This means bubbles have to travel downward, requiring energy and momentum to make it happen. However the liquid governing equations do not describe the process of entrainment. Thus, if bubbles are entrained at surface level, work needs to be done to carry the bubbles deep into the liquid.

The potential energy per unit time required to entrain these bubbles to a depth ϕ is

$$\dot{E}^G = \int_0^\infty dD\, \rho_c\, g\, v(D)\, \phi\, S(D, \boldsymbol{x}) = \rho_c\, g\, \bar{v}_{\text{ent}}\, \phi\, S_d(\boldsymbol{x}) \tag{4.45}$$

where $\bar{v}_{\text{ent}}$ is the mean entrained bubble volume and $S(\boldsymbol{x})$ is the total entrainment source for void fraction. This energy to pull the bubbles down must be provided by the liquid phase and therefore the momentum change of the liquid pushing bubbles down is

$$\frac{dP}{dt} = \frac{\dot{E}^G}{V} \tag{4.46}$$

where V is the averaged downward velocity with which the bubbles are being entrained from the free surface to depth ϕ. The loss of momentum can be accounted for in the dimensional momentum equation as

$$\frac{\partial \alpha_c \rho_c \mathbf{u}_c}{\partial t} + \nabla\cdot(\alpha_c \rho_c \mathbf{u}_c \otimes \mathbf{u}_c) = -\nabla \hat{p}_c + \nabla\cdot\left(2\alpha_c \mu_{eff,c} \nabla^s \mathbf{u}_c\right) + \alpha_d \rho_c\, g\left(1 - \frac{\rho_d}{\rho_c}\right)\hat{k} - \frac{\dot{E}^G}{V}\hat{k} \tag{4.47}$$

where V needs to be estimated appropriately from the average downward velocity of the entrained bubbles, $\mu_{eff,c}$ is the effective dynamic viscosity, $\hat{p}_c$ is the piezometric pressure.

Since bubbles are entrained by turbulent vortices in the model presented, the turbulent kinetic energy has to decrease correspondingly due to the energy it takes (a) to entrain the bubbles and (b) to transport them to depth as in Equation (4.45). Entraining bubbles requires a minimum formation energy given by $a(D)\sigma$ with $a(D)$ the surface area of a bubble with size D.

The formation energy is probably larger than this surface tension energy due to the simultaneous formation of surface waves. A first approximation of the energy rate supplied to form entrained bubbles is

$$\dot{E}^{\sigma} = C_{\sigma} \int_0^{\infty} dD\, a(D)\, \sigma\, S(D, \boldsymbol{x}) = C_{\sigma}\, \bar{a}_{\text{ent}}\, \sigma\, S_d(\boldsymbol{x}) \tag{4.48}$$

where C_{σ} is a factor larger than 1, $\bar{a}_{\text{ent}}$ is the mean bubble surface area. The formation energy equals potential energy (one bubble size) at a depth

$$\phi = \frac{3C_{\sigma}\sigma}{\rho_c g R} \tag{4.49}$$

As an example and arbitrarily assuming $C_{\sigma} = 3$, Equation (4.49) yields a depth of 0.132 m for a bubble of $1\,\text{mm}$ diameter.

The model presented in this work assumes that bubbles are entrained by a process of energy exchange between turbulence and the free surface. Thus, the turbulent kinetic energy must decrease as bubbles are entrained. This turbulent energy loss can be included as a source of energy dissipation in the two phase blended k-ε / k-ω SST model (Moraga et al. 2008) used in this research.

$$\alpha_c \frac{Dk}{Dt} = \alpha_c \mathbf{T}_c^{Re} : \nabla \mathbf{u}_c + \nabla \cdot \left[\alpha_c (\nu_c + \sigma_k \nu_t) \nabla k \right] - \alpha_c \beta^* \omega k - \alpha_c (\dot{E}^G + \dot{E}^{\sigma}) \tag{4.50}$$

$$\begin{aligned} \alpha_c \frac{D\omega}{Dt} = {} & \alpha_c \gamma \frac{\omega}{k} \mathbf{T}_c^{Re} : \nabla \mathbf{u}_c + \nabla \cdot \left[\alpha_c (\nu + \sigma_{\omega} \nu_t) \nabla \omega \right] - \alpha_c \beta \omega^2 - \alpha_c \frac{\omega}{k} \frac{\beta}{\beta^*} (\dot{E}^G + \dot{E}^{\sigma}) \\ & + 2\alpha_c (1 - F_1) \frac{\sigma_{\omega 2}}{\omega} \nabla \omega \cdot \nabla k \end{aligned} \tag{4.51}$$

The energetic considerations involving in this section complicate the modeling strategy, however it is physical requirement on the state art of entrainment modeling. In this thesis, only the term in turbulent kinetic energy equation is included with $C_{\sigma} = 1$ as a first approximation.

4.10 Free surface turbulence model

The prediction of the turbulent entrainment model requires a suitable turbulence model near the free surface. Present turbulence models are calibrated in flow without free surface. Hirt (2003) found existing turbulence model cannot predict enough turbulence near impact region to active air entrainment model in a plunging jet simulation. In addition, single level set does not include surface tension and air action to liquid which can disturb free surface. These factors can enhance the momentum mixing near the free surface. The RANS simulation with single level set method cannot describe such behavior near the free surface. Here it is proposed to model these behaviors as turbulent mixing resulting in increasing turbulence level near the free surface. A simple mixing length free surface model is developed to improve the turbulence prediction account for above reasons.

This model introduces a new production term in the turbulent kinetic energy equation that attempts to model the generation of these free surface fluctuations. It can be written as

$$\begin{aligned} P_\lambda^k &= 2\nu_\lambda S_{ij}\frac{\partial u_i}{\partial x_j} \\ \nu_\lambda &= (C_\lambda \lambda)^2 \|\mathbf{S}\| \max\left(1-\phi/\lambda, 0\right) \\ \|\mathbf{S}\| &= \sqrt{2S_{ij}S_{ij}} \end{aligned} \tag{4.52}$$

where ν_λ is a new turbulence viscosity, λ is the length scale of the free surface roughness, ϕ is the distance to the free surface, C_λ is a constant. The max function enforces this turbulence model to be active only close to the free surface.

4.11 Model limitations

In the development of model there are a number of assumptions and approximations. It should be kept in mind that these limitations are the result of the attempt to describe a complex phenomenon using simple descriptions in order to close the model. The idea is to reasonably capture main physical process and enable the model to be

implemented in CFD code conveniently. The following list attempts to identify and summarize the major model limitations:

1. Potential flow model for vortex interaction with free surface in a turbulent flow situation. The free surface deformation is different when considering viscous and surface tension effect, which is quite difficult, if not impossible, to obtain.
2. Superposition of the combined effects of several turbulent scales. The total air entrainment is assumed to be integral of each entrainment rates caused by a continuum of turbulent scales. It does not consider the interactions between different scales and corresponding effects to free surface deformation resulting in difference in entrainment rates.
3. Model does not separate small scales and larger scales energetic enough to generate chunks of water that separate from the main fluid and collapse back again in the turbulent field. The model assumes the free surface is mildly deformed and no detached water is generated. In reality droplets can be generated near the free surface which can also cause entrainment.
4. Different geometrical/topological configurations are not considered. The model presented mainly considers vortex energetics though particular configurations may have different impacts on air entrainment. Vortex rings parallel to the free surface, funnels, and line vortices aligned with the free surfaces are possible examples of particular configurations.
5. Homogeneous and isotropic turbulence is assumed in order to obtain closed relations. In reality the flow is highly anisotropic and inhomogeneous near the free surface. No simple models available in literature to describe these regimes. Even though LES/ DES could be used in these regions, it complicates the modeling due to the topological changes of the free surface and difficulty to estimate average turbulent levels required for the proposed model.

4.12 Air entrainment by impact

As a boat moves forward and hits incoming free surface disturbances at high speed it can entrap air cavities. This process is not accounted for in the turbulent air entrainment model presented in this thesis. A schematic of the air entrainment process is shown in Figure 4.12. A model assuming that a fraction of the volume in these cavities is entrained can be written as

$$S_d d_e d_w b = C(\lambda) b \delta_{FS} U_0 \tag{4.53}$$

where U_0 is the boat speed, b is the width in the perpendicular direction, λ is the wave length and C represents the fraction of total air contained by these cavities that results in entrainment and can be a function of the wave length. δ_{FS} is the peak to peak amplitude of the free surface waves. The entrainment is assumed to occur in a region of size d_w in direction normal to the wall with depth d_e. The final form of the impact entrainment source is then written as

$$S_d = C(\lambda)\delta_{FS} U_0 / d_e d_w \Lambda(\alpha_d) \tag{4.54}$$

where $\Lambda(\alpha_d)$ is added to avoid entrainment when large amounts of bubbles are already present in the flow (high void fraction prevents further entrainment) as done in Equation (4.43). This model is relevant to Kann boat simulations, presented in Chapter 5.

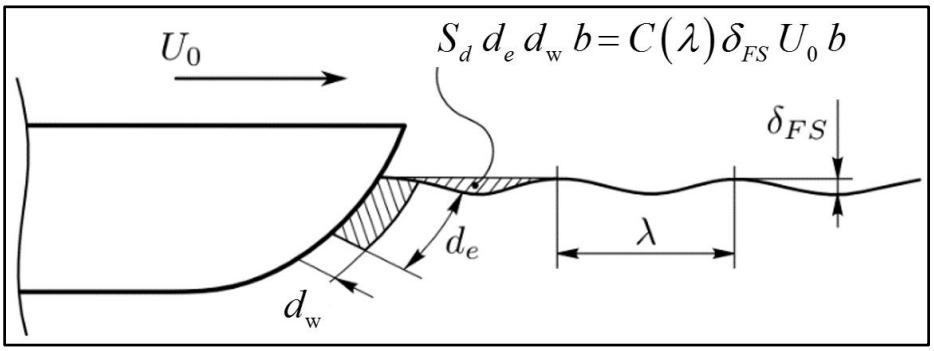

Figure 4.12: Schematic of entrainment due to impact motion.

CHAPTER 5 MODEL VALIDATION AND APPLICATION IN BUBBLY FLOW AROUND SHIPS

The turbulent air entrainment model presented in the previous chapter has a constant that needs to be calibrated against experimental data. As far as the author knows, there is no experiment aimed to measure bubble entrainment purely due to turbulence. To obtain the modeling constant, a breaking bow wave case with extensive data, in which turbulent entrainment is an important factor is chosen as an evaluation case. Though it is an application of the turbulent entrainment model a bit beyond its original assumptions, it can assess the capabilities of the model in natural entrainment conditions present around a ship.

Section 5.1 describes the simulation of a breaking bow wave (Tavakolinejad 2010). The model constant is estimated to match this experimental data. In the following two sections, the calibrated model will be used to simulate the two phase flow around the full scale craft Athena R/V and Kann boat. These simulations can evaluate the entrainment model in relevant problems involving complex geometries and flows, testing the robustness of the numerical scheme in demanding 3D simulations.

5.1 2D+T bow wave breaking simulation

5.1.1 Simulation setup

Bow wave breaking is a key process causing entrainment around ships. Tavakolinejad (2010) performed a set of experiments to simulate the passage of a ship using a 2D+T technique. A steel plate deforms in time to model the shape of a ship crossing a plane in time, as shown in Figure 5.1. The water is pushed away by the steel plate, resulting in a transient wave in the tank that mimics the waves at different axial cross sections in an advancing ship. The experiment simulated a scaled DTMB 5415 model with a waterline length $L = 21.03\text{m}$ moving at the speed $U = 5.441\text{m/s}$. Based on these two

scale parameters, the Froude and Reynolds numbers are $Fr = 0.379$ and $Re = 1.14 \times 10^8$, respectively. The Tank used in the experiment is $14.8\,\text{m}$ long, $1.15\,\text{m}$ wide, and $2.2\,\text{m}$ deep.

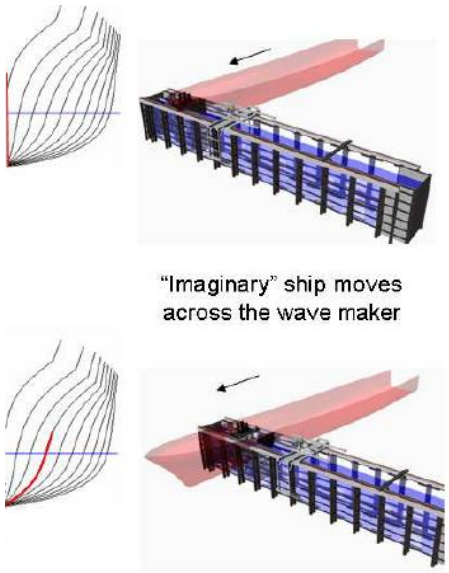

Figure 5.1: Deformed board and wave tank for experiment. (Figure is from Tavakolinejad, 2010)

To discretize such a large domain while retaining a proper level of refinement for the plunging breaker and the regions of interest where bubbles are formed, three blocks are designed. The overset grid system is shown in Figure 5.2. Block 1 (68 K grid nodes) discretizes the large wave tank used in the experiment. The deformable wall of the wave maker advances from left to right in Figure 5.2. In the computation this is simulated by deforming the left side of the domain to follow the experimental wall profile shapes. The shape of the board is linearly interpolated in time from the wave board profiles reported in the experiment. To maintain the quality of the grid the inner grid points of Block 1 are moved using a series of simple linear interpolations between pre-generated grids together with smoothing. Thirteen 2D grids are designed for the interpolations representing typical time series. Blocks 2 (221 K grid nodes) and 3 (234 K grid nodes) are used to refine the

solution domain in the areas of interest, taking advantage of the overset capabilities of the code. Block 3 consists of a Cartesian grid that rigidly moves in time to follow the main features of the wave created and the clouds of bubbles entrained. Block 2 consists of a second smaller Cartesian grid that follows the position of the breaker. It is a refinement to properly capture the plunge and subsequent cavity formation and collapse.

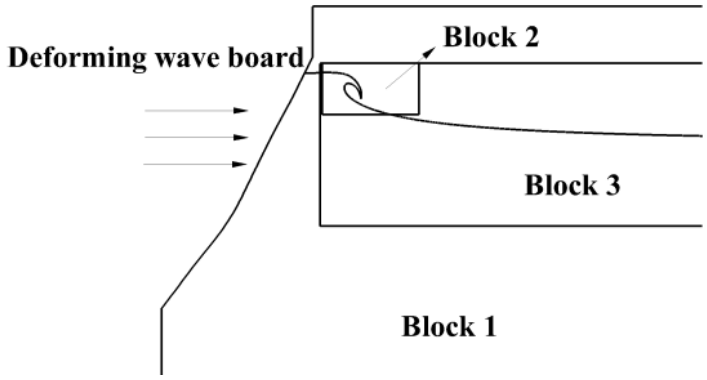

Figure 5.2: Overset grid system for 2D+T wave maker simulation.

Table 5.1: Grid details for simulation

Grid	I	J	Total
Block 1	226	301	68K
Block 2	657	337	221K
Block 3	969	241	234K

The trajectory of the refinement blocks, which move following the evolution of the features of interest, is estimated from an initial single phase run. In all the following simulations the time step is set at $\Delta t = 5.4\times10^{-4}\,\mathrm{s}$. The two phase blended $k-\varepsilon/k-\omega$ SST turbulence model (Moraga et al. 2008) is used to predict the turbulence field for the air entrainment model.

5.1.2 Model application to wave breaking process

As explained in Chapter 1, the entrainment during a wave breaking process involves many entrainment mechanisms. However, it is insightful to test whether the model functions as expected in such turbulence-dominated process.

A numerical experiment is carried out at first with four bubble groups to estimate constants in the models. Bubble diameters span from $20\,\mu m$ to $1\,cm$. These bubbles are uniformly distributed in a logarithmic scale. Bubble group information is shown in Table 5.2. D_g^{ent} is the group size distribution used for estimating the history size distribution, obtained from the data measured at the bow of Athena R/V (Johansen et al. 2010).

Table 5.2: Entrainment size distribution for groups.

Group No.	Radius (μm)	D_g^{ent}
1	10	9.14×10^{-1}
2	80	8.09×10^{-2}
3	630	4.66×10^{-3}
4	5000	0

The turbulent entrainment model requires reasonable turbulence quantities to activate the model. However, existing RANS turbulence models do not consider the effect of the free surface. For this breaking wave simulation, as shown later, the value of turbulent kinetic energy predicted by the blended $k-\varepsilon/k-\omega$ SST turbulence model at the jet impact region is negligible. As a result, the air entrainment model does not activate as it should and the void fraction distribution shows that the first bubble cloud is not as clear as the second one (in the experiment, two distinct clouds are generated in the wave tank. The one near the wave board is referred to as the first cloud, see Figure 5.10). Hirt (2003) proposed to enhance turbulence levels by adding extra energy, which would help activate the entrainment model in the simulation of a plunging jet.

It is known the impact of the plunging jet formed at wave breaking can result in significant turbulence at impact that produces bubble entrainment. Based on this fact, additional turbulence is introduced to Menter (1993) turbulence model. A first change is to remove the production limit in the two phase turbulence model to generate free surface turbulence. According to Menter (1993), the production term in the kinetic energy equation is limited as $P_k = \min\left(P_k, 20\varepsilon_t\right)$, where P_k is the production due to shear. This limit is originally designed to remove unphysical turbulence generation due to numerical wiggles in the velocity field and turbulence accumulation near stagnation regions at solid boundaries. Though shown to provide good agreement with experiments in the simulation of flows with stagnation points such as airfoils, this limit actually does not have a clear physical motivation. Quite the opposite, the original $k-\varepsilon/k-\omega$ equations without this limit carry the proper physical scaling. It is therefore for this reason we propose to remove Menter's limit in regions away from bodies. Even though further research is needed to study this term in broader free surface flows with strong shear, the results shown in this thesis are encouraging to justify removing the limit away from bodies Also, the mixing length turbulence model developed in Section 4.10 is activated to introduce extra turbulence when there is high shear flow motion near the surface. From now on these two measures will be referred as MNL (Menter's model with No Limit in production) and ML (Mixing Length model near the free surface) for short. The original two phase turbulence model by Menter (1994) as modified by Moraga (2008) for two-phase flows is referred as TPM (Two Phase Menter's blended $k-\varepsilon/k-\omega$ model). According to the ML, the length scale of surface roughness can be estimated from the jet thickness. Simulation results show the jet thickness is around 1cm. A length scale of 0.5cm is then estimated for the simulations. The constant c_λ in the mixing length turbulence model and entrainment constant $S_{\ell 0}$ are calibrated against experimental data as $c_\lambda = 0.001$ and $S_{\ell 0} = 2.6\times 10^{-2}$, after several numerical tests and iterations to match Athena's experimental data at the stern , where turbulent entrainment is the main mechanism of aeration.

Additional simulations with 15 groups are performed to describe bubble size distributions in more detail with the calibrated constants. These groups are also uniformly distributed in a logarithmic scale as listed in Table 5.3, and are also used in Athena R/V simulations later on.

Figure 5.3 shows comparisons of turbulent kinetic energy for different proposed turbulence models. As it can be observed, the turbulent kinetic energy in TPM case is extremely small or negligible. The TPM+MNL case shows significant amount of turbulent kinetic energy at the impact region. For the last case, the kinetic energy level is increased further due to the mixing length model. The turbulent kinetic energy is mainly generated at the high shear region of impact and then is transported near the surface as shown in the figure. It is found that the production of turbulent kinetic energy from TPM+MNL is around 50 to 100 times that from the mixing length model at the impact region. This indicates that the difference in kinetic energy should not be significant between TPM+MNL and TPM+MNL+ML, which is also manifested by the contour levels in the figure. Figure 5.4 shows the entrainment sources for three different cases. As expected that the TPM has no entrainment for bubbles while TPM+MNL+ML has the strongest source. Bubbles entrained can enforce liquid out of that region due to mass conservation, as explained in Chapter 3. The increase in the thickness of the little splash is a good example. The closed cavity does not break into bubbles as in the experiment due to the single phase level set method limitations, but the entrainment model can help to close the cavity and replace the cavity with mixture flow when bubbles are entrained around the cavity.

Void fraction contours for $x/L = 0.5$ are shown in Figure 5.5. The TPM case has one cloud formed by the second plunging breaker while the first cloud is not evident because no entrainment occurs for the first plunging breaker. Although there are two bubble clouds for the TPM+MNL case, the void fraction is not as high as that in TPM+MNL+ML case and the depth that bubbles can reach is smaller. Another notable feature is the bubbles entrained at the right of surface wave. The turbulence level there near

the free surface is not high but enough to entrain bubbles according to the entrainment model. In the experiment, it can be observed this entrainment is spilling wave type entrainment with droplet entrainment. As a conclusion, the turbulence level for the first plunging jet is crucial to the formation of bubble clouds and the depth bubbles can reach. The TPM+MNL+ML case shows the best match with experimental data on the wave breaking process.

Table 5.3: Air entrainment bubble size distribution for 15 groups.

Group No.	Radium (m)	D_g^{ent}
1	1.00E-05	3.19E-01
2	1.56E-05	2.98E-01
3	2.43E-05	1.73E-01
4	3.79E-05	9.50E-02
5	5.90E-05	5.22E-02
6	9.20E-05	2.86E-02
7	1.43E-04	1.57E-02
8	2.24E-04	8.64E-03
9	3.49E-04	4.75E-03
10	5.43E-04	2.61E-03
11	8.47E-04	1.43E-03
12	1.32E-03	7.86E-04
13	2.06E-03	3.59E-04
14	3.21E-03	0.00E+00
15	5.00E-03	0.00E+00

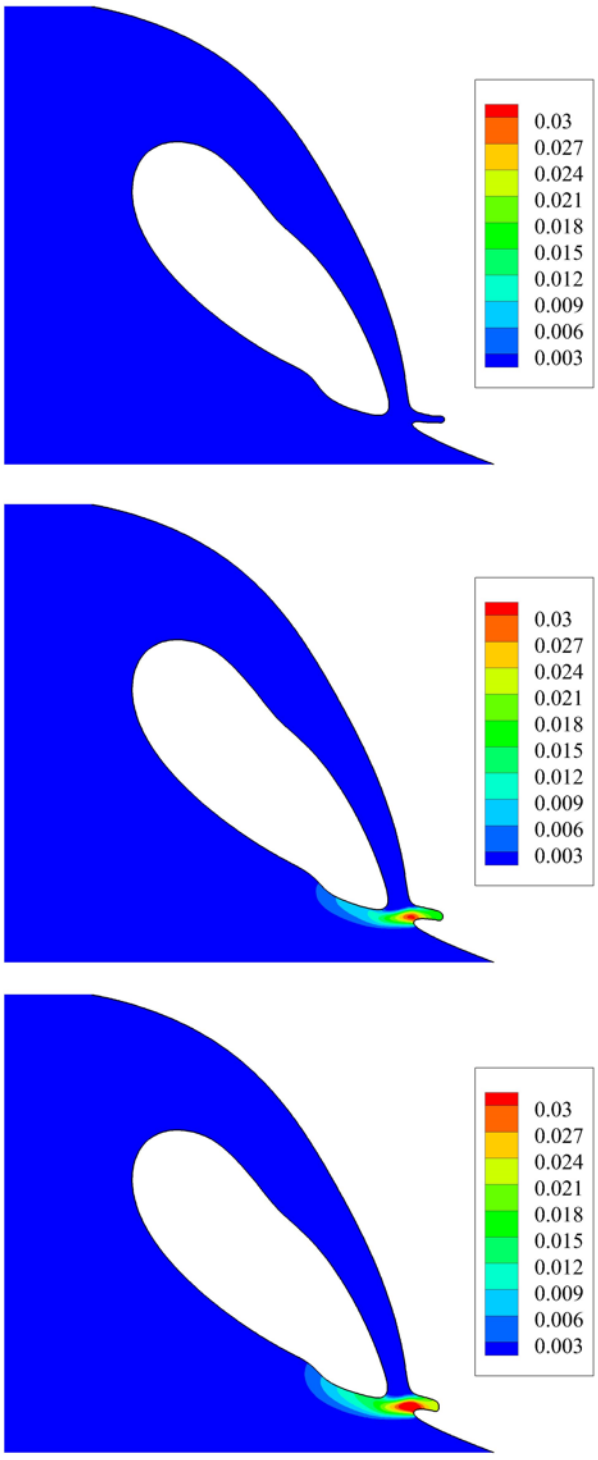

Figure 5.3: Turbulent kinetic energy at $x/L = 0.18$ for TPM (Top), TPM+MNL (Middle), TPM+MNL+ML (Bottom) when the jet hits on the free surface.

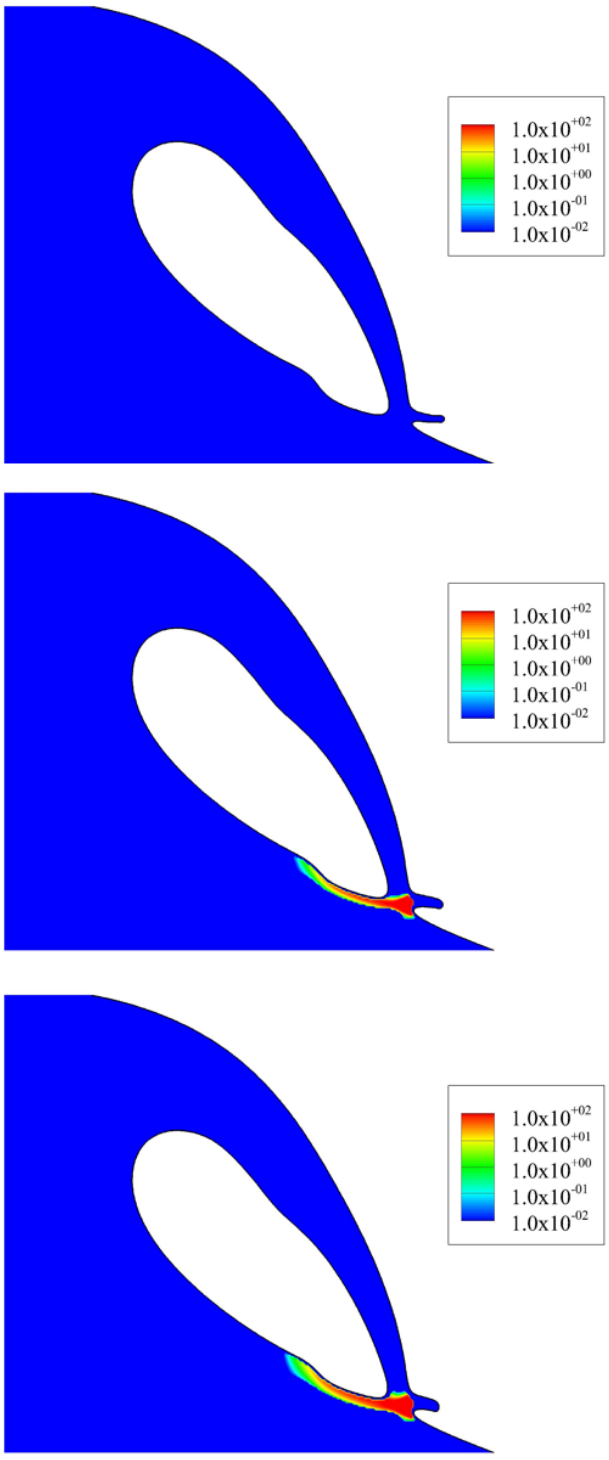

Figure 5.4: Void fraction entrainment source at $x/L = 0.18$ for TPM, TPM+MNL and TPM+MNL+ML. The order is the same as in Figure 5.3.

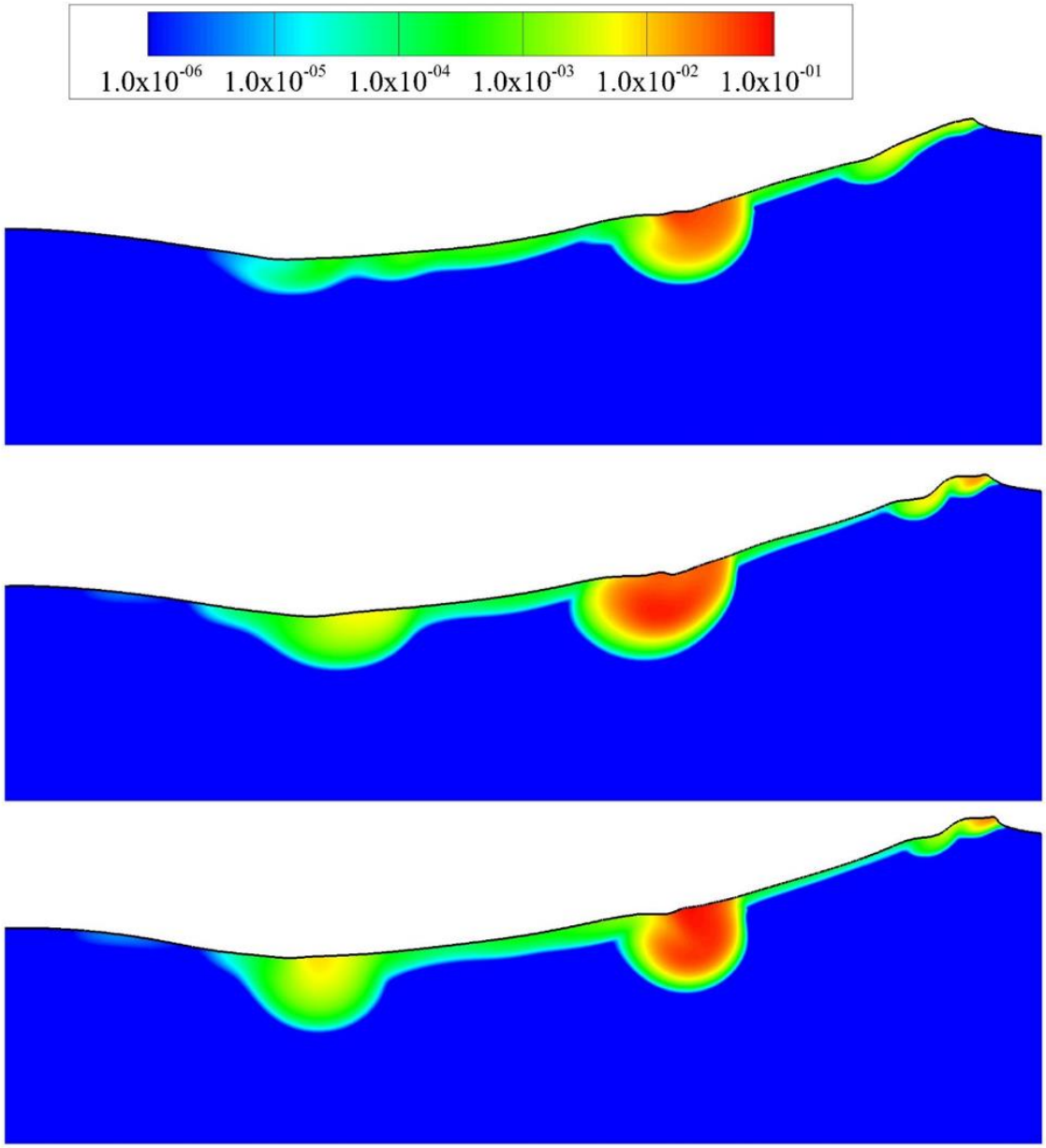

Figure 5.5: Void fraction contours at half ship length ($x/L=0.5$) for TPM, TPM+MNL and TPM+MNL+ML. The order is the same as in Figure 5.3

The turbulent dissipation is shown in Figure 5.6. The dissipation is extraordinarily high at the impact region where the maximum magnitude is approximately $\varepsilon_t \sim 100\,\mathrm{m}^2/\mathrm{s}^3$. Moraga et al. (2008) reported the maximum dissipation $\varepsilon_t \sim 68\,\mathrm{m}^2/\mathrm{s}^3$ in a simulation of 3D breaking bow wave generated with a low free stream velocity and flat plate, different

from this case. In the experimental work by Deane and Stokes (2002) and Loewen and Meville (1991), the cited estimation of the dissipation is around $\varepsilon_t \sim 13\,\mathrm{m}^2/\mathrm{s}^3$. The value is reported at the start of the breaker in this work while it can dramatically and quickly decrease as the breaker develops. As a result, the average value in the entrainment region might be much smaller than $100\,\mathrm{m}^2/\mathrm{s}^3$. It is believed that the dissipation generated in TPM+MNL+ML case is appropriate and acceptable when considering those different breakers and the complexity of the problem.

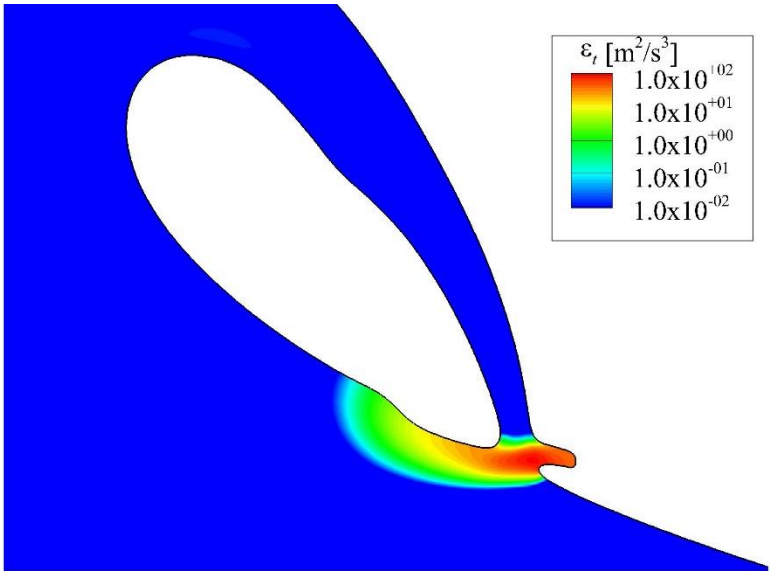

Figure 5.6: Turbulent dissipation contours for TPM+MNL+ML at $x/L = 0.18$.

Figure 5.7 shows the void fraction contours around the impact region. The void fraction can reach 0.3 in 0.02 seconds due to the high turbulence levels driving a strong entrainment. Figure 5.8 shows the entrainment source for the subsequent splash and breaking. As can be seen in Figure 5.8(a), there is entrainment source around the large cavity, which can help the cavity close and break faster. Also, a strong source is active for the splashed fluid. In the experiment the splash includes droplets, bubbles and a violent free surface, absent in a RANS simulation result. For the second breaker, formed by the splash, the entrainment source is active near the surface. As is the case for the first breaker,

the strength is higher at the impact region. Since the flow is highly turbulent after the first breaker, a broad area near the surface is observed to entrain bubbles, as shown in Figure 5.8(b). The resulting two bubble clouds are formed from the two breakers.

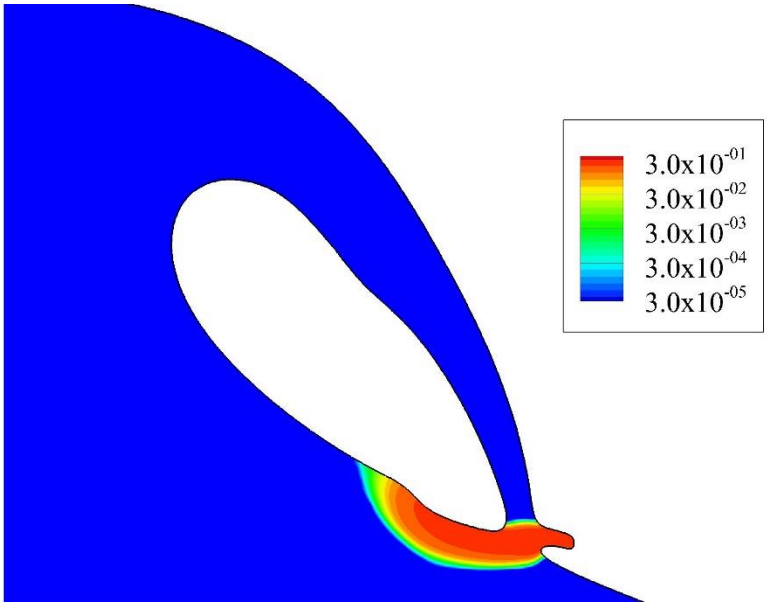

Figure 5.7: Void fraction contours around the jet impact region for TPM+MNL+ML at $x/L = 0.18$.

According to the study of the entrainment process by different turbulence approaches, we believe that TPM+MNL+ML can predict reasonable turbulence levels during the wave breaking process, allowing the turbulent entrainment model to work satisfactorily for this complicated wave process. Unfortunately no data is available to validate the turbulent quantities predicted by the model, but extensive comparisons with available data are presented in the following section.

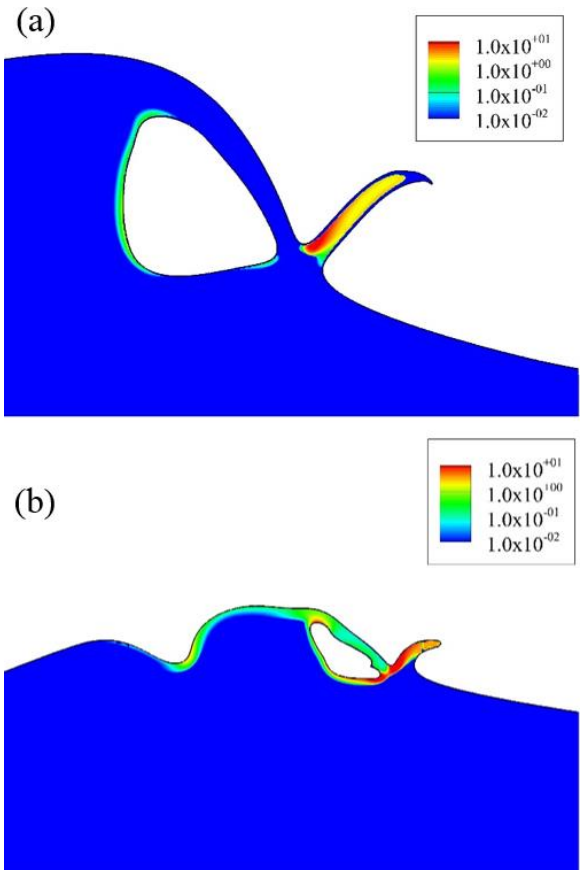

Figure 5.8: Contours of void fraction entrainment source for TPM+MNL+ML at (a): $x/L=0.208$; (b): $x/L=0.319$.

5.1.3 Model comparison with experimental data

Tavakolinejad (2010) reported extensive experimental data of bubbly flow for the breaking bow wave. These results can be used to evaluate the performance of the entrainment model. The simulation is performed with 15 groups listed in Table 5.3 using TPM+MNL+ML. The profile of surface elevation at the wave board exhibits good agreement with the experimental data, as shown in Figure 5.9, where the elevation is non-dimensionalized with the ship draft D and time with the wavemaker run time T_{wm}.

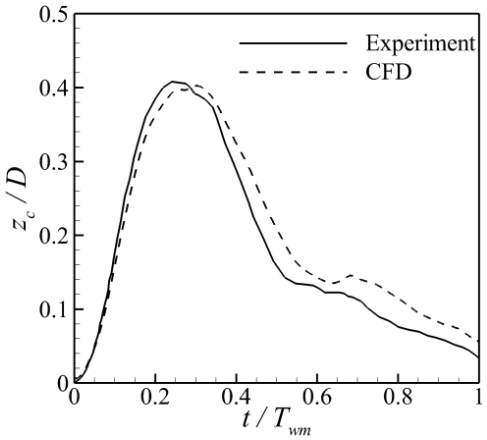

Figure 5.9: Surface elevation on wave board versus time.

Bubble clouds are reported in detail for the half ($x/L=0.5$) and one ship length ($x/L=1$) positions. Figure 5.10 shows two bubble clouds at $x/L=0.5$ for experiment and simulation. The experimental location of the two clouds is estimated from void fraction contours in the work by Tavakolinejad (2010). Numerical results predict two clouds qualitatively similar to those observed in the experiment. The thin layer of bubbles to the left of the second cloud is also predicted by current model. Though the positions of the two clouds do not match the experimental data perfectly, the trends are promising when considering the complexity of the flow and entrainment processes involved. Further research would be required to refine the model and obtain an even better match.

It is well known that the bubbles are not uniformly distributed under the free surface, therefore a good comparison requires the knowledge of experimental process to retrieve data. Figure 5.11 presents the experimental measurement regions in blue, where bubbles are measured bubbles inside each window. The experiment is performed several times and raw data is ensemble averaged.

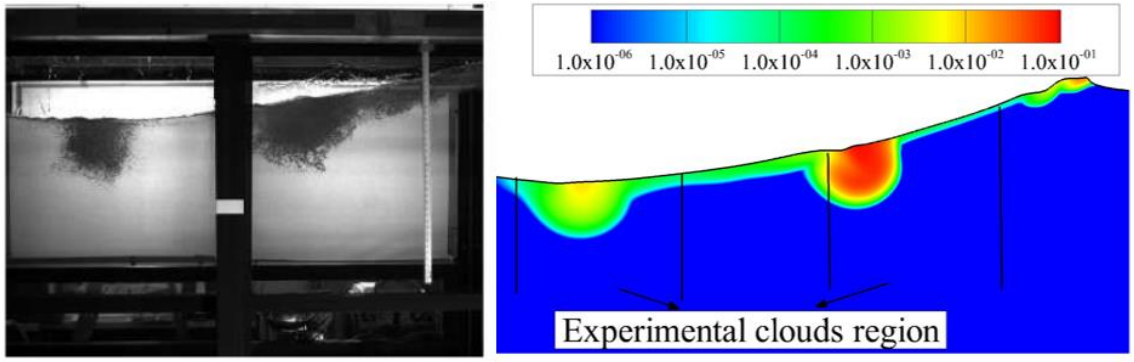

Figure 5.10: Bubble clouds at $x/L=0.5$. Experiment (left) and void fraction contours (right). (Experimetal figure is from Tavakolinejad (2010))

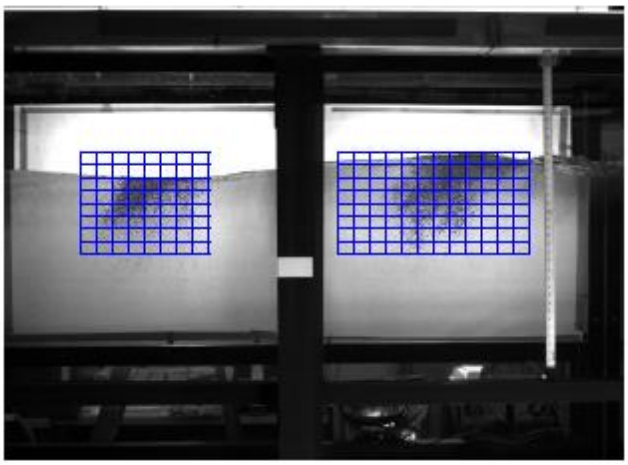

Figure 5.11: Experimental measurement regions. (Figure is from Tavakolinejad (2010))

Predicted bubble size distributions for two clouds at different positions are shown in Figure 5.12. The experimental data from Tavakolinejad (2010) is originally averaged over the entire bubble cloud. The bubble size distributions predicted by the model are reported at three depths in each cloud since the precise experimental region over which the ensemble averages were taken is not available. The profiles' slopes for small bubbles have good agreement with experimental data. Between the two positions, small bubbles do not escape significantly due to their low terminal velocities, while larger bubbles in simulation exit more quickly than in the experimental data. Also, the size distributions for large

bubbles at different depths indicates that large bubbles do not reach deep due to their high terminal velocities. These large bubbles rise up to surface and escape quickly resulting in steeper slope from $x/L=0.5$ to $x/L=1$.

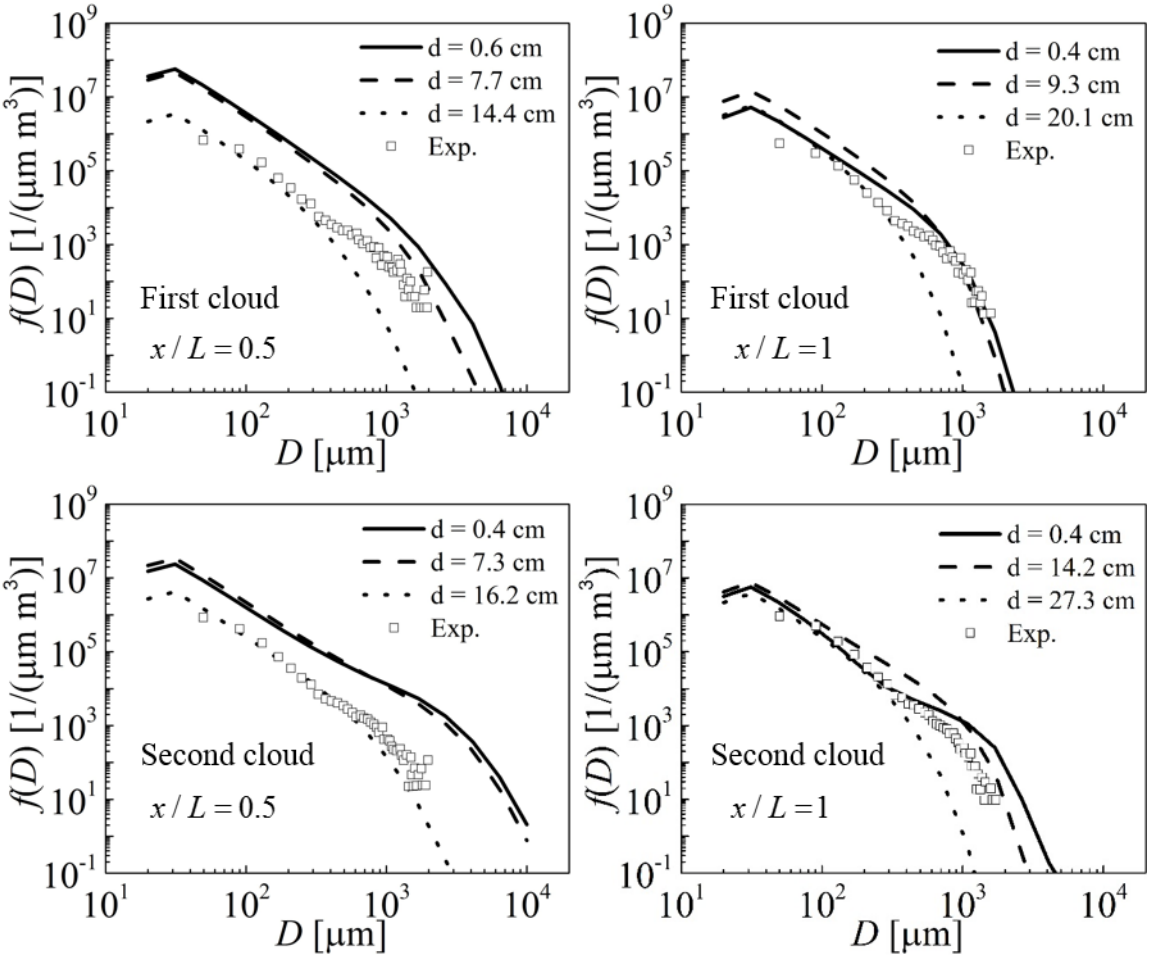

Figure 5.12: Bubble size distribution for first (top) and second (bottom) clouds. d in the legend indicates the distance to the free surface.

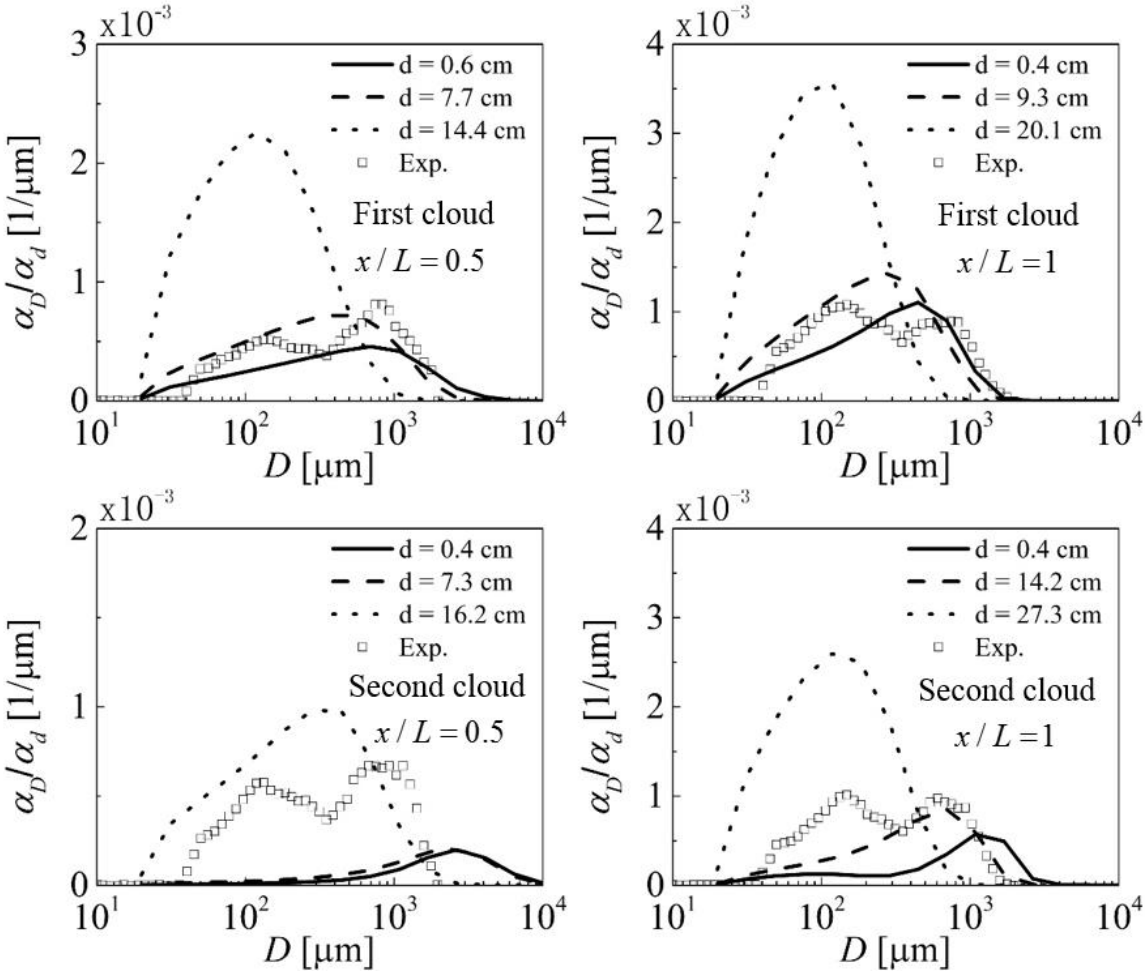

Figure 5.13: Normalized void fraction size distribution for first cloud (top) and second clouds (bottom).

Normalized void fraction size distributions are shown in Figure 5.13. The simulation results are obtained from the same positions as those in Figure 5.12. It can be observed that the two phase model cannot predict the bimodal behavior present in the experimental data. This bimodal distribution could be due to the averaging process over all the experimental cloud, counting small bubbles at the bottom and bigger on top. For the first cloud, profiles are close to the experiment data except for the deepest position, where small bubbles contribute to the most part of void fraction. More large bubbles are predicted for the second cloud resulting in a lower value of the peak because the profiles have to preserve unit area. Overall, the amount of large bubbles decreases when going deeper, as

indicated by the shifting peaks from large to small bubbles in simulation results. It is also noticed that the peaks for the deepest position occur close to the left peaks in experimental data, supporting the view that the bimodal behavior may be caused by the average processing. On the other hand, the bimodal distributions observed in the experimental data provide some hints to improve the entrainment model:

1. The entrainment size distribution could be bimodal.
2. Cavity fragmentation (large bubbles) and droplet impact entrainment (small bubbles) may be needed and require additional modeling.

Figure 5.14 shows the void fraction as a function of depth. Three lines are extracted from simulation results to represent the variation of void fraction in each cloud. The bubbles for the first cloud cannot reach as deep as those in the experiment, although the bubbles go deeper at $x/L=1$. Since the first cloud is mainly affected by the turbulence model, improvements may be needed in this regard. For the second cloud at $x/L=0.5$, the model overpredicts the void fraction near the surface by a factor of approximately 20. The result at $x/L=1$ shows good match with experimental data. It is observed in experiment that there is a peak of void fraction from $4\,\text{cm}$ to $10\,\text{cm}$ in depth (Tavakolinejad 2010). This feature is also well predicted by the simulation as shown in the figure, although it is not noticeable for the first cloud at $x/L=0.5$.

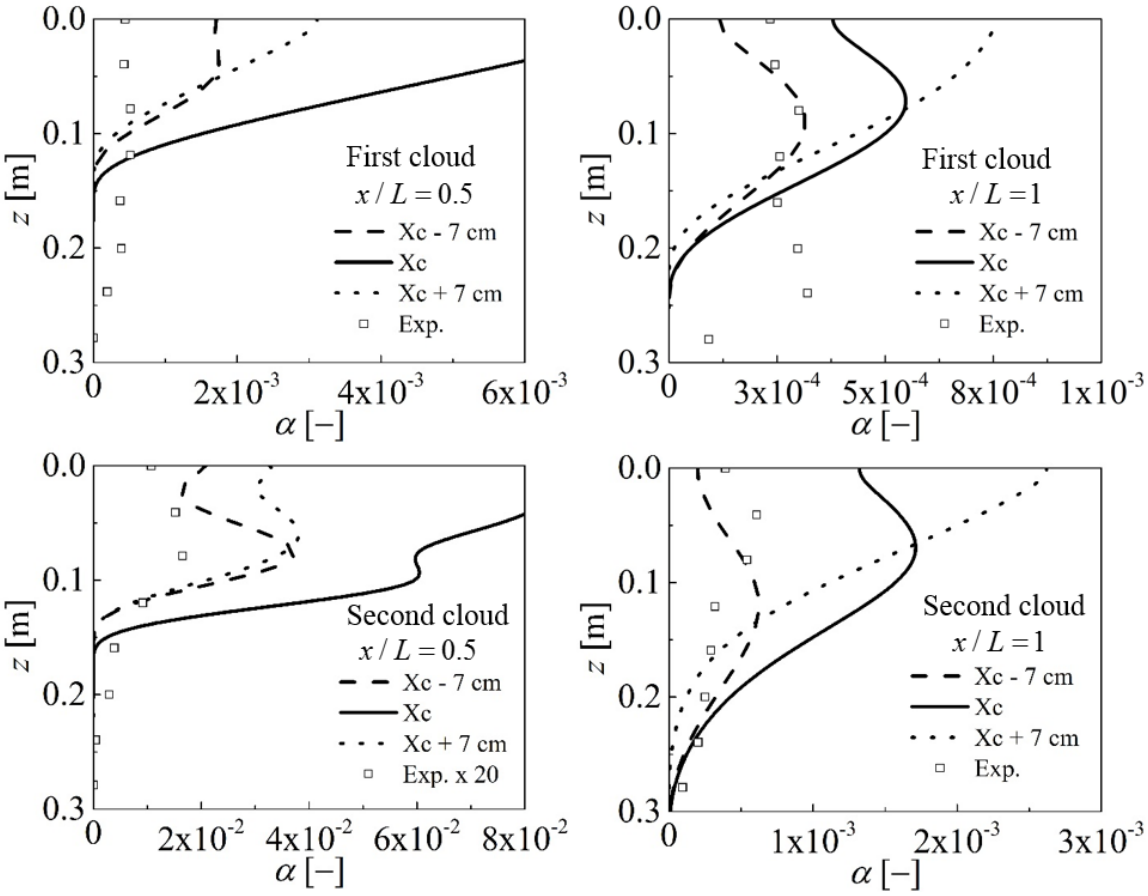

Figure 5.14: Void fraction profiles versus depth for first (top) and second (bottom) clouds. Xc is the x position of the middle line extracted in the cloud.

5.2 Model application to US Navy Athena R/V

The ultimate goal of the entrainment model is to predict bubble entrainment around ships. The near field bubbly flow has important effects to the acoustic signature, therefore it is crucial to evaluate the performance of the entrainment model around relevant ships. Athena R/V is a US Navy research vessel with appendages such as skeg, stabilizers, and masker system. Experimental data, though not considerable, is available to quantitatively validate the entrainment model.

This section applies the entrainment model developed in this work in a full scale simulation of Athena R/V. In Section 5.2.1, the simulation setup will be discussed in detail. A grid convergence study for the model is presented in Section 5.2.2. Finally, the analysis of the bubbly flow around Athena R/V is presented in Section 5.2.3.

5.2.1 Simulation conditions for Athena R/V

As shown in Figure 5.15, the CFD geometry includes all the appendages except propellers. Symmetry about the centerplane is considered to reduce grid size and computational cost. The ship is mirrored for a better visualization in Figure 5.15. To save computational time, the propeller is replaced by a body force model using the load distribution from Hough and Ordway (1964), allowing larger time steps and the use of a static overset grid system. In addition, the grid system is more complicated and elaborate when using discretized propellers (Carrica et al. 2010a). The focus of this simulation is to evaluate the entrainment model occurring near the free surface far from propellers, and thus there is no need to fully discretize the propeller geometry.

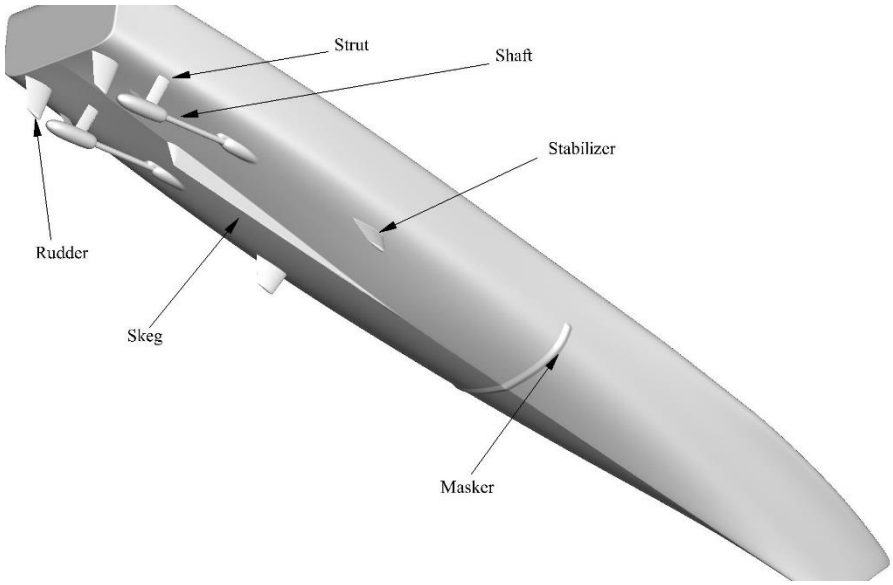

Figure 5.15: Geometry of Athena R/V with appedages.

The complex geometry for Athena R/V requires careful design of the grid system to properly resolve the flow around the ship. The overset grid system is shown in Figure 5.16 and Figure 5.17. Three levels of refinement are placed to resolve the breaking wave at the bow as required by the entrainment model. Although the grid size is much coarser than that used in the 2D+T simulation of Tavakolenijad (2010) for the breaker in Section 5.1 (approximately 3 times for the very fine grid), it provides a good evaluation of the air entrainment model for a practical grid system for a 3D ship simulation. A refinement is placed near the masker to resolve the entrainment in that area. Refinements at stern are designed to capture the highly turbulent bubbly flow there. A summary of important parameters of the coarse grid is shown in Table 5.4. To achieve a better efficiency a proper load balancing is attained by equally distributing the number of grid points across processors. There are 23 grid blocks in total and the load is split in about $55\mathrm{K}$ grid points per processor. The refinements take around 70% of the total number of grid points. Four grid systems are used in the grid study: Coarse, Medium, Fine, and Very fine (VFine). The refinement ratio in each direction is $\sqrt[3]{2}$, doubling the total number of grid points with each successive refinement. For the four grids, grid sizes are shown in Table 5.5. The grid size

for the block at the bow is much finer than other refinements in order to resolve the breaking wave, with a larger grid size in the downstream direction. As for the boundary along the hull, the first grid point to the ship hull is around $0.11\,\text{mm}$ for the VFine grid. Considering the mean shear stress reported in Castro (2011), it can be estimated that $y^+ \sim 17$ at this first grid point (see Table 5.5 for details of different grids). The impact on the solution by this level of refinement near the wall still needs to be revised given that the two-layer boundary layers models (Esch and Menter, 2003) used in these full scale simulations are only applicable within a given range of y^+.

The length for this ship is $L = 47\,\text{m}$. The simulation is performed at a speed of $U = 5.4\,\text{m/s}$. Based on these two reference scales, the Froude and Reynolds numbers are 0.252 and 2.53×10^8, respectively. To better represent the experimental conditions, is incorporated in the simulation. A regular incoming wave with amplitude is 0.05 m and wave length $35.2\,\text{m}$ is used, mimicking the experimental conditions of Johansen et al. (2010), who performed the tests in the ocean with small amplitude waves. A small time step of $\Delta t = 9.2\times10^{-2}\,\text{s}$ is used to avoid large Courant number for all the grid systems. The simulations are performed on a Cray XC30, Lightning, at the U.S. Air Force Research Laboratory (AFRL) DoD Supercomputing Resource Center.

Second order backward differences in time are used for momentum, and a fourth-order ENO scheme (Shu 1998) is used for convection. A second-order TVD scheme with superbee limiter (Ismail et al. 2010) is used to solve the transport equations of group number densities. As the grid size is not fine enough to resolve the viscous sublayer, the two layer wall function implementation by Bhushan et al. (2009) is used. Dissolution is modeled in the number density (2.3), but is neglected in the total void fraction (3.21). The models of Prince and Blanch (1990) and Lehr et al. (2002) are used to model coalescence and breakup, respectively.

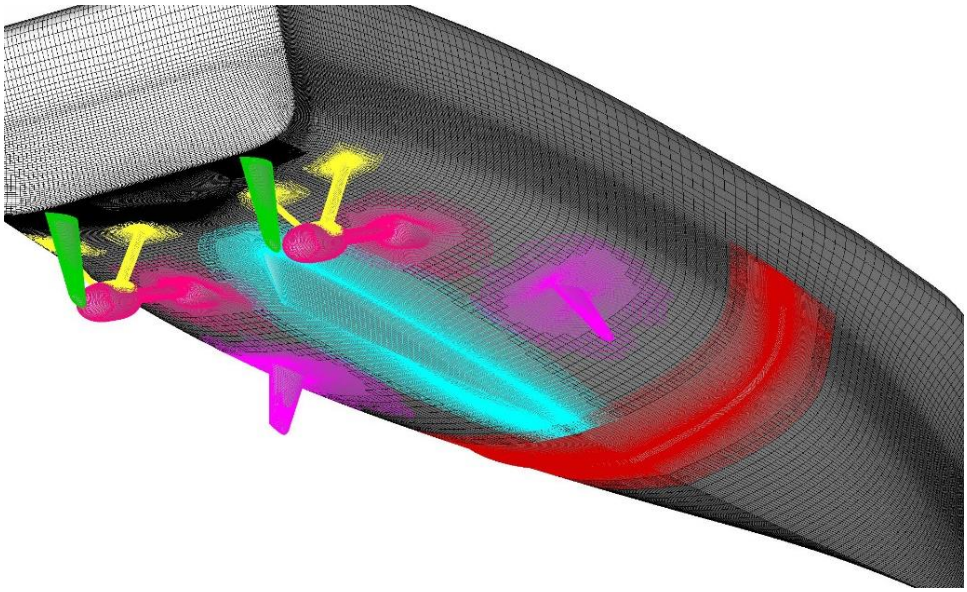

Figure 5.16. Overset grid system for Athena R/V.

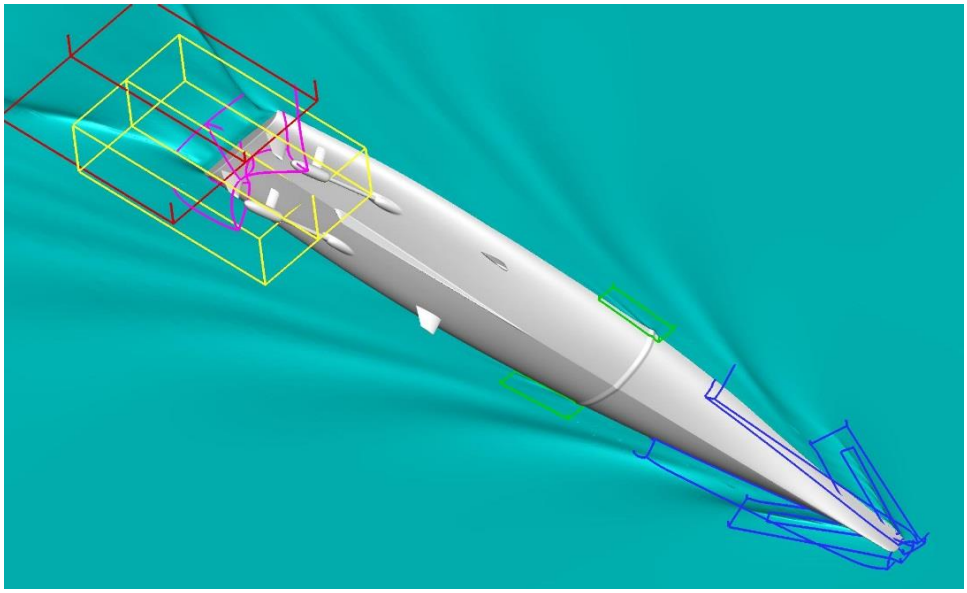

Figure 5.17. Refinements around Athena R/V.

The air entrainment constant is set to $S_{\ell 0} = 0.026$, the same as in Section 5.1. The mixing length turbulence model is also active near the free surface with the same constants obtained from the 2D+T breaking wave case. The simulation is performed for three ship

lengths until a periodic solution driven by the incoming waves is achieved. Two additional wave periods are simulated to perform averages on the solutions.

Table 5.4: Summary of the Coarse grid.

Block Name	**Grid points**	**Processors**	**Grid points/proc**
Hull	1246560	24	56448
Masker	416500	8	54180
Rudder Bottom	102900	2	52920
Rudder Top	208250	4	54180
Rudder Prop	148824	3	50544
Skeg	205800	4	54432
Stabilizer Body	211140	4	54180
Stabilizer Cap	102900	2	52920
Shaft Cap	51450	1	51450
Shaft Propeller	311640	6	54432
Shaft Collar	102900	2	52920
Strut port	205800	4	54432
Strut starboard	205800	4	54432
Background	1244600	24	57024
Rudder Refinement[1]	105056	2	53312
Wake refinement	1038800	20	57960
Bubbly wake refinement	416232	8	56448
Stern refinement	1573040	32	54432
Free surface Refinement	1244600	24	57024
Masker refinement	1573040	32	54432
Bow refinement 1	416500	8	55440
Bow refinement 2	2382032	48	54432
Bow refinement 3	3463800	70	54723

[1] This block is only required for Coarse and Medium grids due to orphans for overset grids.

Table 5.5: Typical grid sizes for grid study.

Grid	**# Points [Million]**	**Grid Spacing [mm]**		
		Bow (dx[1])	Stern	BL (y^+)
Coarse	17.0	4.0 (27.0)	50.0	0.22 (34)
Medium	34.0	3.2 (21.4)	39.7	0.17 (27)
Fine	67.6	2.5 (17.0)	31.5	0.14 (21)
Very fine	135.8	2.0 (13.5)	25.0	0.11 (17)

5.2.2 Grid study for air entrainment model

Most of the air entrainment models reported in the literature are tested with only one grid (Ma et al. 2010a, Shi et al. 2010), and evidence suggests that there are significant changes in entrainment for different grid sizes (M. Hyman, personal communication). Besides that the model constants may vary significantly for different problems (Ma et al. 2010b, Ma et al. 2011b). In addition to model validation with experiments, the independence of the model to grid size changes is important for practical applications. In this work, the grid convergence of the numerical solutions is assessed at several positions where data is available from Johansen et al. (2010).

5.2.2.1 Void fraction contours

Since the experimental data are averaged in time, results are averaged over two wave periods and shown in Figure 5.18. The black dots inside the figure indicate the positions where solutions are extracted at different depths to compare with experimental data. The bubbles entrained at the breaking bow wave region are transported along the ship and finally mix with the bubbly flow at the stern. The Kelvin waves are captured more clearly as the grid is refined. Qualitatively, the mean void fraction at the stern seems to converge in grid, but quantitative comparisons are provided in the following sections. The

[1] dx denotes the grid size in the mainstream direction.

bow insets on the left show details of the void fraction contours and exhibit grid convergence of the solution in this region.

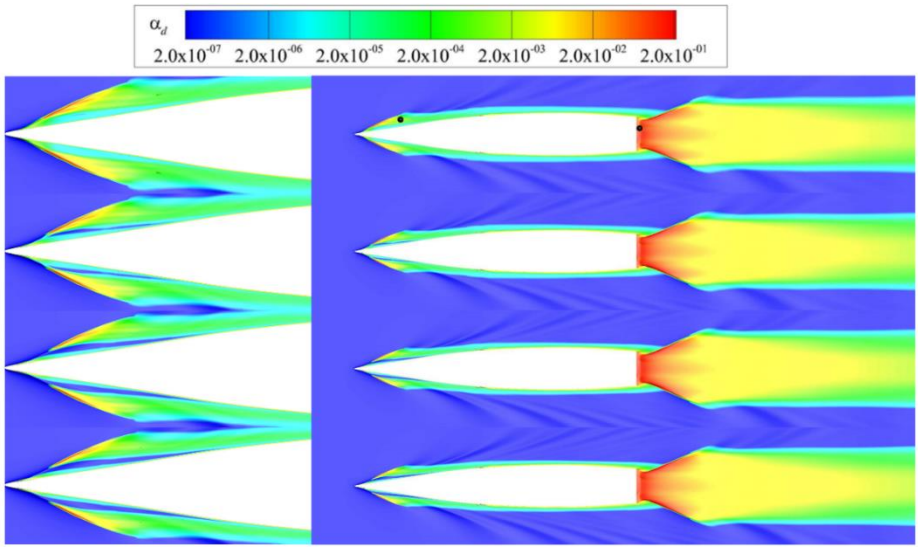

Figure 5.18: Free surface colored with void fraction contours around Athena R/V predicted by the model. From top to bottom: Coarse, Medium, Fine, VFine.

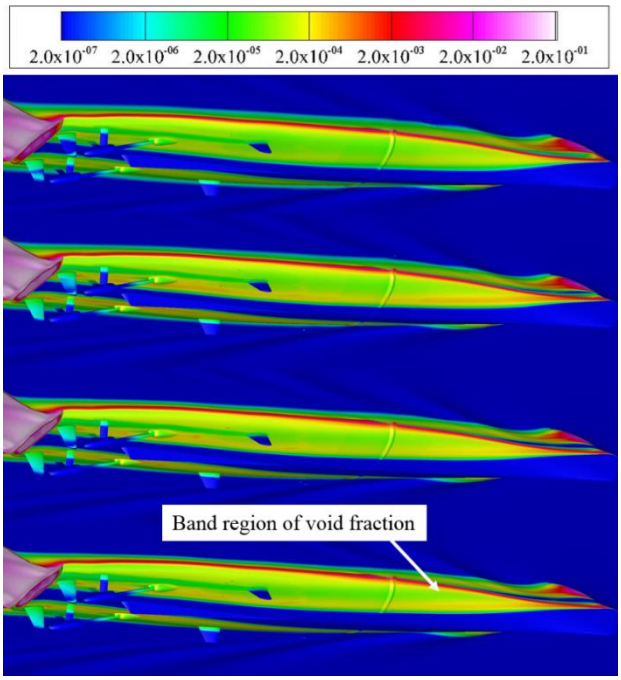

Figure 5.19: Void fraction contours on the hull of Athena R/V. From top to bottom: Coarse, Medium, Fine, VFine.

Figure 5.19 shows void fraction contours on the ship hull under the free surface. Bubbles are entrained at the bow and are swept down underneath the ship by convective and diffusive transport. These bubbles form a band region and go through the shaft and the propellers. The void fraction for the band region is higher than other parts on the hull. Overall, the void fraction contours on the hull show qualitative convergence since no major difference can be observed between Fine and VFine grids.

5.2.2.2 Void fraction profiles

Void fraction profiles with depth at the bow are shown in Figure 5.20 along with experimental data. Although grid convergence is not obvious, the difference among the four grids is not significant considering how sensitive the breakers are to small changes in turbulence levels. The exact vertical position of the probe in the experiment was difficult to determine given that the ship was experiencing roll, pitch and yaw motions. Considering these difficulties, the simulation results are sampled at $(x, y) = (0.158, 0.052)$, at about 3.5 meters downstream the second cloud. As shown in Figure 5.20, the void fraction is underpredicted about one order of magnitude in comparison with experimental data. Johansen et al. (2010) filter their raw data by only counting bubbles when the probe is in water and therefore the time the probe is in the air phase is not counted as an additional void fraction. This, however, is acknowledged by the authors as a significant source of error in the experiment that can lead to considerable overprediction of the void fraction since the probe frequently was exposed to air as the ship rolled. It was observed, however, a clear trace of white water right downstream of the breakers and void fraction levels of about 2% and higher are reasonably expected. On the other hand, the void fraction drops to zero faster than experimental data in depth as also found with the 2D+T breaker.

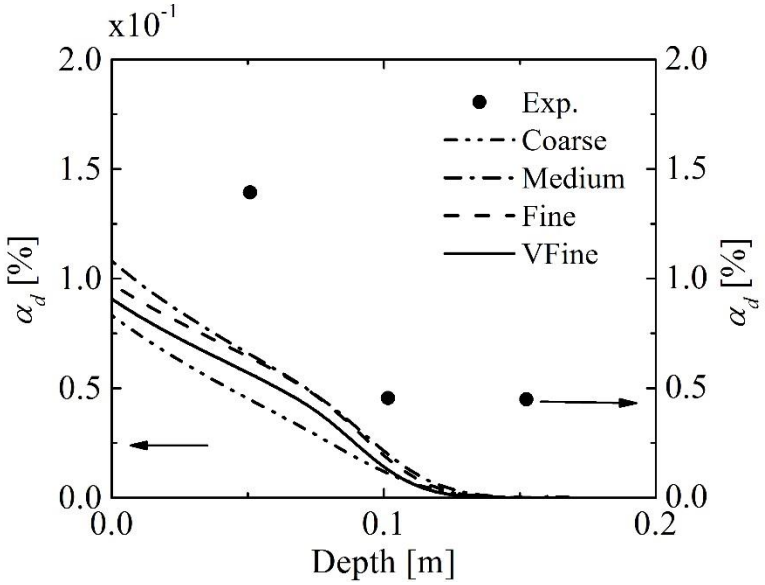

Figure 5.20: Void fraction versus depth at bow expermental position for different grids.

Void fraction variations in depth at the stern are shown in Figure 5.21. The void fraction at the free surface monotonically increases as the grid is refined but it unexpectedly decreases for the VFine grid. Deeper than 0.4 m, the solution shows good grid convergence as observed in Figure 5.21(b) with logarithmic scale. The reason for the void fraction behavior near surface is that the turbulence variables, critical for the bubble entrainment model, do not converge in grid for the VFine grid as shown in Figure 5.22. Both turbulent kinetic energy and dissipation are found to decrease respect to the values in the Fine grid. In addition, higher frequency fluctuations than those from the incoming wave develop as the grid is refined (see Figure 5.22). It is unknown whether the fluctuations resolved in the VFine grid decrease the source from the mean flow and result in lower turbulence levels. Another possible source of error is the wall function, since the first grid point to the wall is $y^+ \sim 17$ for the VFine grid, a distance that may not be appropriate for the two layer wall function model. Inappropriate turbulence levels from the bottom boundary layer of the hull can directly affect the turbulence flow at stern. More work is needed to understand the behavior of turbulence quantities in the stern region as the grid is refined.

The location for the experimental position at the stern is $(x, y) = (1.0106, 0.021)$ (Johansen et al. 2010). Although the experimental data from Terril and Fu (2008) is taken at the centerline, 0.2 meters aft of Johansen et al. probe location, and no filtering was performed to account for when the probe is in air, it is included here for completeness and because of the scarcity of experimental results.

Generally, good agreement is found between the predicted profiles and the experiments even for the coarse grid. Based on this result it is concluded that the air entrainment model is a good predictive tool for a highly turbulent free surface flow as is the case for the stern of a ship at low Froude number. Figure 5.21(b) highlights the transition region in void fraction at the bottom of transom. Bubbles are pushed away by the incoming high speed boundary layer flow under the ship as they reach the bottom of the transom's depth. However, the experiments show higher void fraction levels than in the simulation below this depth. Possible reasons can be: 1. The turbulent dispersion and interaction with the hull are underpredicted, So bubbles cannot be pulled down deep enough by turbulent mixing. The same trend is observed for Kann boat. 2. Bubbles coming from underneath the ship are underpredicted by the model.

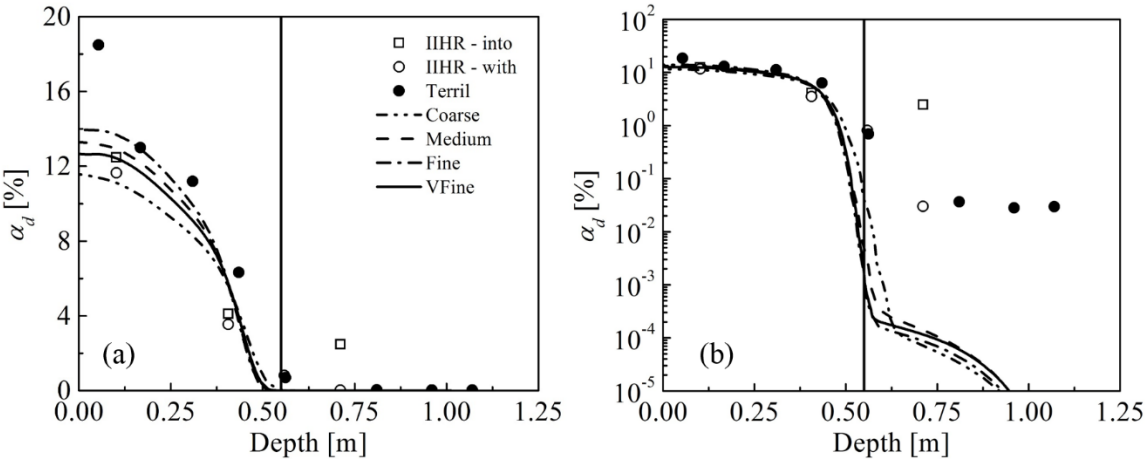

Figure 5.21: Void fraction versus depth at the stern for different grids at the experimental position. (a): linear scale; (b): logrithmic scale. Black vertical line indicates the depth of the bottom of transom.

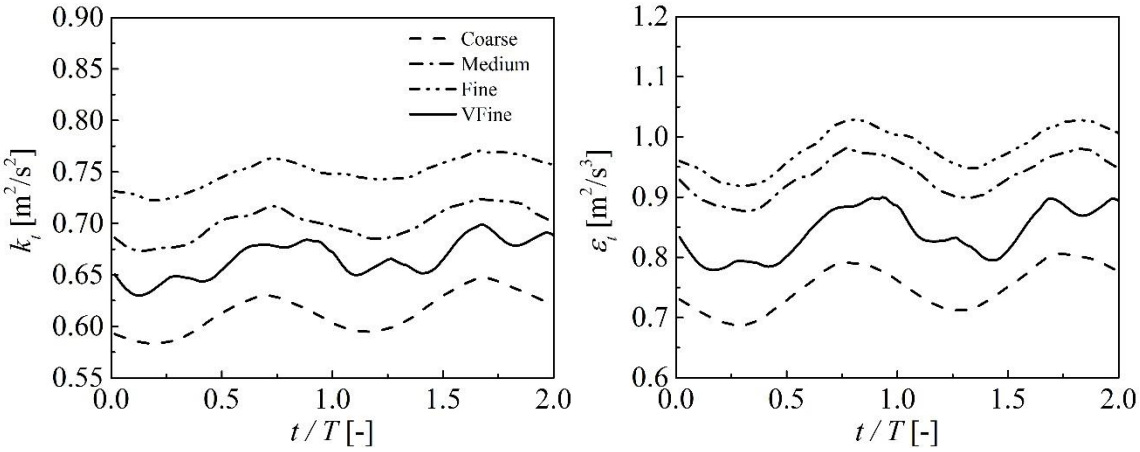

Figure 5.22: Turbulent kinetic energy and dissipation variations in two wave periods for VFine grid at z =-0.007 at experimental loaction (around 0.05 m from the averaged free surface). T is the incoming wave period.

5.2.2.3 Bubble size distribution

Normalized bubble size distribution for several depths at the stern are reported in Figure 5.23. The bubble groups reported in the experiment are different from those chosen for the numerical simulation, thus the numerical results are integrated over the experimental groups for comparison. The group size information can be found in Johansen et al. (2010). The experimental data shown in Figure 5.23 was taken at 9 knots, while simulations were performed at 10.5 knots. It is assumed that the size distribution does not vary significantly when increasing the speed to 10.5 knots.

At 0.1 m the profiles for the four grids are practically indistinguishable from each other as a result of the entrainment source being the dominating term at this depth. The profiles show convergence at depths of 0.3 m and 0.5 m. However, a significant difference among grids at 0.6 m is observed, where the transition region at the bottom of transom occurs (Figure 5.21). Although the Coarse grid predicts large bubbles dominating in the void fraction, small bubbles become the main contribution as the grid is refined. The reason for such large difference is the difficulty to predict the sharp transition with the coarse grid, numerical diffusion can strongly affect the size distribution around the region. As the depth

increases further, the profiles show good grid convergence. While the void fraction near the free surface does not converge well as the grids are refined, the normalized group void fraction shows great grid convergence trends.

Overall, two peaks can be observed in the profiles at all depths. These peaks are not always predicted by the numerical simulation. For the depth at 0.1 m, the experimental data shows a small peak at $R = 80\,\mu\text{m}$, which is not predicted by the two phase model. This peak is also seen at all other depths in the experiments suggesting that a fraction of these bubbles might come from the ship's boundary layer. Another fraction can be entrained form the surface by droplet impact, a process important in the highly energetic stern flow and ignored at this point in the entrainment model, or the product of breakup from large bubbles. The experimental data at 0.3 m shows a slight drop in value for largest group due to high terminal velocity, which is also predicted by the simulation. The experimental data suggests a peak at $R = 2\,\text{mm}$, underpredicted slightly by the simulations. At 0.6 m, the numerical simulation predicts a peak at around $R = 80\,\mu\text{m}$, present in the experimental data, and repeated for depths 0.6 m, 0.65 m and 0.7 m. The transition region (between 0.5 m and 0.6 m) predicted by the simulation is narrower than that for the experimental data (between 0.5 m to 0.7 m).

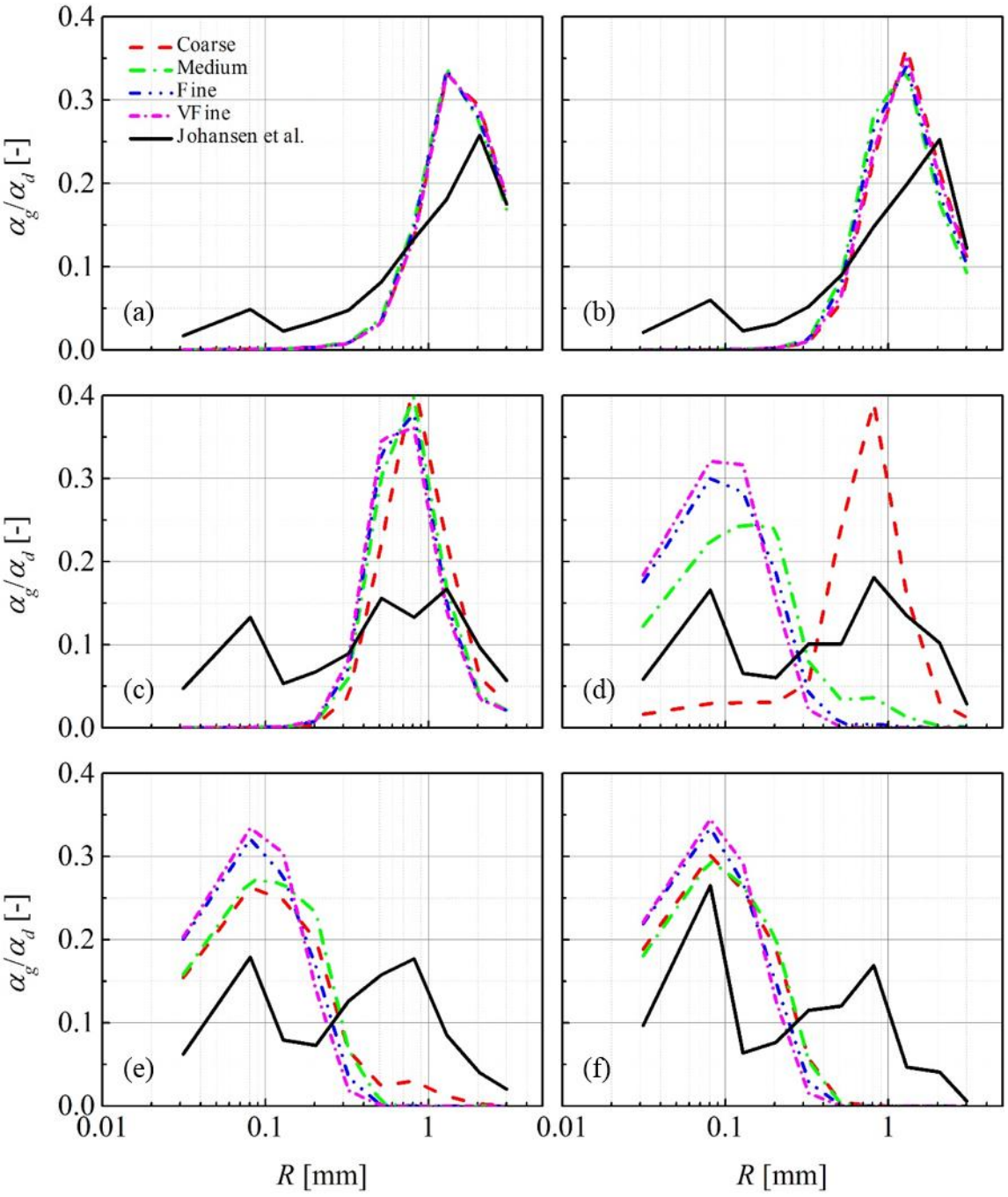

Figure 5.23: Normalized void fraction for experimental groups at different depths. The order (a) to (f) indicates 0.1 m, 0.3 m, 0.5 m, 0.6 m, 0.65 m, 0.7 m in depth.

The Sauter diameter d_{32} and mean diameter d_{10} at the same stern location are shown in Figure 5.24, displaying a satisfactory grid convergence. The Sauter diameter predicted at the free surface is around 2.6 mm and slowly decreases to 1 mm at about 0.5

m deep. A narrow transition region between 0.5 m and 0.6 m can be observed for the finer grids. This transition in d_{32} was already hinted by Figure 5.23. Both d_{32} and d_{10} show good convergence below 0.6 m in agreement with the results in Figure 5.23. As for the mean diameter, the profile increases until a peak occurs at around 0.46 m. The mean diameter (Castro 2011) is the zero-th moment of $D\,f(D)$ ($f(D)$ is normalized by the total number of bubbles). As can be seen in Figure 5.25 for the normalized $D\,f(D)$, a peak is observed for large bubbles around 1 mm for depths near 0.4 m in accordance to the peak in mean diameter observed in Figure 5.24.

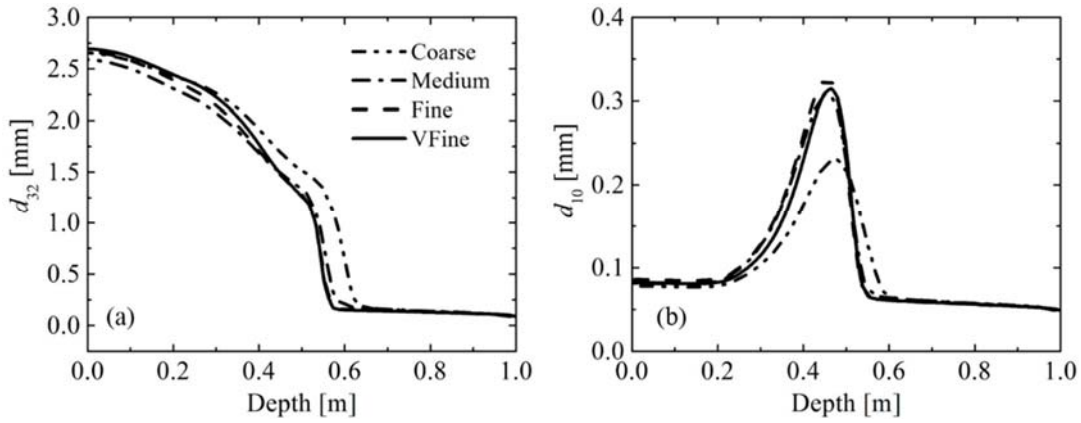

Figure 5.24: Sauter diameter and mean diameter vs. depth for different grids.

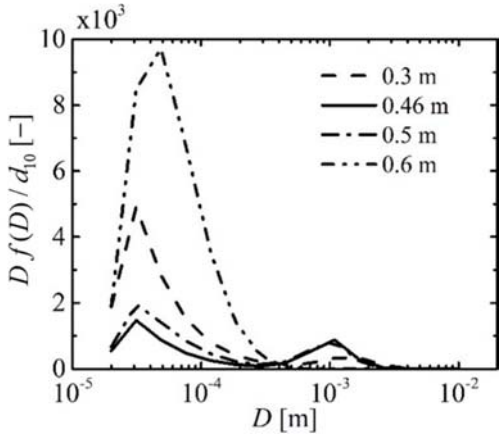

Figure 5.25: Normalized $D\,f(D)$ for diferent depths at the stern experimental location for Fine grid.

5.2.3 Flow features

This section presents a detailed analysis of the main flow features of the bubbly flow around Athena R/V. Solution from the fine grid is used to this end.

5.2.3.1 Entrainment source predicted by the model

The entrainment source around Athena is shown in Figure 5.26 with logarithmically distributed contour levels. Three key regions are observed with high entrainment source, the stern, the bow wave breaking are, and the hull/free surface contact line, as expected from experimental observations of bubble locations. Although the area for entrainment at the stern is broad due to the strong turbulent flow, the strength decreases rapidly away from the ship. The source remains active deeper at the center than in the shoulder waves. The wave breaking results in strong entrainment. At the contact line the source remains active in a very narrow region close to the free surface as a result of the small turbulent scales that drive the process. In addition, the entrainment source has a larger entrainment region at the masker compared with neighboring areas. It has to be pointed out that breaking at the masker as observed in the experiment is a very violent process resulting in a very fragmented free surface and sprays that are not resolved by the grids used herein.

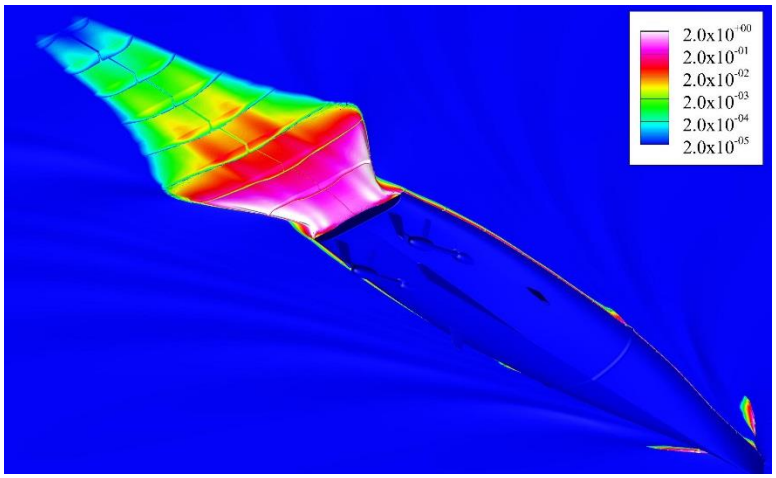

Figure 5.26: Entrainment source of void fraction around Athena R/V predicted by the model. Slices and free surface are colored with entrainment source of void fraction.

A detailed view of the bow breaker is shown in Figure 5.27. The entrainment source is active along the bow wave breaker and has a large value at the impact region as previously observed for the 2D+T breaker. Additionally, a region of high entrainment source attached to the hull where the breaker begins to develop is observed. The entrainment strength there is significantly affected by the incoming wave, resulting in pulsating bubble clouds with a frequency given by the wave encounter frequency. Even though there are bubbles in the entire boundary layer for the hull/free surface contact line, air entertainment source may not be active there. As shown in Figure 5.28, the integral length scale in boundary layer near surface can be less than 1 cm. As a result, P_z in the entrainment source decreases to zero in an extremely short depth and the probability of entrainment is low. Figure 5.28(a) shows the source is deactivate very close to the wall. Bubbles entrained at places where the integral length scale is larger than the depth can be transported to the wall by turbulent mixing in the boundary layer.

Figure 5.29 shows the instantaneous entrainment source for the bow breaker at $x/L = 0.064$. The impact region is characterized by a large entrainment source while locations around the cavity have less entrainment. Although the jet is different form the jet in the 2D+T simulation in Section 5.1, the source is active at similar places. To make a comparison, several characteristic parameter are chosen in Table 5.6 where the shear strength is chosen when the jet hits the free surface. Overall, the 2D+T breaker is stronger than the 3D breaker, which makes sense since the Froude number is higher. Additionally, it is found that the production contributed by the mixing length model is negligible compared with the production by the TPM+MNL model described in Section 5.1.2. Therefore, the mixing length model does not play such an important role as it did with the 2D+T breaker.

Table 5.6: Comparison between two breakers.

	3D breaker	2D breaker
Height (m)	0.1	0.16
Thickness (m)	0.012	0.016
Shear strength ($\|\mathbf{S}\|$) (1/s)	215	654

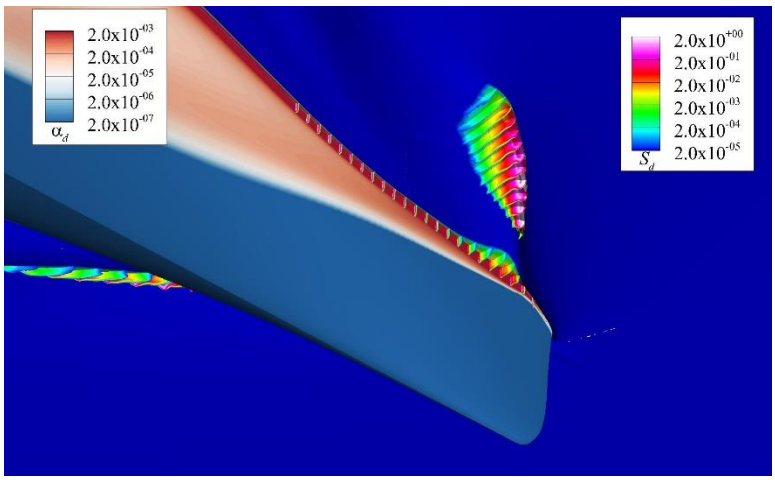

Figure 5.27: Wave breaking at the bow. Hull colored with void fractoin. Free surface colored with entrainment source.

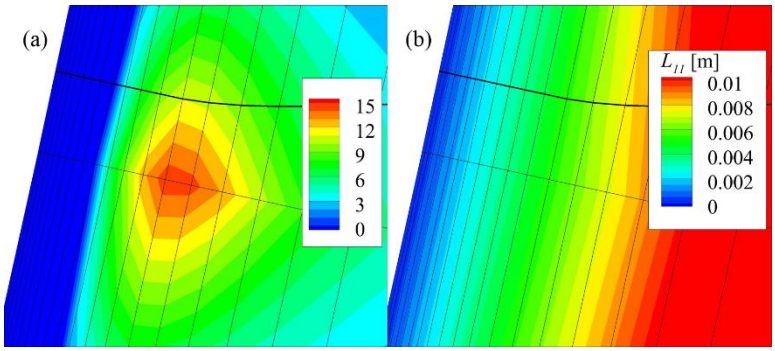

Figure 5.28: Instantaneous solution at $x/L = 0.8$ colored with (a) entrainment source and (b) integral length scale L_{11}.

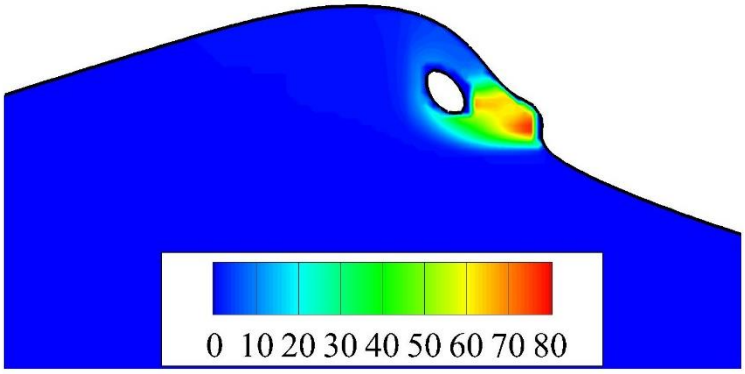

Figure 5.29: Slice $x/L = 0.064$ at bow wave breaking region colored with entrainment source of void fraction.

5.2.3.2 Void fractions around the Athena R/V

Figure 5.30 shows void fraction contours around Athena R/V. Bubbles are observed at the bow wave breaking, hull/free surface contact line, and stern. The masker also causes wave breaking and entrainment as observed in the experiment even though the grid resolution is insufficient to capture it to the full extent. Previous work by Castro (2011) predicts higher void fraction levels at the hull when using RPI's (Ma et al. 2010b) model. However it was observed that RPI's model tends to improperly predict air entrainment in regions of high velocity gradients especially near solid boundaries. This thesis improves on these results in two ways: 1) the air entrainment model is a function of local turbulent quantities and is reasonably grid independent. 2) Bubble transport equations are integrated all the way into the wall in contrast to the work by Castro (2011), which solves for average quantities near a wall region. Bubbles at the bow are transported down by the strong downward velocity field and turbulence mixing, as indicated by the void fraction contours. Slices colored with void fraction in Figure 5.30 show the bubbly boundary layer evolves from the bow to the stern of the ship. The void fraction contours shown on the rudders indicate strong effects of the propeller on the bubble transport.

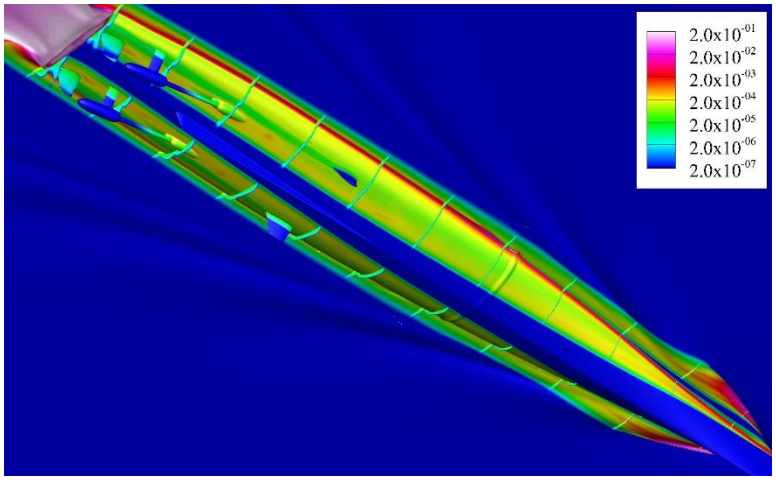

Figure 5.30: Predicted void fraction contours around Athena R/V.

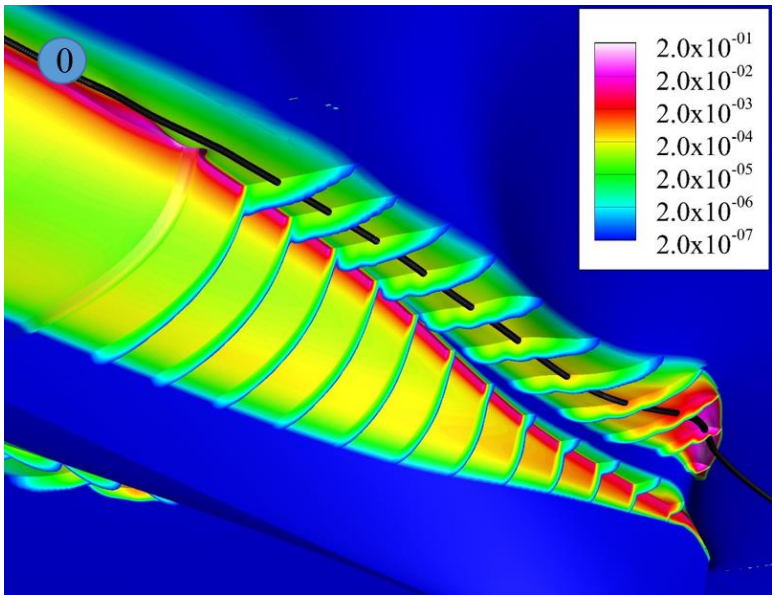

Figure 5.31: Void fraction contours at bow.

Bubble clouds similar to those observed in the 2D+T experiment (Tavakolinejad 2010) are also predicted in the Athena R/V bow wave as shown in Figure 5.31. The clouds downstream of the breaker finally disappear before reaching the masker as bubbles leave the domain due to buoyancy. Bubbles can go deep, depending on bubble size, as they are transported around the ship with the flow, which can be seen from the thickness of the

bubbly layer near the free surface. Bubbles forming the band region shown in Figure 5.19 are transported from the near surface region at bow by the flow (see Figure 5.35 for streamlines).

The streamline in Figure 5.31 goes through the second bubble cloud produced by the breaker. Void fraction along this streamline is presented in Figure 5.32. Two peaks in the profile are marked out by circles. They are caused by the entrainment at bow and stern respectively. The void fraction decreases quickly due to escape of bubbles through the surface but with different rates after entrainment in bow and stern. This difference is mainly caused by differences in turbulence mixing and bubbles sizes. The void fraction does not vary significantly form $x/L=0.4$ to $x/L=1$ because small bubbles, with low terminal velocity, dominate the size distribution in this region.

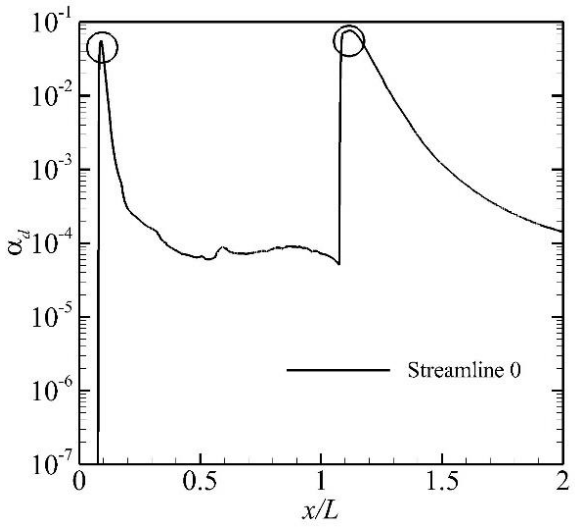

Figure 5.32: Void fraction variation along streamline 0.

As shown in Figure 5.33, the void fraction distribution changes significantly as bubbles move close to the propeller. Upstream of the propeller, bubbles are sucked downward gradually. Since mostly small bubbles are present at this depth, the relative velocity is negligible compared with the liquid velocity. As a result, they are essentially

markers transported along the shaft by the shedding vortices from the shaft collar. Bubbles are pulled deeper when they go through the propeller and finally reach the rudders, producing a wake with a very characteristic cloud signature behind the propellers. The bubbly wake behind the ship is shown in Figure 5.34 with slices colored by void fraction. The void fraction gradually decreases as the wake grows in the spanwise direction due to mixing and bubbles leaving the domain due to buoyancy. In addition, stronger turbulence in the center of the wake, as indicated by the entrainment source in Figure 5.26, results in higher void fraction and mixes bubbles deeper than those on two sides.

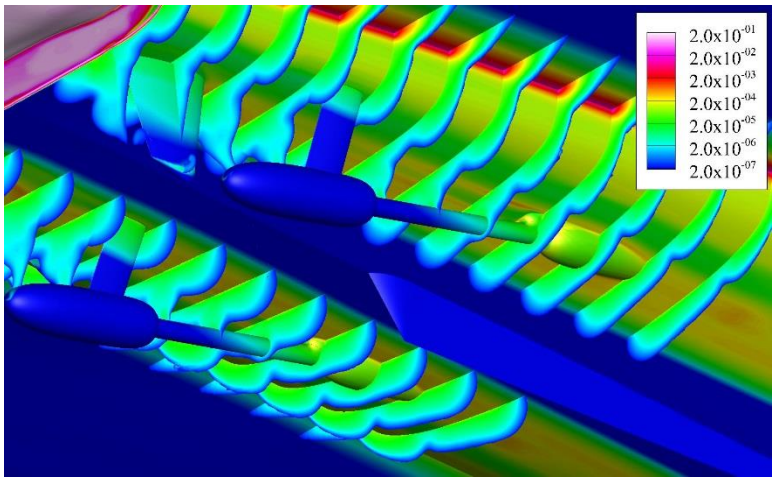

Figure 5.33: Void fraction contours near the propellers.

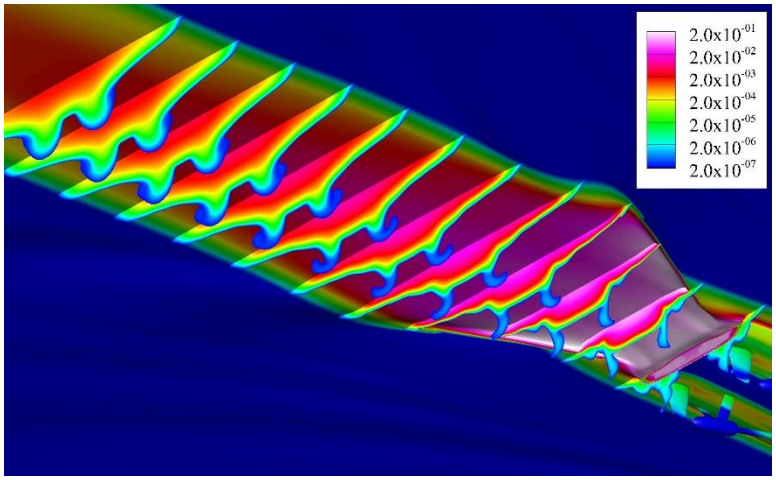

Figure 5.34: Bubbly wake for Athena R/V. Slices and free surface are colored with void fraction.

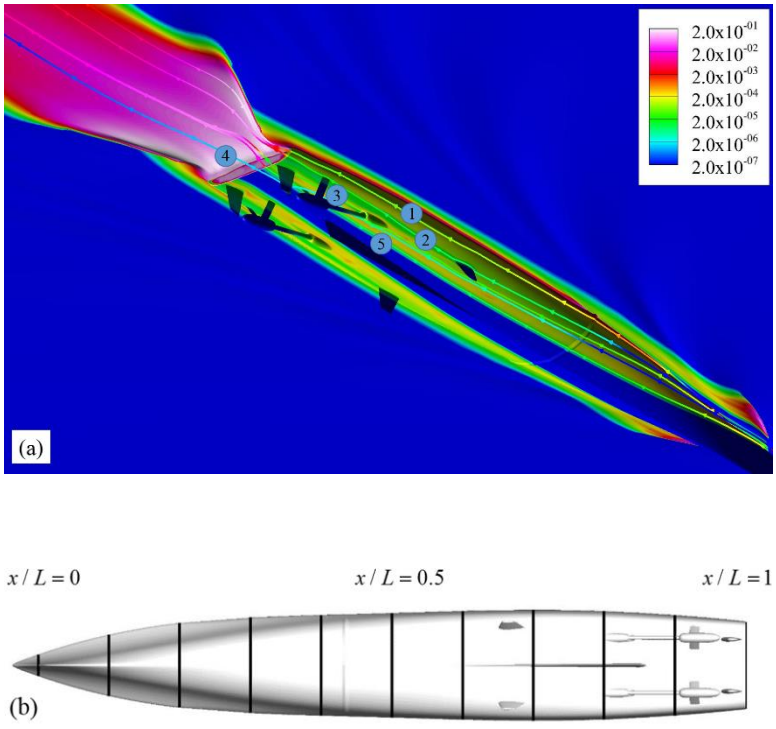

Figure 5.35: (a) Extracted streamlines along Athena R/V (All are colored with void fraction); (b) Definition of positions along hull.

Five streamlines are extracted along the starboard side of the hull, chosen to represent most of the near wall region. They are numbered 1 to 5 from top to bottom in

Figure 5.35(a). Streamline 1 is near the hull/free surface contact line. Streamline 2 is close to the strut and stabilizer. Streamline 3 goes through the two struts, 4 goes through the propeller and 5 covers the deepest regions that bubbles can reach on the hull, close to the skeg and inner strut. In addition, streamlines 3 and 5 are close to the center in the bubbly wake behind the ship, where the depths for all the streamlines except 4 are less than $10\,\mathrm{cm}$. The definition of positions along the ship are shown in Figure 5.35(b).

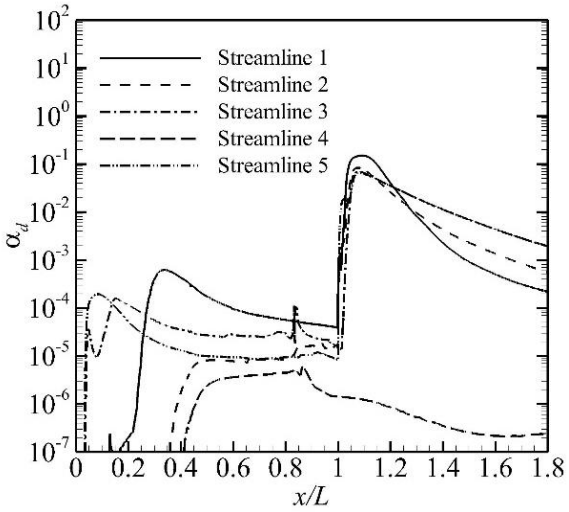

Figure 5.36: Void fraction along streamlines.

Void fraction along the streamlines is shown in Figure 5.36. Increases in void fraction are initially observed when the path gets into bubbly locations. The void fraction then decrease or increase slowly, with values varying from 10^{-4} to 10^{-6} depending on streamline from $x/L = 0.5$ to $x/L = 1$. The void fraction jumps to much higher values at the stern except for streamline 4, which is deeper and not affected by the entrainment at the stern. Downstream of the stern the void fraction decreases quickly due to bubble buoyancy and release through the free surface. The deaeration rates beyond $x/L = 1.4$ are similar for streamlines close to the surface (1, 2, 3 and 5)

Turbulent kinetic energy and dissipation are shown in Figure 5.37. Streamlines 3 and 5 (lines overlap in the figure) go through the highest k_t and ε_t downstream of the ship. The turbulence field not only affects the entrainment source but also the bubble transport, resulting in differences in void fraction and bubble size distribution.

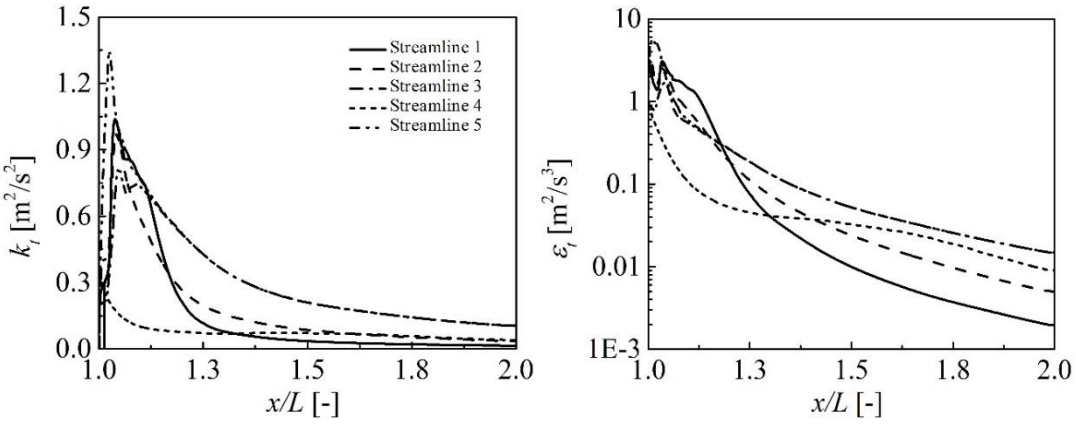

Figure 5.37: Turbulence kitnetic energy and dissipation in the ship's wake.

5.2.3.3 Bubble size distribution along sample streamlines

Normalized void fraction size distributions along streamline 0 are shown in Figure 5.38. The distribution for the entrainment source is also shown, which peaks at 4 mm in diameter. Large bubbles rise quickly after entrainment as indicated by the shifts toward smaller bubbles for different downstream positions in Figure 5.38(a). At $x/L = 0.1$, close to the breaker, the peak value occurs at $D = 2\,\text{mm}$, half of the value for entrainment source, and drops to 300 μm in a distance of 1.4 m along the streamline. From $x/L = 0.2$ to $x/L = 0.4$ the peak diameter decreases from around $200\,\mu\text{m}$ to $100\,\mu\text{m}$. Beyond $x/L = 0.4$, the bubble size distribution does not show significant variations. Considering Figure 5.32 and Figure 5.38, we conclude that large bubbles entrained at wave breaking region escape quickly through the free surface resulting in a rapid drop in void fraction as the remaining small bubbles dominate the bubble size distribution, leading to lower decrease rates in void fraction.

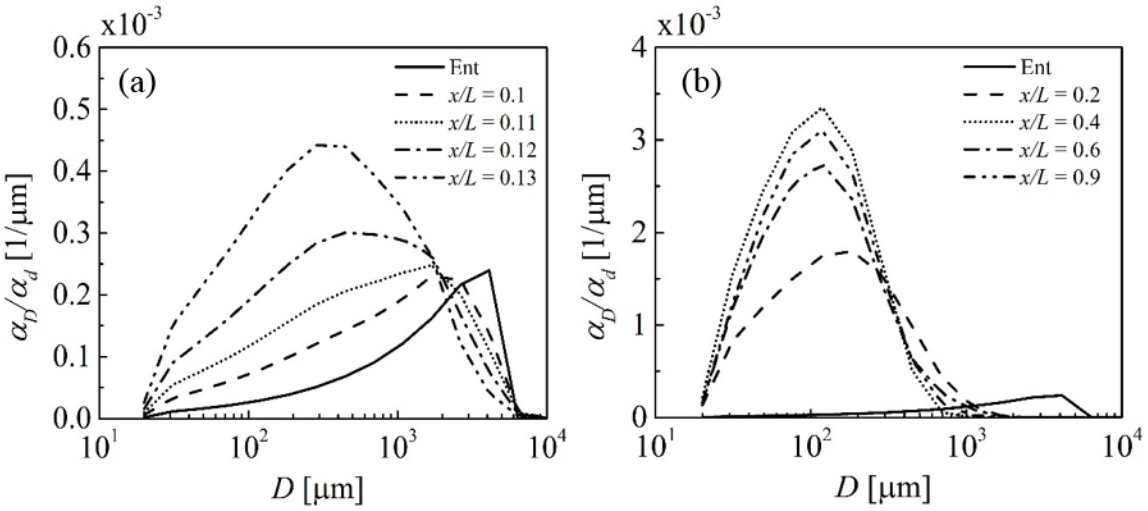

Figure 5.38: Normalized void fraction size distribution at different positions along streamline 0.

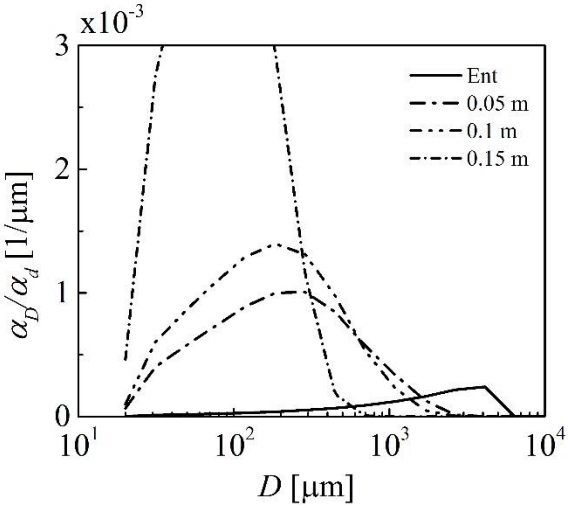

Figure 5.39: Normalized void fraction size distribution at different depths for the bow experimental position.

Figure 5.39 presents the normalized void fraction size distribution at different depths for the bow experimental position in Johansen et al. (2010), 3.5 m downstream of the breaker. As expected, the size distribution peak shifts to smaller bubbles as the depth increases. The size distribution peaks around 80 μm at 0.15 m, coincident with the

distributions shown in Figure 5.23. The size distribution does not change considerably from 0.05 m to 0.1 m in depth while it varies substantially from 0.1 m to 0.15 m.

The Sauter diameter for different streamlines is shown in Figure 5.40. From $x/L=0.4$ to $x/L=1$, the Sauter diameter is small at $d_{32}\sim 170\,\mu\text{m}$ ($270\,\mu\text{m}$ for streamline 3), concluding that the size distribution quickly develops along the hull. The strong entrainment at the stern causes sharp increases of the Sauter diameter near the free surface, reaching values of $d_{32}\sim 2350\,\mu\text{m}$. The Sauter diameter decreases quickly downstream mainly as a result of large bubbles leaving the domain, with the exception of streamline 4.

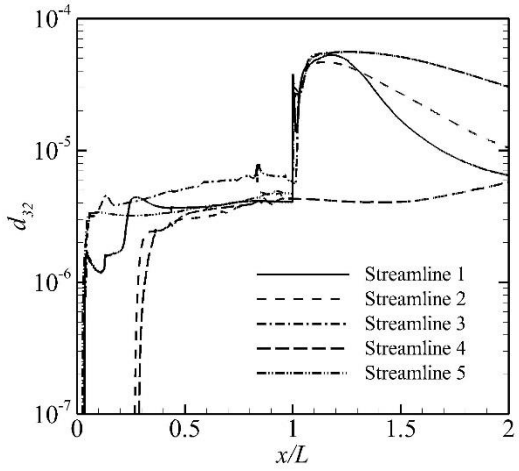

Figure 5.40: Predicted Sauter diameter d_{32} variation along streamlines.

The number density of three groups (groups 1, 8 and 15) are shown in Figure 5.41. The evolution along the streamlines for groups 1 and 8 groups are considerably similar downstream of the ship, with both decreasing slowly away from the ship. For bubbles with $D=0.45\,\text{mm}$ (group 8), the number density stays almost constant from $x/L=0.5$ to $x/L=1$. Few bubbles with $D=1\text{cm}$ can be found under the ship, and though they are entrained massively at the stern, large bubbles leave the fluid rapidly downstream of the

ship. Since these streamlines go through regions with different turbulence levels (see Figure 5.37), dispersion, coalescence and breakup rates differ for different streamlines.

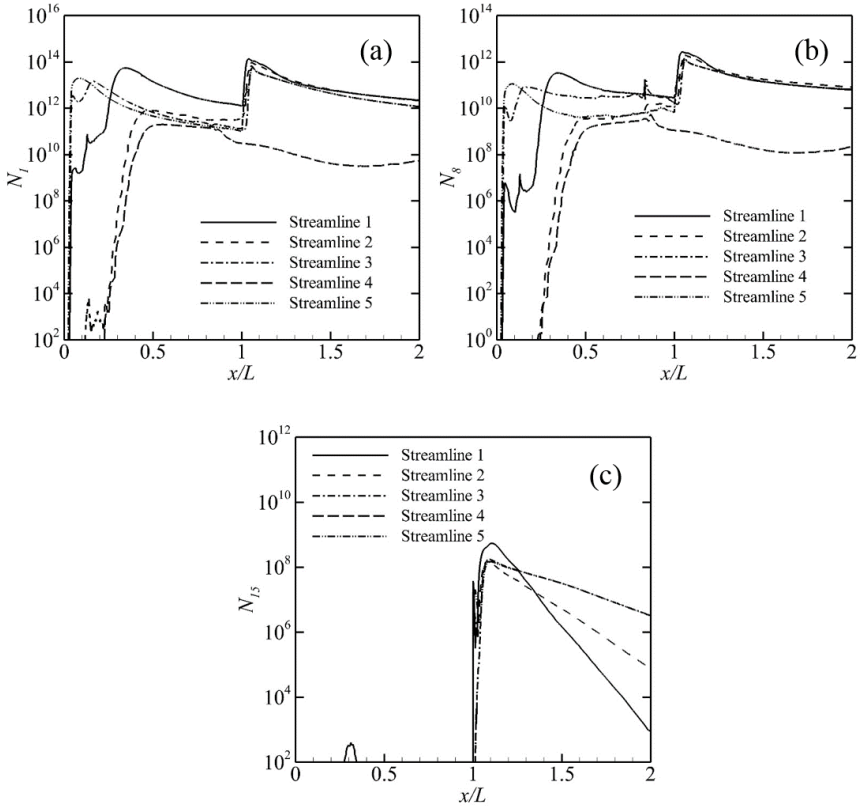

Figure 5.41: Group number density along the hull for different streamlines. (a): No. 1 group with $D = 20\,\mu\text{m}$;(b): No. 8 group with $D = 0.45\,\text{mm}$; (c): No. 15 group with $D = 1\,\text{cm}$.

Figure 5.42 presents the normalized void fraction size distribution along streamlines. Recall that the streamline may go through different depths, which can affect the size distribution, see Figure 5.39. For $x/L < 1$, most bubbles along all streamlines are smaller than 500 μm. For streamlines 1 and 2 the size distribution in the wake shifts gradually to smaller bubbles. Streamlines 3 and 5, however, experience high turbulence levels (see Figure 5.37) that produce entrainment resulting in size distributions similar to the entrainment size distribution.

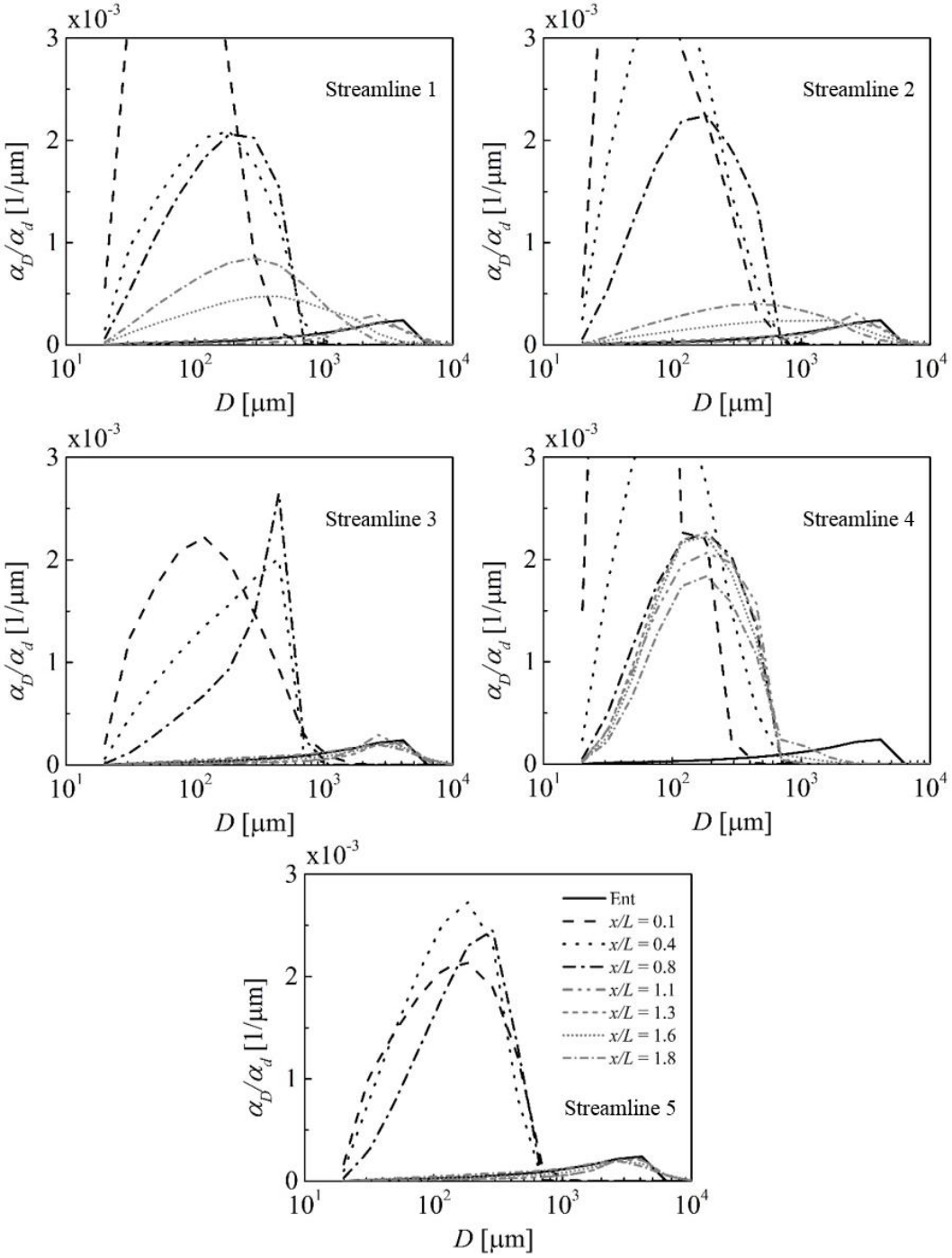

Figure 5.42: Normalized void fraction distributions at different positions along the five extracted streamlines.

5.3 Model application for Kann boat

Bubble transport around ships can be significantly different depending on the geometry characteristic of ship. This section presents two phase simulation of Kann boat using the proposed numerical scheme, with turbulent entrainment and impact entrainment model. Also, extensive experimental data is available from Perret et al. (2014) to make a comparison.

For this case, the waterline length is $L = 6\,\mathrm{m}$ and the boat speed is $U = 9.26\,\mathrm{m/s}$, resulting in $\mathrm{Re} = 5.67\times10^{7}$ and $\mathrm{Fr} = 1.21$. Half of the ship is simulated, taking advantage of the centerplane symmetry of the geometry. The grid system has 7 blocks with 10.3 million grid nodes in total as shown in Figure 5.43. Two refinements are placed at the bow to properly capture wave breaking and entrainment.

The two phase blended $k-\varepsilon/k-\omega$ SST turbulence model (Moraga et al. 2008) with MNL+ML method in Section 5.1 is used in the simulation. The liquid momentum equation is solved with second order discretization in time and fourth order in space. The time step is $\Delta t = 6.5\times10^{-4}\,\mathrm{s}$. The boat is free to heave with the trim fixed at 2.3°, as measured in experiments. Bubble sizes are discretized in 15 groups in the range $D \in (20\,\mu\mathrm{m}, 2\,\mathrm{cm})$ equally spaced on a logarithmic scale. The models of Prince and Blanch (1990) and Lehr et al. (2002) are used to model coalescence and breakup, respectively. Bubble dissolution is also modeled as in (Castro and Carrica 2013a) though it could be neglected in this case given the short time scales considered. Impact entrainment model parameters are: $d_e = 0.025\,\mathrm{m}$, $d_{\mathrm{w}} = 0.05\,\mathrm{m}$, $\delta_{FS} = 0.05\,\mathrm{m}$. The modeling strength constant is $C(\lambda) = 0.15$. Entrainment size distribution taken from the bow experimental data (Johansen et al 2010) is used to obtain the entrainment source for each group. Other modeling constants are the same as in Athena R/V case. The simulation is performed without two phase model for 3 ship lengths and then continues with two phase model until the flow finally reach a quasi-steady status. The solution for the following analysis is obtained at $t = 6$.

Grid	Nodes
Hull	241×51×201
Bow	51×51×61
Bilge keel	201×51×61
Stern	61×51×51
Refinement_curv	121×91×185
Refinement_cube	151×171×117
Background	181×101×101
Total	10.3M

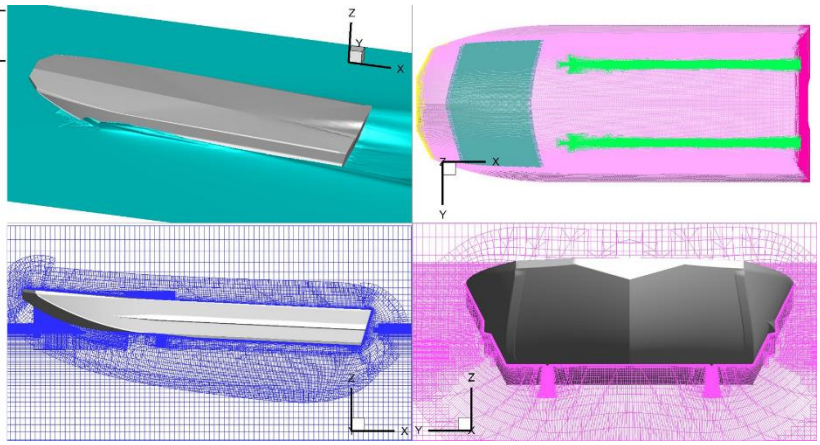

Figure 5.43: Overset grid system for Kann boat.

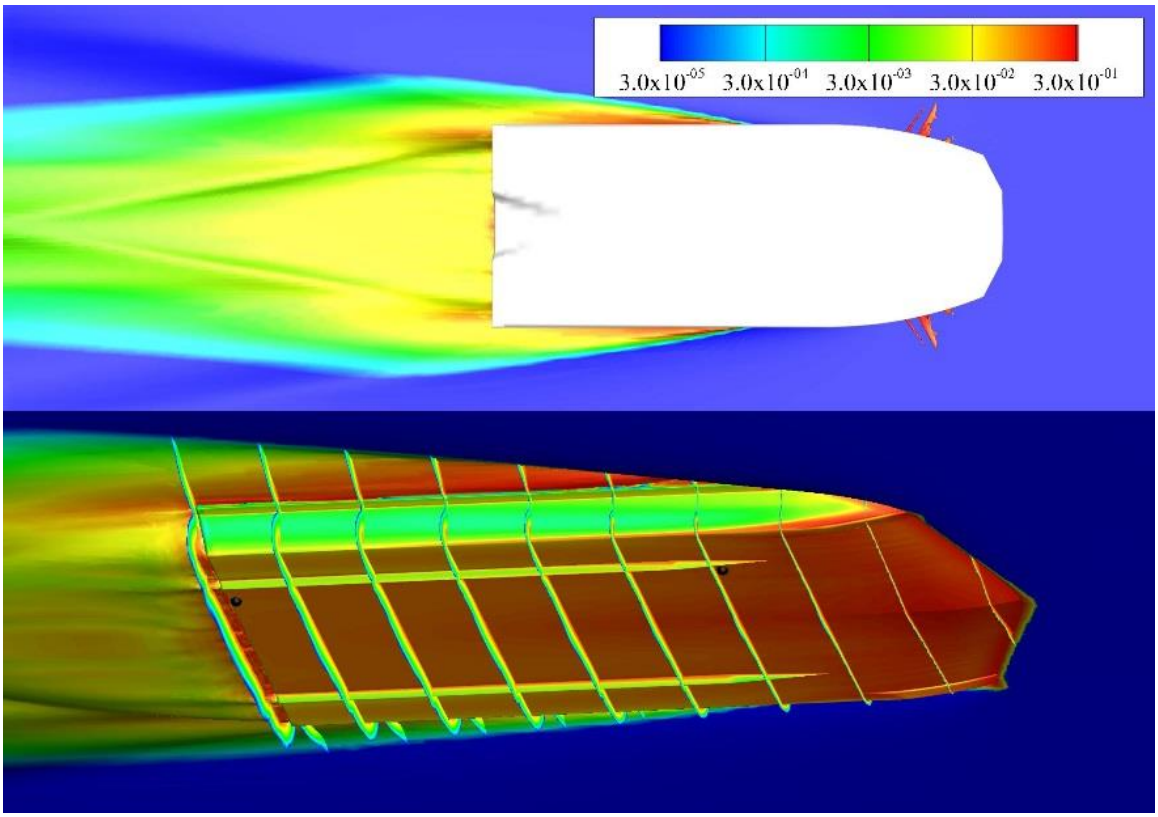

Figure 5.44: Free surface and hull colored with void fraction.

Free surface colored with total void fraction is shown in Figure 5.44 at $t = 6$, when the bubbly flow is fully developed behind the boat. The experimental locations are marked out as black points. The top view shows the bubbly wake behind boat. High void fraction

are observed near transom. It has to be mentioned that results from increasing mixing length model constant are different at the bow, which have splashes plunging into water forming bubble trails on two sides (Li et al. 2015). Slices colored with void fraction in a view from the bottom in Figure 5.44 follow the evolution of the boundary layer as its thickness grows from the bow to the stern, revealing that a large amount of the bubbles in the wake behind the boat comes from the boundary layer bubbles generated at the bow. The contour levels of void fraction at the hull show a fairly uniform two-phase flow underneath the boat with no significant secondary flows that might disturb the experimental conditions.

Figure 5.45 compares profiles of void fraction against distance to the hull at the bow and the stern at the experimental locations reported by Perret et al. (2014). The experiments reveal a fairly uniform profile at the bow most likely due to the very intense mixing taking place at this location near the entrainment region. The void fraction increases at the stern location as bubbles rise up towards the hull. The computational model is able to reproduce levels of void fraction similar to those in the experiments and even the shrinking of the boundary layer towards the stern. However a better match requires the development of breakup and coalescence models for the extreme conditions of shear and turbulence within a full-scale boundary layer. The result from Li et al. (2015) is also shown in Figure 5.45. The major difference is the void fraction level away from hull at bow. It is due to the high turbulence level introduced by the mixing length model that the void fraction reaches zero slowly. Although the void fractions differ for two models, the normalized void fraction distribution and bubble number density are very similar at experimental locations.

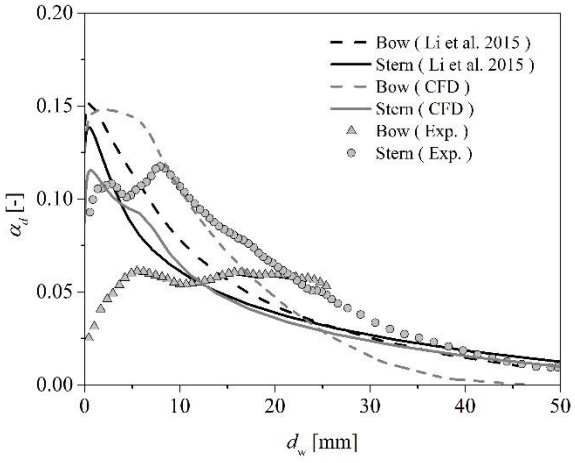

Figure 5.45: Void fraction versus distance to the hull for experimental positions.

Normalized void fraction distribution is shown in Figure 5.46 at locations at the bow and stern and at three distances from the wall where experimental data is available. Both computational and experimental results exhibit a size distribution 5 mm away from the hull that shifts towards smaller bubbles when compared to the distribution at 10 mm, though this shift is more dramatic in the experiments. A significant difference in the experiments is observed for the size distribution at 0 mm from the wall (where the probe tip is practically touching the hull) which dramatically shifts towards much smaller bubbles at the stern. This shift most likely is caused by the highly enhanced breakup of bubbles in the boundary layer, which current breakup models greatly underpredict given that the combined interaction between shear and turbulence is not taken into account. An important observation is that during the process of unfolding used in the post-processing of experimental data to obtain size distributions, an isotropic field of bubbles is assumed. This assumption clearly does not hold near the wall and may cause overprediction of larger bubbles near the wall.

The bubble size distribution is shown in Figure 5.47. The good agreement between model predictions and experimental data shows that the improvements in robustness and

accuracy enable computations that were not possible with less careful implementation of numerical schemes.

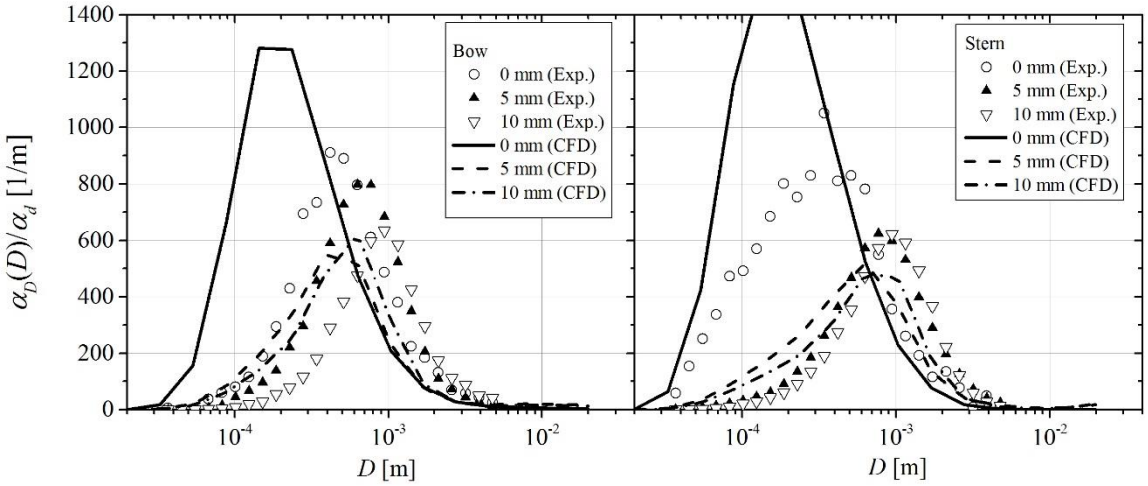

Figure 5.46: Normalized void fraction size distribution for different depths.

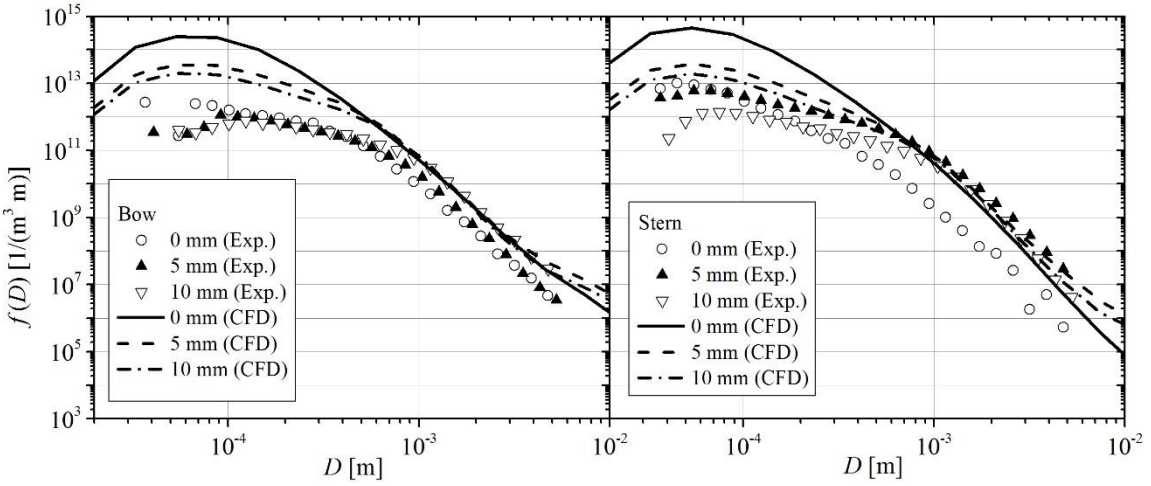

Figure 5.47: Bubble number density distribution at experimental locations.

CHAPTER 6 CONCLUSIONS AND FURTURE WORK

This thesis presents the development of a mechanistic turbulent bubble entrainment model. The model was designed for ship flow applications, and validation was performed for several flows of interest for ship hydrodynamics. The model shows good predictive capabilities when the air entrainment process is dominated by turbulence. The entrainment model is also extended to account for air entrapment due to hull/wave impact processes.

Application of the new entrainment model results in regions of very high void fraction that the original Rhie and Chow (1983) projection method is unable to handle. A novel two-phase numerical approach, developed to handle high void fractions while preventing instability, is also presented in this thesis. The approach was successfully applied to a variety of flows, including high Reynolds number ship flows with complex geometries at high void fractions.

6.1 Main contributions and conclusions

The main contributions and corresponding conclusions of this thesis can be summarized as follows:

Physical modeling

A general framework focusing on turbulent entrainment model is developed and applied to bubbly flow simulations relevant to ship hydrodynamics. The model is mechanistic, in the sense that all terms are the result of direct modeling of physical mechanisms or processes, and based on local quantities. The only modeling constant is calibrated using experimental data for bow wave breaking entrainment. This constant is also proved to be appropriate for Athena R/V simulations. Overall, the model constitutes a significant improvement over previous bubble entrainment models by virtue of better accuracy and robustness while using less adjustable parameters.

Proper turbulence levels for entrainment near the free surface are obtained through modifications to the classical two phase $k-\omega/k-\varepsilon$ SST turbulence model. Also a mixing length model is proposed to describe unresolved turbulence due to roughness on the free surface. This model can appropriately add otherwise absent turbulence near a free surface and activate the turbulent entrainment model. These two improvements to the turbulence model show improved results for wave breaking entrainment.

A packing model, similar to those used for fluidized beds, is developed to prevent unphysically high void fractions as bubbles start "packing" by exerting pressure on each other when void fraction increases. It is modeled as a diffusion term in the bubble transport equation, and is shown to be stable for high void fractions. The corresponding momentum transferred to the liquid is added as a body force to the liquid momentum equation. This force is also expanded to be consistent with the multi-group approach followed in this work.

A preliminary impact model is proposed to incorporate entrainment caused by blunt bow shapes hitting a rough free surface. The model provides insights to another different but important entrainment process occurring in ships. Though further work is necessary, encouraging results show the potential of the model.

Numerical methods

An efficient, robust and stable numerical scheme for two phase flow is developed to solve highly nonlinear multiphase equations. It mainly includes the following improvements:

A hybrid method is developed to achieve strong pressure velocity coupling in two phase flows. The methodology introduces face velocities in a collocated grid, effectively achieving mass conservation performance found on staggered grid methods in the context of a single-phase level set, overset grid solver. As a result, conservation of all flow variables is greatly improved. A non-linear interpolation for predicted face velocities is introduced

to obtain time step independent solutions and is able to handle large Courant numbers. The method is also shown to be much more stable under situations of high void fraction or large gradients of void fraction.

To improve coupling between the bubbly phase solver and the liquid solver, a total void fraction equation is introduced as a predictor step. This proved to be an efficient approach while keeping a strong coupling between the phases.

A new mass conservation equation is formulated to implicitly couple void fraction in the projection method, which removes instabilities observed at high void fractions. .

The introduction of packing forces, needed to prevent unphysical accumulation of bubbles typical of disperse two-phase flow models, is a source of instability. A semi-implicit implementation of the multi-group approach is developed to handle packing forces.

Finally, the balanced force method is extended to general curvilinear grids. This improvement can remove the spurious currents observed on node velocities in body force dominated flows.

Validation and applications work

Due to its relevance to ship flows and the high-quality data available, a 2D+T experiment was chosen to calibrate and validate the bubble entrainment model. The turbulent air entrainment model predicts well the bubble clouds generated by the wave breaking, including position, void fraction and bubble size distribution. It is found that the turbulence generated by the plunging breaker has a strong effect on the two-phase parameters of the resulting bubble clouds. The turbulence model modifications proposed in this thesis can satisfactorily predict turbulence dissipation during wave breaking. Although extra work is required to refine the models, they can be a starting point for improving free surface capabilities of isotropic turbulence models.

Further validation and demonstration was performed for the Athena R/V ship. Data is available for this ship of void fraction and bubble size distribution at the bow and stern (Johansen et al. 2010). The study shows that bubbles entrained at the bow are swept down underneath of ship. A large amount of bubbles generated due to entrainment at the bow and contact line are transported down and reach the stern, strongly affected by incoming waves. The experiment does not support a study of the effect of bubbles on ship hydrodynamics performance. A transition for the bubble size distribution is predicted, which is also observed in the experimental data. Bubbles coming from the bottom boundary layer of the ship are small with size $R \approx 80\,\mu\text{m}$. Simulation results show good agreement with experiment data in this regard. For Athena R/V a grid convergence study was performed to analyze the grid independence of the model, a major issue with previous entrainment models. Since the entrainment model strongly depends on the turbulence levels, it shows good convergence for void fraction and bubble size distribution as the turbulence converges. It is shown that a medium grid size is a good choice for full scale simulations. According to the model, bubbles reach size distribution equilibrium quickly as they travelling around the ship. In agreement with the experiments, the predicted void fraction is very high in the highly aerated transom stern.

Simulations of Kann boat show that the turbulent air entrainment model grossly underpredicts entrainment at the bow due to the low levels of turbulence predicted. The impact entrainment model properly supplements turbulent bubble entrainment for cases where bubbles are entrapped. The proposed numerical methodology can predict bubble transport in the boundary layer, where extensive data is available, providing a computational tool for development and evaluation of breakup/coalescence models inside boundary layer. The current model predicts that bubbles are uniformly distributed under the boat and the bubbly boundary layer thickness is underpredicted at the bow due to the inability to capture intense turbulent mixing, but properly predicts that the bubbly boundary layer under the boat grows as the boundary layer develops. The current breakup model

underpredicts the amount of small bubbles in the boundary layer. Interaction between turbulence and strong shear should result in high breakup rates into smaller bubbles, as observed in the experiments, but presently bubble breakup models do not include this mechanism.

6.2 Future work

Bubble entrainment is a challenging research field, in particular for ship flows. Progress made in this thesis provides guidance on possible areas for future work. There is a lack of experimental data, as geared towards development and validation of bubble entrainment modeling. Laboratory experiments should be designed to study parameters affecting entrainment to help improve modeling, for instance measuring two-phase parameters but also turbulence quantities. Additional experimental campaigns for full scale ships are needed to evaluate model application under practical conditions. The following discusses some areas of future research to improve simulation of bubbly flows around ships, mostly focusing on entrainment modeling:

Two phase modeling

Refinements to the entrainment model developed in this work. As a short term target, more work is needed to study grid convergence at the stern. Longer term, work to minimize the limitations of the turbulent air entrainment model is needed. For example, anisotropic turbulence should be considered to introduce entrainment caused by strong normal vortices interacting with the free surface (dimples), which can cause bubbles to be pulled deep. As the computation costs decrease, hybrid RANS/LES approaches (like DES) are being introduced in computational ship hydrodynamics. Improvements need to be introduced to adapt the model for DES simulations.

Improvements on impact entrainment model. The constants involved inhibit application of this model to general problems. This is an area of importance and significant potential since many ships have blunt bows where impact entrainment is important.

Bubble breakup. Current models account for turbulence-induced breakup or shear-induced breakup. In a boundary layer both effects are important and interact, shear deforming bubbles and making turbulent eddies more efficient at breaking. Current models, as shown in the simulations of Kann boat, cannot predict breakup of small bubbles inside the boundary layer.

Extension to coarser grids. Modifications to the model are needed to predict entrainment on coarse grids that cannot capture wave breaking. The simulation for Athena R/V already shows little entrainment at the masker due to inability to capture wave breaking in the coarser grid. It is desirable an entrainment model can predict appropriate entrainment under situations where the grid cannot capture wave breaking and consequent turbulence generation. This can be done by using indicators as wave slope to determine if entrainment is to occur, adding some non-mechanistic nature to the model.

Wall forces. Models accounting for interaction bubbles with the wall for bubbles about a diameter away or closer are needed to prevent excessive bubble accumulation at the wall and better match experiments. A preliminary model is presented in this work with insufficient justification. More work should focus on improvements for such forces.

Numerical improvements

1. *Pressure coupling for two phase solver*. The current two phase solver is proven to be robust and stable for bubbly flows dominated by buoyancy. The effect of the pressure gradient effect on bubble velocity are explicitly treated in the solver, which may cause numerical instability when the pressure gradient force overcomes buoyancy.
2. *Computational efficiency for turbulent entrainment model*. It is found the entrainment model takes around 20% of the total computation time for the finest grid in the Athena R/V simulation. A faster strategy for the 1D integration of

turbulent entrainment model needs to be developed to lower the computational cost.

3. *Smoothing the pressure gradient for force on bubbles*. The pressure gradient in regions of complex geometry or with bad quality grid can result in local unphysical bubble velocities. An efficient and reasonable averaging strategy could solve such numerical issues.
4. *Air/water solver for the free surface*. The single level set method is a well-established free surface capturing method for ship hydrodynamics. However, by ignoring the air flow, entrapped air resulting in cavities or large bubbles cannot be modeled. An air/water solver, like the traditional level set method or the VOF method could improve modeling of wave breakers and the performance of the present entrainment model.

REFERENCES

Adams P, George K, Stephens M, Brucker KA, O'Shea TT, Dommermuth DG. 2010. A numerical simulation of a plunging breaking wave. *Physics of Fluids*. 22(9):091111–12

Aksoy H, Chen C-J. 1992. Numerical Solution of Navier-Stokes Equations with Nonstaggered Grids Using Finite Analytic Method. *Numerical Heat Transfer, Part B: Fundamentals*. 21(3):287–306

Antal SP, Lahey RT, Flaherty JE. 1991. Analysis of phase distribution in fully developed laminar bubbly two-phase flow. *International Journal of Multiphase Flow*. 17(5):635–52

Baldy S. 1993. A generation-dispersion model of ambient and transient bubbles in the close vicinity of breaking waves. *Journal of Geophysical Research: Oceans (1978–2012)*. 98(C10):18277–93

Behzadi A, Issa RI, Rusche H. 2004. Modelling of dispersed bubble and droplet flow at high phase fractions. *Chemical Engineering Science*. 59(4):759–70

Bell JB, Colella P, Howell LH. 1991. An efficient second-order projection method for viscous incompressible flow. *10th Computational Fluid Dynamics Conference*

Bergman T, Mesler R. 1981. Bubble nucleation studies. Part I: Formation of bubble nuclei in superheated water by bursting bubbles. *AIChE Journal*. 27(5):851–53

Bhushan S, Xing T, Carrica P, Stern F. 2009. Model- and Full-Scale URANS Simulations of Athena Resistance, Powering, Seakeeping, and 5415 Maneuvering. *Journal of Ship Research*. 53(4):179–98

Bick AG, Ristenpart WD, van Nierop EA, Stone HA. 2010. Bubble formation via multidrop impacts. *Physics of Fluids*. 22(4):042105

Bin AK. 1988. Minimum air entrainment velocity of vertical plunging liquid jets. *Chemical engineering science*. 43(2):379–89

Bin AK. 1993. Gas entrainment by plunging liquid jets. *Chemical Engineering Science*. 48(21):3585–3630

Blenkinsopp CE, Chaplin JR. 2010. Bubble Size Measurements in Breaking Waves Using Optical Fiber Phase Detection Probes. *IEEE Journal of Oceanic Engineering*. 35(2):388–401

Borowski B, Sutin A, Roh H-S, Bunin B. 2008. Passive acoustic threat detection in estuarine environments. *In Society of Photo-Optical Instrumentation Engineers (SPIE) Conference Series*. 6945

Brattberg T, Chanson H. 1998. Air entrapment and air bubble dispersion at two-dimensional plunging water jets. *Chemical Engineering Science*. 53(24):4113–27

Brouilliot D, Lubin P. 2013. Numerical simulations of air entrainment in a plunging jet of liquid. *Journal of Fluids and Structures*. 43:428–40

Buning PG, Pulliam TH. 2011. Cartesian Off-Body Grid Adaption for Viscous Time-Accurate Flow Simulation. *20th AIAA Computational Fluid Dynamics Conference*, Honolulu HI

Carrica PM, Bonetto FJ, Drew DA, Lahey Jr. RT. 1998. The interaction of background ocean air bubbles with a surface ship. *International Journal for Numerical Methods in Fluids*. 28(4):571–600

Carrica PM, Castro AM, Li J, Politano M, Hyman MC. 2012. Towards an air entrainment model. *29th Symp. Naval Hydrodyn.*, Gothenburg, Sweden

Carrica PM, Castro AM, Stern F. 2010a. Self-propulsion computations using a speed controller and a discretized propeller with dynamic overset grids. *Journal of Marine Science and Technology*. 15(4):316–30

Carrica PM, Drew D, Bonetto F, Lahey Jr RT. 1999. A polydisperse model for bubbly two-phase flow around a surface ship. *International journal of multiphase flow*. 25(2):257–305

Carrica PM, Huang J, Noack R, Kaushik D, Smith B, Stern F. 2010b. Large-scale DES computations of the forward speed diffraction and pitch and heave problems for a surface combatant. *Computers & Fluids*. 39(7):1095–1111

Carrica PM, Wilson RV, Noack RW, Stern F. 2007a. Ship motions using single-phase level set with dynamic overset grids. *Computers & Fluids*. 36(9):1415–33

Carrica PM, Wilson RV, Stern F. 2007b. An unsteady single-phase level set method for viscous free surface flows. *International Journal for Numerical Methods in Fluids*. 53(2):229–56

Cartmill JW, Yang Su M. 1993. Bubble size distribution under saltwater and freshwater breaking waves. *Dynamics of atmospheres and oceans*. 20(1):25–31

Castro AM. 2011. *Polydispersed bubbly flow model for ship hydrodynamics with application to Athena R/V*. PhD thesis. University of Iowa

Castro AM, Carrica PM. 2013a. Bubble size distribution prediction for large-scale ship flows: Model evaluation and numerical issues. *International Journal of Multiphase Flow*. 57:131–50

Castro AM, Carrica PM. 2013b. Eulerian polydispersed modeling of bubbly flows around ships with application to Athena R/V. *International Shipbuilding Progress*. (1-4):403–33

Castro AM, Carrica PM. 2011. Full Scale Simulations of the Bubbly Flow Around the Research Vessel Athena With Incoming Waves and Discretized Propeller. *ASME-JSME-KSME 2011 Joint Fluids Engineering Conference*. 1709–20

Castro AM, Li J, Hyman M, Carrica PM. 2014. Turbulent and Cavity Free Surface Bubble Entrainment with Application to Ship Hydrodynamics. *30th Symposium on Naval Hydrodynamics*, Tasmania, Australia.

Chanson H. 2009. Turbulent air–water flows in hydraulic structures: dynamic similarity and scale effects. *Environmental fluid mechanics*. 9(2):125–42

Chanson H, Cummings PD. 1994. Modelling air bubble entrainment by plunging breakers. *Proceedings of the International Symposium: Waves-Physical and Numerical Modelling, IAHR*. 2:783–92

Ciborowski J, Bin A. 1972. Minimum entrainment velocity for free liquid jets. *Inz. Chem.* (Polish). 2:453–69

Cox DT, Shin S. 2003. Laboratory measurements of void fraction and turbulence in the bore region of surf zone waves. *Journal of engineering mechanics*. 129(10):1197–1205

Cummings PD, Chanson H. 1999. An experimental study of individual air bubble entrainment at a planar plunging jet. *Chemical Engineering Research and Design*. 77(2):159–64

Dalrymple RA, Rogers BD. 2006. Numerical modeling of water waves with the SPH method. *Coastal engineering*. 53(2):141–47

Davies JT. 1972. Turbulence phenomena at free surfaces. *AIChE Journal*. 18(1):169–73

Deane GB, Stokes MD. 2002. Scale dependence of bubble creation mechanisms in breaking waves. *Nature*. 418(6900):839–44

Deshpande SS, Trujillo MF, Wu X, Chahine G. 2012. Computational and experimental characterization of a liquid jet plunging into a quiescent pool at shallow inclination. *International Journal of Heat and Fluid Flow*. 34:1–14

Dommermuth D, O'Shea T, Wyatt D, Sussman M, Weymouth G, Yue D, Adams P, Hand R. 2006. The numerical simulation of ship waves using cartesian-grid and volume-of-fluid methods, Rome, Italy.

Drew DA, Passman SL. 1999. *Theory of Multicomponent Fluids*. Springer

Duncan JH. 2001. Spilling breakers. *Annual review of fluid mechanics*. 33(1):519–47

Elbing BR, Winkel ES, Lay KA, Ceccio SL, Dowling DR, Perlin M. 2008. Bubble-induced skin-friction drag reduction and the abrupt transition to air-layer drag reduction. *Journal of Fluid Mechanics*. 612:201–36

El Hammoumi M, Achard JL, Davoust L. 2002. Measurements of air entrainment by vertical plunging liquid jets. *Experiments in fluids*. 32(6):624–38

Ervine DA, Elsawy E, McKeogh E. 1980. Effect of turbulence intensity on the rate of air entrainment by plunging water jets. *ICE Proceedings*. 69(2):425–45

Esch T, Menter FR. 2003. Heat transfer prediction based on twoequation turbulence models with advanced wall treatment. *Proceedings, International Symposium on Turbulence, Heat and Mass Transfer*, 4, pp. 614–21

Esmailizadeh L, Mesler R. 1986. Bubble entrainment with drops. *Journal of Colloid and Interface Science*. 110(2):561–74

Ezure T, Kimura N, Hayashi K, Kamide H. 2008. Transient Behavior of Gas Entrainment Caused by Surface Vortex. *Heat Transfer Engineering*. 29(8):659–66

Ezure T, Kimura N, Miyakoshi H, Kamide H. 2011. Experimental investigation on bubble characteristics entrained by surface vortex. *Nuclear Engineering and Design*. 241(11):4575–84

Galvin CJ. 1968. Breaker type classification on three laboratory beaches. *Journal of geophysical research*. 73(12):3651–59

Garrett C, Li M, Farmer D. 2000. The connection between bubble size spectra and energy dissipation rates in the upper ocean. *Journal of physical oceanography*. 30(9):2163–71

Gidaspow D. 1994. *Multiphase Flow and Fluidization: Continuum and Kinetic Theory Descriptions*. Academic press

Greaves M, Kobbacy KAH. 1981. Surface aeration in agitated vessels. *Institue of Chemical Energy Symposium Series*, 64, H1

Hinze JO. 1955. Fundamentals of the hydrodynamic mechanism of splitting in dispersion processes. *AIChE Journal*. 1(3):289–95

Hirt CW. 2003. Modeling turbulent entrainment of air at a free surface. *Flow Science, Inc*

Hoque A. 2002. *Air Bubble Entrainment by Breaking Waves and Associated Energy Dissipation*. PhD thesis. Toyohashi University of Technology, Japan.

Horikawa K, Kuo C-T. 1966. A study on wave transformation inside surf zone. *Coastal Engineering Proceedings*. 1:217–33

Hosokawa S, Tomiyama A, Misaki S, Hamada T. 2002. Lateral Migration of Single Bubbles Due to the Presence of Wall. *Proceedings of ASME Fluids Engineering Division Summer Meeting*,Montreal, Oue., Canada, pp. 855–60.

Hough GR, Ordway DE. 1964. The generalized actuator disk. Technical Report TAR-TR 6401, Therm Advanced Research, Inc.

Huang J, Carrica PM, Stern F. 2007. Coupled ghost fluid/two-phase level set method for curvilinear body-fitted grids. *International Journal for Numerical Methods in Fluids*. 55(9):867–97

Hunt JCR. 1984. Turbulence structure and turbulent diffusion near gas-liquid interfaces. In *Gas Transfer at Water Surfaces*, pp. 67–82. Springer

Iafrati A. 2009. Numerical study of the effects of the breaking intensity on wave breaking flows. *Journal of Fluid Mechanics*. 622:371–411

Iafrati A. 2011. Energy dissipation mechanisms in wave breaking processes: Spilling and highly aerated plunging breaking events. *Journal of Geophysical Research*. 116(C7):

Iafrati A, Campana EF, Gomez Ledesma R, Kiger KT, Duncan JH. 2004. Air entrainment induced by the impact of a planar translating jet on a flat free surface. *Proc. 25th Symposium on Naval Hydrodynamics*. 3:84

Ishii M. 1975. Thermo-fluid dynamic theory of two-phase flow. NASA STI/Recon Technical Report A

Ishii M, Hibiki T. 2006. *Thermo-Fluid Dynamics of Two-Phase Flow*. Springer Science+Business Media

Ismail F, Carrica PM, Xing T, Stern F. 2010. Evaluation of linear and nonlinear convection schemes on multidimensional non-orthogonal grids with applications to KVLCC2 tanker. *International Journal for Numerical Methods in Fluids*. 64(8):850–86

Issa RI. 1986. Solution of the implicitly discretised fluid flow equations by operator-splitting. *Journal of computational physics*. 62(1):40–65

Jeong J-T. 2012. Free-surface deformation due to spiral flow owing to a source/sink and a vortex in Stokes flow. *Theoretical and Computational Fluid Dynamics*. 26(1-4):93–103

Jeong J-T, Moffatt HK. 1992. Free-surface cusps associated with flow at low Reynolds number. *Journal of fluid mechanics*. 241:1–22

Johansen JP, Castro AM, Carrica PM. 2010. Full-scale two-phase flow measurements on Athena research vessel. *International Journal of Multiphase Flow*. 36(9):720–37

Kiger KT, Duncan JH. 2011. Air-entrainment mechanisms in plunging jets and breaking waves. *Annual Review of Fluid Mechanics*. 44:563–96

Kothe DB. 1998. Perspective on Eulerian Finite Volume Methods for Incompressible Interfacial Flows. In *Free Surface Flows*, eds. HC Kuhlmann, H-J Rath, pp. 267–331. Springer Vienna

Kuboi R, Komasawa I, Otake T. 1972. Behavior of dispersed particles in turbulent liquid flow. *Journal of Chemical Engineering of Japan*. 5(4):349–55

Kumagai M, Endoh K. 1983. A note on the relationship between gas entrainment curve and its starting velocity. *Journal of Chemical Engineering of Japan*. 16(1):74–75

Lamarre E, Melville WK. 1991. Air entrainment and dissipation in breaking waves. *Nature*. 351(6326):469–72

Landrini M, Colagrossi A, Greco M, Tulin MP. 2007. Gridless simulations of splashing processes and near-shore bore propagation. *Journal of Fluid Mechanics*. 591:183–213

Lang AW, Manglano CE. 2004. An experimental study of a turbulent shear layer at a clean and contaminated free-surface. *Experiments in Fluids*. 36(3):384–92

Latorre R, Miller A, Philips R. 2003. Micro-bubble resistance reduction on a model SES catamaran. *Ocean Engineering*. 30(17):2297–2309

Lara P. 1979. Onset of air entrainment for a water jet impinging vertically on a water surface. *Chemical Engineering Science*. 34(9):1164–65

Lehr F, Millies M, Mewes D. 2002. Bubble-Size distributions and flow fields in bubble columns. *AIChE Journal*. 48(11):2426–43

Leifer I, de Leeuw G. 2006. Bubbles generated from wind-steepened breaking waves: 1. Bubble plume bubbles. *J. Geophys. Res.* 111(C6):C06020

Lewis D, Davidson JF. 1982. Bubble splitting in shear flow. *Transactions of the Institution of Chemical Engineers*. 60(5):283–91

Lien FS, Leschziner MA. 1994. A general non-orthogonal collocated finite volume algorithm for turbulent flow at all speeds incorporating second-moment turbulence-transport closure, Part 1: Computational implementation. *Computer methods in applied mechanics and engineering*. 114(1):123–48

Li J, Castro AM, Carrica PM. 2015. A pressure-velocity coupling approach for high void fraction free surface bubbly flows in overset curvilinear grids: Pressure-velocity coupling for free surface bubbly flows with overset. *International Journal for Numerical Methods in Fluids*. DOI: 10.1002/fld.4054

Lin TJ, Donnelly HG. 1966. Gas bubble entrainment by plunging laminar liquid jets. *AIChE Journal*. 12(3):563–71

Loewen MR, Melville WK. 1991. Microwave backscatter and acoustic radiation from breaking waves. *Journal of Fluid Mechanics*. 224(-1):601

Loewen MR, Melville WK. 1994. An experimental investigation of the collective oscillations of bubble plumes entrained by breaking waves. *The Journal of the Acoustical Society of America*. 95(3):1329–43

Lopez de Bertodano M, Moraga FJ, Drew DA, Lahey RT. 2004. The modeling of lift and dispersion forces in two-fluid model simulations of a bubbly jet. *Journal of fluids engineering*. 126(4):573–77

Lorenceau E. 2003. *Interfaces en grande deformation: oscillations, impacts, singularites.* PhD thesis. Univeristy Paris VI

Luo H, Svendsen HF. 1996. Theoretical model for drop and bubble breakup in turbulent dispersions. *AIChE Journal*. 42(5):1225–33

Ma G, Shi F, Kirby JT. 2011a. A polydisperse two-fluid model for surf zone bubble simulation. *Journal of Geophysical Research: Oceans (1978–2012)*. 116(C5):C05010

Ma J, Oberai AA, Drew DA, Lahey Jr RT, Moraga FJ. 2010a. A quantitative sub-grid air entrainment model for bubbly flows–plunging jets. *Computers & Fluids*. 39(1):77–86

Ma J, Oberai AA, Hyman MC, Lahey Jr RT, Drew DA. 2010b. A generalized subgrid air entrainment model for RaNS modeling of bubbly flows around ship hulls. *7th International Conference on Multiphase Flow-IcmF 2010 Proceedings*, Tampa, Florida

Ma J, Oberai AA, Lahey RT, Drew DA. 2011b. Modeling air entrainment and transport in a hydraulic jump using two-fluid RANS and DES turbulence models. *Heat and Mass Transfer*. 47(8):911–19

Martínez-Bazán C, Montanes JL, Lasheras JC. 1999. On the breakup of an air bubble injected into a fully developed turbulent flow. Part 1. Breakup frequency. *Journal of Fluid Mechanics*. 401:157–82

McKeogh EJ, Ervine DA. 1981. Air entrainment rate and diffusion pattern of plunging liquid jets. *Chemical Engineering Science*. 36(7):1161–72

Menter FR. 1994. Two-equation eddy-viscosity turbulence models for engineering applications. *AIAA Journal*. 32(8):1598–1605

Mesler R, Mailen G. 1977. Nucleate boiling in thin liquid films. *AIChE Journal*. 23(6):954–57

Miettinen A. 1997. *A study of the pressure correction approach in the colocated grid arrangement*. Helsinki University of Technology

Mofidi A, Carrica PM. 2014. Simulations of zigzag maneuvers for a container ship with direct moving rudder and propeller. *Computers & Fluids*. 96:191–203

Montazeri H, Ward CA. 2014. A balanced-force algorithm for two-phase flows. *Journal of Computational Physics*. 257:645–69

Moraga FJ, Carrica PM, Drew DA, Lahey Jr. RT. 2008. A sub-grid air entrainment model for breaking bow waves and naval surface ships. *Computers and Fluids*. 37(3):281–98

Moraga FJ, Larreteguy AE, Drew DA, Lahey Jr RT. 2003. Assessment of turbulent dispersion models for bubbly flows in the low Stokes number limit. *International Journal of Multiphase Flow*. 29(4):655–73

Mori N, Suzuki T, Kakuno S. 2007. Experimental study of air bubbles and turbulence characteristics in the surf zone. *Journal of Geophysical Research: Oceans (1978–2012)*. 112(C5):C05014

Noack R. 2005. SUGGAR: a general capability for moving body overset grid assembly. *AIAA paper*. 5117:2005

Oguz HN, Prosperetti A, Lezzi AM. 1992. Examples of air-entraining flows. *Physics of Fluids A: Fluid Dynamics (1989-1993)*. 4(4):649–51

Pascau A. 2011. Cell face velocity alternatives in a structured colocated grid for the unsteady Navier–Stokes equations. *International Journal for Numerical Methods in Fluids*. 65(7):812–33

Perret MN, Esmaeilpour M, Carrica PM. 2014. Two Phase Flow Measurements in a Full Scale Boundary Layer. *30th Symp. Naval Hydrodyn.,* Hobart, Australia

Pope SB. 2000. *Turbulent Flows*. Cambridge university press

Prince MJ, Blanch HW. 1990. Bubble coalescence and break-up in air-sparged bubble columns. *AIChE Journal*. 36(10):1485–99

Pumphrey HC, Elmore PA. 1990. The entrainment of bubbles by drop impacts. *Journal of Fluid Mechanics*. 220:539–67

Rapp RJ, Melville WK. 1990. Laboratory measurements of deep-water breaking waves. *Philosophical Transactions of the Royal Society of London. Series A, Mathematical and Physical Sciences*. 735–800

Rhie CM, Chow WL. 1983. Numerical study of the turbulent flow past an airfoil with trailing edge separation. *AIAA journal*. 21(11):1525–32

Savelsberg R, Van De Water W. 2009. Experiments on free-surface turbulence. *Journal of Fluid Mechanics*. 619:95–125

Saylor J, Bounds GD, others. 2012. Experimental study of the role of the Weber and capillary numbers on Mesler entrainment. *AIChE Journal*. 58(12):3841–51

Sene KJ. 1988. Air entrainment by plunging jets. *Chemical Engineering Science*. 43(10):2615–23

Shen L, Yue DK. 2001. Large-eddy simulation of free-surface turbulence. *Journal of fluid mechanics*. 440:75–116

Shen WZ, Michelsen JA, Sørensen JN. 2001. Improved Rhie-Chow interpolation for unsteady flow computations. *AIAA journal*. 39(12):2406–9

Shi F, Kirby JT, Ma G. 2010. Modeling quiescent phase transport of air bubbles induced by breaking waves. *Ocean Modelling*. 35(1-2):105–17

Shu C-W. 1998. *Essentially Non-Oscillatory and Weighted Essentially Non-Oscillatory Schemes for Hyperbolic Conservation Laws*. Springer

Sigler J, Mesler R. 1990. The behavior of the gas film formed upon drop impact with a liquid surface. *Journal of Colloid and Interface Science*. 134(2):459–74

Sutin A, Benilov A, Roh H-S, Nah YI. 2008. Acoustic measurements of bubbles in the wake of ship model in tank. *Journal of the Acoustical Society of America*. 123(5):3751

Takahashi M, Inoue A, Aritomi M, Takenaka Y, Suzuki K. 1988. Gas Entrainment at Free Surface of Liquid,(II) Onset Conditions of Vortex-Induced Entrainment. *Journal of Nuclear Science and Technology*. 25(3):245–53

Tavakolinejad M. 2010. *Air bubble entrainment by breaking bow waves simulated by a 2D+T technique*. PhD thesis. University of Maryland

Thompson JF, Warsi ZU, Mastin CW. 1985. *Numerical Grid Generation: Foundations and Applications*, Vol. 45. North-holland Amsterdam

Thoroddsen ST, Etoh TG, Takehara K. 2003. Air entrapment under an impacting drop. *Journal of Fluid Mechanics*. 478:125–34

Townsend AA. 1966. The mechanism of entrainment in free turbulent flows. *Journal of Fluid Mechanics*. 26(04):689–715

Trevorrow MV, Vagle S, Farmer DM. 1994. Acoustical measurements of microbubbles within ship wakes. *The Journal of the Acoustical Society of America*. 95(4):1922–30

Trevorrow MV, Vasiliev B, Vagle S. 2006. Wake acoustic measurements around a maneuvering ship. *Canadian Acoustics*. 34(3):112–13

UNCTAD. 2009. United Nations Conference on Trade and Development. *Summary of Proceedings, Geneva*

van de Sande E, Simith JM. 1974. Mass transfer in a pool with plunging liquid jets. *Proceedings of the international Chem. Engng Symposium Multiphase Flow Systems, Glasgow*

van de Sande E, Smith JM. 1975. Mass transfer from plunging water jets. *The Chemical Engineering Journal*. 10(2):225–33

Wallis GB. One-dimensional two-phase flow, 1969. *McGraw-Hill, New York*

Xing T, Shao J, Stern F. 2007. BKW-RS-DES of unsteady vortical flow for KVLCC2 at large drift angles. *Proc 9th Int Conf on Numerical Ship Hydrodynamics*, Ann Arbor, MI

Yeoh GH, Tu J. 2010. *Computational Techniques for Multi-Phase Flows*. Elsevier Ltd.

Yu B, Kawaguchi Y, Tao W-Q, Ozoe H. 2002. Checkerboard Pressure Predictions Due to the Underrelaxation Factor and Time Step Size for a Nonstaggered Grid with Momentum Interpolation Method. *Numerical Heat Transfer, Part B: Fundamentals*. 41(1):85–94